RAPPORT ANNUEL
2007

Sous projet SC25

Detection of Deep Conductive Massive Orebodies by Magnetotelluric Surveys

By

Michel Chouteau*, Olivier Boulanger*, Bernard Giroux*

* Département des génies civil, géologique et des mines, École Polytechnique, Montréal, Québec
chouteau@geo.polymtl.ca

Soumis à l'administration de DIVEX
juillet, 2007 – Québec

DIVEX, INRS, Eau Terre Environnement, 490 de la Couronne, Québec, Québec G1K 9A9
Tél. : (418) 654-2652; Fax : (418) 654-2600; Courriel : info@divex.ca; Site web : www.divex.ca

1. CONTEXT

An agreement was signed between Xstrata Zinc Canada and École Polytechnique to assess the capability of the Magnetotelluric method to detect a few types of massive sulphide orebodies at large depths and to estimate their geometric and physical properties. Xstrata Zinc Canada has committed a contribution of 15,000 $ to the project that adds up to the existing contribution of 15,000 $ from the MÉDIE (Ministère du Développement Économique, de l'Innovation et de l'Exportation). An extra 3,000 $ was recently added (April 2007) by the MÉDIE.

We have proposed to model the responses of deep targets explored by Xstrata and to develop and test two (2) approaches in order to allow the interpreter to select targets with confidence in exploring for massive conductive ore bodies. Xstrata would supply the geometry and the electrical conductivity distribution of the selected orebodies (Matagami-, Raglan- and Bathurst-VMS type deposits) as well as the MT survey data collected on those properties.

The project collaborators are Michel Chouteau (École Polytechnique), Michel Allard (senior geophysicist, Xstrata Zinc Canada, Laval) and Sharon Taylor (geophysicist, Xstrata Zinc Canada, Bathurst).

The present progress report (report #1) displays and discusses the 3D MT modelling responses of the selected models. In the following we will first introduce the methodology used to compute the MT responses, then the results for each particular model and finally we will discuss about the depth of investigation of the MT method for such models (detection capability).

2. METHODOLOGY

2.1. Modelling

Synthetic data were computed using 3D numerical modelling with the finite differences method. The computer code of MacKie et al (1994, 1999) was used for this step. Modelled responses were obtained for different orebody models by varying geometry and electrical conductivities

The 3D modelling algorithm uses the integral form of Maxwell’s equations to derive a finite difference approximation for the magnetic field that is second order. Non-divergence of the magnetic field is enforced by evaluating the magnetic and electric fields on grids that are staggered relative to one another. The resulting linear system is solved by pre-conditioned conjugate gradient relaxation. It assumes that 2D structure parallel to each edge continues uniformly to infinity in the direction normal to the edge. The new program assigns the tangential magnetic fields using 2D calculations for each edge. The edges parallel to the source magnetic field will have electric current flowing normal to them and so TE mode calculations are done. The edges perpendicular to the source magnetic field will have current flowing parallel to them. In these cases, the tangential magnetic fields are zero. More information about the 3D code can be found in MacKie and Booker (1999).

2.2. Selection of orebody models

The MT responses were computed from geoelectrical models of 3D deep orebodies explored by Xstrata. They are:

1. VMS-type sulphide ore bodies of the Rouyn-Noranda and Matagami mining camps (VMS stands for Volcanogenic Massive Sulphides)
2. Raglan-type individual Ni ore bodies
3. Raglan orebodies and host rock from geological model of the camp
4. Bathurst Half Mile massive sulphide orebodies

For the VMS-type deposits of Noranda-Matagami the alteration zone surrounding the massive body is larger that the body alone. It could occur that at a depth of several hundred meters the massive bodies could be undetectable while the alteration zone could well be. We model the alteration zone by a weak decrease of resistivity (factor of 4) with regards to the host rock.

We therefore consider 3 models for the VMS deposits: massive sulphides only, alteration zone only and massive sulphides surrounded by alteration zone. For the Raglan-type individual Ni deposit, we consider a cubic compact conductor at different depths. For computing the responses of Raglan orebodies and host rock using a geological model of the camp we will build a model out of the known geology from Xstrata and from the results of the interpretation from a Titan 24 survey carried out on the property. For the Bathurst orebodies, a geoelectrical model built from the Half Mile Lake deposit will be used and tested.

The project will follow a sequence of steps:

1. Selection of the geoelectrical models for the orebodies presented above.
2. 3D numerical modelling of those selected models with variable depths and electrical properties.
3. Interpolation of the modelled data on a regular grid. The 3D mesh used to compute the MT responses is adapted to the geometry of the model,

conductivities and conductivity gradients and frequency range. Thus it is not regular with constant spacing; however the MT soundings collected in a survey are usually equally distributed with spacing of the order of 100 m to a 1 km. Therefore modeled data (impedances and magnetic transfer functions) will be interpolated on a grid 50 m x 50 m.

4. Calculation of impedance invariants.
5. Display (maps, soundings) of impedance invariants and tipper.

During the course of their standard Titan-24 survey, Quantec uses of a single set of X-Y magnetic coils along the line and records Ey electric fields spaced every 200m (compared to Ex electric fields spaced 100m). We will verify the effects that these shortcuts have on the quality of data set and its limitation on the detection of the selected orebody.

3. MODELLED MT RESPONSES

For each of the models we have computed the five MT fields (Ex, Ey, Hx, Hy, and Hz), the elements of the impedance tensor and the vertical magnetic transfer functions for every frequency and every position. As there are many parameters to display, we have selected here to display maps of principal impedances (Zxy and Zyx) for a few frequencies, resistivity and phase pseudo-sections for two orthogonal transects across the bodies and some profiles of important parameters with distance and frequency. All other parameters not displayed here are available in the database and can be displayed on request.

3.1. Matagami model

The Matagami (and also Rouyn-Noranda) type of massive orebody consists of a vertical thick sheet with dimensions of 300 m x 30 m x 200 m (Ly x Lx x Lz) where Ly: strike length, Lx: thickness, and Lz: depth extent). Its conductivity is 0.1 Ω.m. The depth to the upper face, d, is varied from 0 to 2 000 m. The host rock has a high resistivity of 40,000 Ω.m typical of the Abitibi Subprovince geological environment. Figure Mat-1 shows the model outcropping at ground surface. Figure Mat-2 shows a plan view of the 3D domain used to calculate the body response. The mesh is adapted to the shape and to the resistivity contrast of the body in such a way that the electromagnetic fields are well estimated by the finite difference computation.

Results from the 3D modelling code consist of all the components of the electric field (Ex and Ey) and of the magnetic fields (Hx, Hy and Hz) for each polarization (hx and hy). Then the two sets (for each polarization) are used to calculate the impedance tensors. Figure Mat-3 shows for example the magnetic field Hy generated by the conductive body for a polarization hx. Figure Mat-4 displays the resistivities calculated from the impedance tensor elements (xx, xy, yx and yy) for a frequency of F = 1000 Hz.

The model has been run for 17 frequencies equally distributed geometrically between 1 Hz and 10,000 Hz. The impedances have been estimated at the central node of each cell of the modelling domain. As the dimensions of the cells vary over the entire grid, the impedances have been further estimated by Akima interpolation at equally separated MT sites on a surface grid of 50 m x 50 m. Modelled data (apparent resistivities and phases and tipper) can now be presented either in pseudo-sections along traverses, as maps at various frequencies (or periods), as profiles along traverses or as soundings for each site. We have generated all those plots. However, because of the large amount of plots that could be displayed in the report, we have selected only a few which are the most representative of the modelled responses.

- Figures Mat-5, Mat-9 and Mat-12 show maps of the MT parameters at F = 10,000 Hz for three different depths (0, 100 m and 200 m).
- Figures Mat-6, Mat-10 and Mat-13 show pseudo-sections of MT parameters for two orthogonal profiles across the conductive body (X-axis or y = 0, and Y-axis or x = 0) for z = 0, 100 and 200 m.
- Figures Mat-7 and Mat-11 show the profiles at three selected frequencies (F = 1, 10, 100, 1000, 10000 Hz) of ρ_{det} along the X-axis (y = 0) for z = 0 and 100 m respectively. We observe that at z = 100 m the resistivity profiles are almost identical whatever the frequency and the minimum anomaly is 21,400 Ω.m over the body compared to the host rock resistivity (40,000 Ω.m) for a maximum deflection of ~33%. The tipper shows a maximum of ~6.6% at 1000 Hz (8.2% at 10,000 Hz) which is slightly above the practical detection level of 3-5 % presently in field surveys.
- Figures Mat-14, Mat-15 and Mat-16 display the apparent resistivity profiles (yx, xy and det) along the X-axis (y = 0) for all selected depths (0, 100, 200, 300, 400, 500, 1000 m) at F = 1000 Hz. Changes of yx resistivity (with regards to the host rock resistivity) are >100%, 67.4%, 30.5%, 13.2%, 6.6%, 3.6% and 0.1% respectively. For ρ_{det}, they are >100%, 46.6%, 17.9%, 7.4%, 3.5%, 1.7% and 0.1% respectively. If we assume that a significant resistivity anomaly is at least 20% change from background, then ρ_{yx} can detect orebodies at a

maximum depth of ~250 m and ρ_{det} of <200 m.

- Figures Mat-17, Mat-18 and Mat-19 display the apparent phase profiles (yx, xy and det) along the X-axis (y = 0) for all selected depths (0, 100, 200, 300, 400, 500, 1000 m) at F = 1000 Hz. In all cases changes are less than 30, which is about the limit (~20) for detecting some significant change.
- Figure Mat-20 display the tipper profiles along the X-axis (y = 0) for all selected depths (0, 100, 200, 300, 400, 500, 1000 m) at F = 1000 Hz. If we set 5% as the detectable minimum level, only orebodies ≤100 m can be detected.
- Figures Mat-21, Mat-22 and Mat-23 display the apparent resistivity profiles (yx, xy and det) along the Y-axis (x = 0) for all selected depths (0, 100, 200, 300, 400, 500, 1000 m) at F = 1000 Hz.

3.2. VMS1 model

VMS1 is the model of the alteration zone without a massive conductive core. The alteration has a resistivity 4 times smaller than the background resistivity (10,000 Ω.m and 40,000 Ω.m respectively). It is a thick vertical prism with dimensions (Ly x Lx x Lz) 400 m x 200 m x 600 m (Fig. VMS1-1). Depth to the top varies from 0 to 2000 m.

- Maps of the MT parameters for F = 10,000 Hz are plotted in Figure VMS1-2.
- Figures VMS1-3 and VMS1-4 display the pseudo-sections for all MT parameters for z = 0 and 100 m.
- Figures VMS1-5, VMS1-6 and VMS1-7 display the apparent resistivity profiles (yx, xy and det) along the X-axis (y = 0) for all selected depths (0, 100, 200, 300, 400, 500, 1000 m) at F = 10,000 Hz. Changes of yx (xy) resistivity (with regards to the host rock resistivity) are 69.4% (86.1%), 41.4% (42.8%), 30.3% (17.9%), 10.3% (8.3%), 5.5% (4.1%), 3.1% (2.3%) and 0.2% (0.2%) respectively. For ρ_{det}, they are 79.4%, 42.1%, 19.1%, 9.3%, 4.8%, 2.7% and 0.2% respectively. If we assume that a significant resistivity anomaly is at least 20% change from background, then ρ_{yx} can detect orebodies at a maximum depth of ~250 m and ρ_{det} of <200 m.
- Figures VMS1-8, VMS1-9 and VMS1-10 display the apparent phase profiles (yx, xy and det) along the X-axis (y = 0) for all selected depths (0, 100, 200, 300, 400, 500, 1000 m) at F = 10,000 Hz. In all cases changes are less than 30 for bodies deeper than 100 m. The limit for detecting some significant change is about ~20.
- Figure VMS1-11 display the tipper profiles along the X-axis (y = 0) for all selected depths (0, 100, 200, 300, 400, 500, 1000 m) at F = 1000 Hz. The shallow (0 m) body causes an anomaly of 6.8 % and bodies with depths larger than 100 m have tippers below 2.5%. If we set 5% as the detectable minimum level, only bodies at the surface can be detected using the tipper.
- Figures VMS1-12, VMS1-13 and VMS1-14 display the apparent resistivity profiles (yx, xy and det) along the Y-axis (x = 0) for all selected depths (0, 100, 200, 300, 400, 500, 1000 m) at F = 10,000 Hz. Changes of yx resistivity (with regards to the host rock resistivity) are the same as along the X-axis because the body is symmetric.
- Figures VMS1-15, VMS1-16 and VMS1-17 display the apparent phase profiles (yx, xy and det) along the X-axis (y = 0) for all selected depths (0, 100, 200, 300, 400, 500, 1000 m) at F = 10,000 Hz. Again the maximum phase changes are the same as along the X-axis.
- Figure VMS1-18 display the tipper profiles along the X-axis (y = 0) for all selected depths (0, 100, 200, 300, 400, 500, 1000 m) at F = 1000 Hz. The tipper is 4.7% for z = 0 m and it is smaller than 1.8% for depths larger than 100 m. Again only bodies at the ground surface can be detected using the tipper.

3.3. VMS2 model

VMS2 is the model of the alteration zone (VMS1) surrounding the massive conductive body with dimensions and resistivity identical to the Matagami model above. Depths to the top of the alteration zone vary from 0 to 2000 m. The top of the conductive core is at the same depth than the top of the alteration zone. The resistivity model is shown in Figure VMS2-1.

- Figures VMS2-2 and VMS2-4 map the MT parameters for depths z = 0 and 100 m respectively at F = 10^4Hz.
- The pseudo-sections along Y-axis and X-axis are displayed in Figures VMS2-3 and VMS2-5 for depths z = 0 and 100 m respectively.
- Profiles along X-axis (y = 0) of resistivities and phases for Zyx, Zxy and Zdet at F = 10,000 Hz are shown in Figures VMS2-6, VMS2-7, VMS2-8,
- VMS2-9, VMS2-10 and VMS2-11 for depths varying from 0 to 1000 m.
- Profiles of tipper at F = 10,000 Hz for the same depth range are shown in Figure VMS2-12.

- Profiles along Y-axis (x = 0) of resistivities yx, xy and det at F = 10,000 Hz are shown in Figures VMS2-13, VMS2-14, VMS2-15 for depths varying from 0 to 1000 m.
- Profiles along Y-axis (x = 0) of tipper at F = 10,000 Hz for the same depth range are shown in Figure VMS2-16.

The MT response of such an orebody model can be detected for depths up to 300 m at the most using Zyx (250 m with Zdet). The tipper is also sensitive (>0.03) to ~ 200 m.

3.4. Raglan basic Ni model

The Raglan basic massive Ni model consists of a compact cubic sulphide body of 100 m x 100 m x 100 m displaying a resistivity of 0.1 Ω.m embedded in a 40,000 Ω.m resistive host rock (see Figure RIN-1). Depths are varied from 0 to 2000 m.

- Figures RNI-2 and RNI-4 show maps of the MT parameters for depths z = 0 m and 100 m respectively.
- The pseudo-sections along Y-axis and X-axis are displayed in Figures RNI-3 and RNI-5 for depths z = 0 and 100 m respectively.
- Figures RIN-6, RNI-7, RNI-8 and RNI-9 show profiles of apparent resistivity ρ_{yx}, ρ_{xy} and ρ_{det} and of the tipper along the X-axis for a body at z = 100 m for the whole frequency range [1 Hz; 10,000 Hz]. We observe that the resistivity profiles are almost identical whatever the frequency and the anomaly is 26,670 Ω.m over the body compared to the host rock resistivity (40,000 Ω.m) for a maximum deflection of 26%. The tipper shows a maximum of ~3% at high frequencies which is barely detectable presently in field surveys.
- Profiles of resistivities and phases for Zyx, Zxy and Zdet at F = 10,000 Hz are shown in Figures RNI-10, RNI-11, and RNI-12 for depths varying from 0 to 1000 m.
- Profiles of tipper at F = 10,000 Hz for the same depth range are shown in Figure RNI-13. From those results, we can state that beyond 100 m depth the body cannot be detected.

3.5. Raglan orebodies and host rock (geological model)

This model is built from a geological cross-section of the site (courtesy of Xstrata Nickel Ltd) and from resistivities estimated by inversion from a Titan 24 survey. A gOcad model was built from the known geology (Figure RAG-1) and units were filled with voxets of corresponding resistivities. The resistivity distribution was then exported as input for the 3D MT modelling code of MacKie. The model includes known orebodies (8G, 8F, 8H). In order to estimate the anomalies caused by the small Ni orebodies from the response to the regional geology the model was run with and without the orebodies: once with the conductive orebodies and a second time without the orebodies (in fact they are replaced by the closest background resistivity). The basic model is shown in Figure RAG-2. The MT (resistivity, phase, tipper) parameters are mapped for both frequencies F = 10^4 and 10^2 Hz in Figures RAG-3 and RAG-4. Obviously the MT data is responding to the main lithologies and structure of the region. Figure RAG-5 shows the pseudo-sections along two perpendicular profiles running over the orebody 8H.

As discussed above, we have modelled the response of the Raglan model without the known orebodies (Figure RAG-6) to assess the anomalies caused by the conductive bodies by computing the difference with the responses from the previous one. Differences were estimated differently for resistivity on one side and phase and tipper on the other side. Resistivity difference is estimated by taking the log10 (ρ^*/ρ^0) where ρ^* and ρ^0 are the resistivity response for the model with and without orebodies respectively. For phase and tipper, we simply subtract the response of the model without orebodies from the one with orebodies (i.e., Φ^* -Φ^0). Figures RAG-7 and RAG-8 map the differences (resistivity, phase, tipper) at F = 10^4 Hz and 10^2 Hz respectively. Figure RAG-9 shows the pseudo-sections of the differences (resistivity, phase, and tipper) for the two perpendicular profiles running over body 8H. Obviously the differences are negligibly small and some deviations from 0 are randomly distributed and may be caused by round off errors or too coarse meshing. For computing the responses of the Raglan model we use the same cell size (12.29m x 18.61m 10.40m) for the entire 3D domain. That amounts to 100 x 100 x 81 cells (810,000 cells). We use 2 GB of memory to run the Raglan model with such mesh which hits the limit for the 32-bit CPU.

We then decided to test if those negligible differences were caused by the limited size of the bodies or by the limited discretization of the model. We have checked the sensitivity of the modelling to the size of the conductive body by enlarging the conductive body 8H twice. For model 0, body 8H had an horizontal extension of 5 x 3 cells (61.4m x 55.8m); for model 1, 8H was extended horizontally to 10 x 8 cells (about 5.3 times larger than original or 123m x 149m); for model 2, 8H was extended horizontally to 14 x 12 cells (about

11.2 times larger than original or 172m x 223m).

Model 1 is shown in Figure RAG-10 and model 2 in Figure RAG-15. Using the same mesh as used to compute the original model (model 0), we have computed the responses of model 1 and model 2. Then we have computed the differences between the responses of model 1 and 2 and model 0. Figures RAG-11 and RAG-12 displays the pseudo-sections of the differences between model 1 and model 0 along two sets of perpendicular profiles. The first set is for x = 0 and y = 0 and the second set is for x = 300 and y = 550 which intersect just above body 8H. Figures RAG-13 and RAG-14 map those differences for F = 10^3 and 10^2 Hz. Obviously again the differences are negligibly small. The same exercise is repeated using model 2 compared to model 0. Figures RAG-16 and RAG-17 displays the pseudo-sections of the differences between model 2 and model 0 along two sets of perpendicular profiles. The first set is for x = 0 and y = 0 and the second set is for x = 300 and y = 550. Figures RAG-18 and RAG-19 map those differences for F = 10^3 and 10^2 Hz. Obviously once again the differences are negligibly small. We have also computed the differences between the responses for model 1 and model 2 with the one for the model without conductive orebodies. Differences are negligible. The detection of orebodies like 8H at depths of 500 – 600 m is in agreement with the results from the modelling of simple 100m x 100m x 100m Ni bodies done before. The size of the body is too small compared to depth to generate a detectable MT anomaly.

3.6. Bathurst Half Mile model

The HalfMile deposit of the Bathurst mining camp was modelled in gOcad using geological and resistivity information supplied by Sharon Taylor (geophysicist in charge of the property). Then meshing of the resistivity distribution was generated and exported as input into MacKie's 3D MT modelling program. This model provided a good opportunity to test the differences between the earth transfer functions estimated from a local five-component MT sounding and an equivalent site using the Quantec Titan24 configuration. The latter uses the Hx and Hy measured magnetic fields of one site only for estimating impedances at all sites (this is equivalent of saying that the magnetic field does not significantly changes along the 24 sites/2.4 km profile). The HalfMile geological cross-section and the resistivity model are shown in Figures Bat-1 and Bat-2 respectively. The model presents a constant cross-section along strike for a long distance (1.8 km) and in terms of MT response it could be modelled as 2D (or 2½D) geometry. However here we have modelled it in 3D to avoid possible approximations in the computed responses.

The magnetic field Hx perpendicular to structural strike changes quite rapidly along the X-axis (Figure Bat-3). This is caused by induction and the changes are increasing with increasing frequencies. At the position of the outcropping body the magnetic field is maximum and can be as high as 4-5 times (for 1000 Hz; 10,000 Hz respectively) the one measured away from the body. We note that the transient behaviour of Hx for X positive (right side in Figure Bat-3) decays more slowly for lower frequencies. This is caused by migration with lower frequencies along the dip of the current density induced within the conductive body.

The impedances at each site were computed from the local electric fields and the reference magnetic fields. The reference site for the Hx and Hy magnetic fields can be located anywhere along the MT profile across the deposit.

Figures Bat-4 and Bat-5 show profiles of the apparent resistivities ρ_{xy} measured along X-axis with the electric field perpendicular to strike for 5-component and Titan24-like MT sites (magnetic field reference is at x = -0.111 km for the Titan24). As the magnetic field in this case is measured parallel to strike and therefore there is no induction, they are no differences between the two types of MT site.

However if we measure the apparent resistivities and phases for the impedance with the electric field (Ey) measured parallel to strike (magnetic field Hx perpendicular to strike), the differences can be important. Figures Bat-6 and Bat-7 show ρ_{yx} and Φ_{yx} profiles computed for a 5-component site while Figures Bat-8 and Bat-9 show ρ_{yx} and Φ_{yx} profiles for a Titan24-like site (in this case the magnetic field reference is at x = -0.111 km). We re-plot ρ_{yx} and ρ_{yx}^{ref} (ref is for the Titan24-like site) and Φyx and Φyxref in Figures Bat-10 and Bat-11 respectively to better compare both types of MT response and assess the differences. As a general rule, the magnitudes of the anomalies are smaller and the profiles are smoother for the Titan24-like responses compared to the ones from a 5-component site. That means that some lateral resolution will be lost and conductivities from mineralization underestimated. Here the HalfMile body is shallow and it has a large strike extent; both factors cause induction to be large and the basic assumption underlying the Titan24 philosophy, that is the magnetic field does not significantly change over the body, is violated.

The location where the magnetic reference field is measured has some impact on the MT responses. Figures Bat-12 and Bat-13 show ρ_{yx} and Φ_{yx} profiles for a Titan24-like site with the magnetic reference site at x = - 0.538 km instead of x = - 0.111 km as previously.

We re-plot ρ_{yx} and ρ_{yx}^{ref} in Figures Bat-14 to better compare both resistivities. We observe that now that the resistivities away from the body (over the host rock) are underestimated. In general, an interpretation of the Titan24-like responses would lead to the same contrast of resistivities between the host rock and the conductive body whatever the location of the magnetic reference site except that neither the true resistivities of the host rock or of the body or both can be retrieved.

Lateral variations of apparent resistivity, phase and tipper can be better observed by plotting maps for a few frequencies. Figures Bat-15 and Bat-16 show the MT responses at $F = 10^3$ Hz and 10 Hz respectively. Figure Bat-17 show apparent resistivities and phases (xy, yx and det) and tipper pseudo sections of the HalfMile orebody for = [1 Hz – 10^4 Hz] along profiles perpendicular to strike (X-axis) on the left and parallel to strike (Y-axis) on the right. Note the rapid MT parameter changes along X especially in the vicinity of the outcropping conductive body (x ~ - 0.5 km). Note also how ρ_{yx} varies smoothly over the profile while ρ_{xy} detects every small variation of resistivity associated with lithology change.

To assess the impact of the two situations a 2D MT inversion on both sets of impedances (five-component versus Titan24-like MT sites) will be shown and discussed in the final report.

4. DICUSSION

4.1. Depth of detection

The major aspect of the modelling study is to estimate the detection capability of the MT method for some types of conductive orebodies. The detection capability can be defined as the maximum depth at which the specific target causes a measurable change of the background response. We assume here that the changes have to be respectively 20%, 20 and 3% minimum for resistivity, phase and tipper to be significant. According to these thresholds, the depths of detection for our models are:

Table 1: Depths of detection for ρ, Φ and tipper.

Models	Depth of detection based on:		
	ρ	Φ	tipper
Matagami	200m	<100m	100m
VMS1	200-250m	100m	<100m
VMS2	250-300m	300m	<200m
Raglan-Ni	100-150m	<100m	<100m

As a crude rule of thumb we can estimate the maximum depth of detection by:

$$p^d(m) = (Lx.Ly.Lz)^{1/3}$$

For example, p^d would be 120m, 360m and 100m for Matagami, VMS1-VMS2 and Raglan-type models respectively. In general, the resistivities are more sensitive than phases and tipper for deep detection. This is presumably caused by the very small inductive response from the 3D conductive bodies. Induction causes changes in the magnetic fields which are sensed by the tipper. Most of the response from 3D deep bodies are generated galvanically (charges at conductivity boundaries). That causes changes in the electric field amplitude but little in its phase. Therefore in the impedance only the amplitude is affected but not so much the phase.

4.2. Anomaly width with depth

There is no clear evidence of a relationship between depth to the top of the conductive body and width of the anomaly for a fixed frequency. For most models the width of the anomaly is approximately the same whatever the depth. A possible explanation is the following. As most of the mechanism for the generation of the MT anomaly is galvanic (quasi-static; see for example Figures RIN-6, -7 and -8), the electric field changes at ground surface are caused by charges accumulated at conductivity boundaries. The anomalous (secondary) electric field arising from the charges decays very fast away from the body (as $1/r^2 - 1/r^3$). Therefore only above the body the change is noticeable; on either side of the body the change is negligible. Obviously when depth is too large the anomaly is unnoticeable.

4.3. Anomaly with frequency

Apart from the responses computed for bodies at z = 0 m, the responses from deeper bodies are almost identical (see for example Figures MAT-11 and RIN-8) for all frequencies [1 Hz; 10^4 Hz]. This is an indication of a galvanic response (quasi-static or independent of frequency). In most models, the background resistivity is 40,000 Ω.m that yields a minimum penetration depth of 1000m at 10^4 Hz. For lower frequencies the depth increases to reach 100km at 1 Hz. In all cases the quasi-static approximation is valid.

4.4. Raglan mine camp

MT modelling of the region containing the Ni orebodies 8F, 8G, 8H show that lithologies and structure are finely mapped by apparent resistivities, phases and tipper; however within the modelling computation errors the known conductive orebodies do not cause detectable anomalies. Even virtual increase of the size of body 8H to 11 times (in x and y) its size does not cause a significant anomaly

4.5. Bathurst HalfMile

The HalfMile orebody is outcropping and therefore the inductive response is large. It causes the rapid change of the horizontal magnetic field perpendicular to the body strike. Therefore the assumption behind the Titan24-type sounding is not fulfilled and differences appear between the local 5-component and the Titan24-type MT responses. In general, an interpretation of the Titan24-like responses would lead to the same contrast of resistivities between the host rock and the conductive body whatever the location of the magnetic reference site except that neither the true resistivities of the host rock or of the body or both can be retrieved.

5. CONCLUSION

Modelling has shown that small conductive orebodies are difficult to detect with MT. Only bodies with sizes comparable with the depth explored are possibly detected by the MT method. In the next report we will explore the capability of inversion (1D of Zdet and 3D of the impedance tensor) to retrieve depth to the conductive orebody and geometry.

6. REFERENCES

Legault, Jean, 2006: Experiences in geologically constrained 2D DCIP & MT inversions using Titan-24; presented at the Annual GAC-MAC meeting, Session SM2, Montreal, May 14-17, 2006.

Mackie, R.L., Smith, J.T., Madden, T.R., 1994. Three-dimensional electromagnetic modeling using finite difference equations: the magnetotelluric example. Radio Sci. 29, 923–935.

Mackie, R., Booker, J., 1999: Documentation for mtd3fwd and d3_to_mt; 6 pages.

MATAGAMI

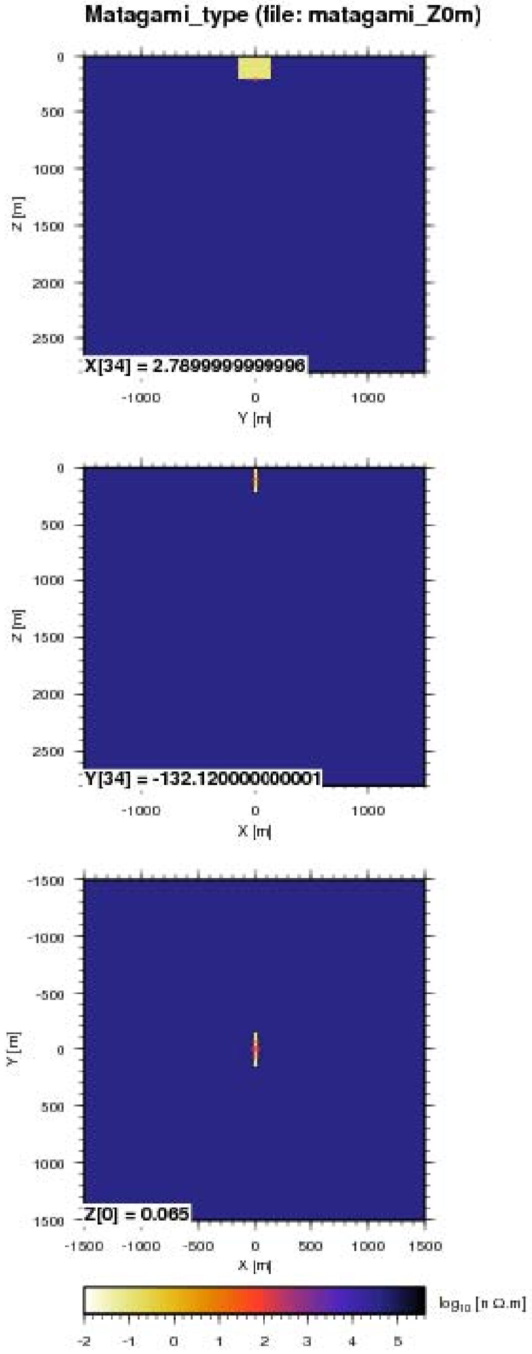

Figure Mat-1: model of Matagami orebody outcropping at ground surface. Resistivities of orebody and host rock are 0.1 Ω.m and 40,000 Ω.m respectively.

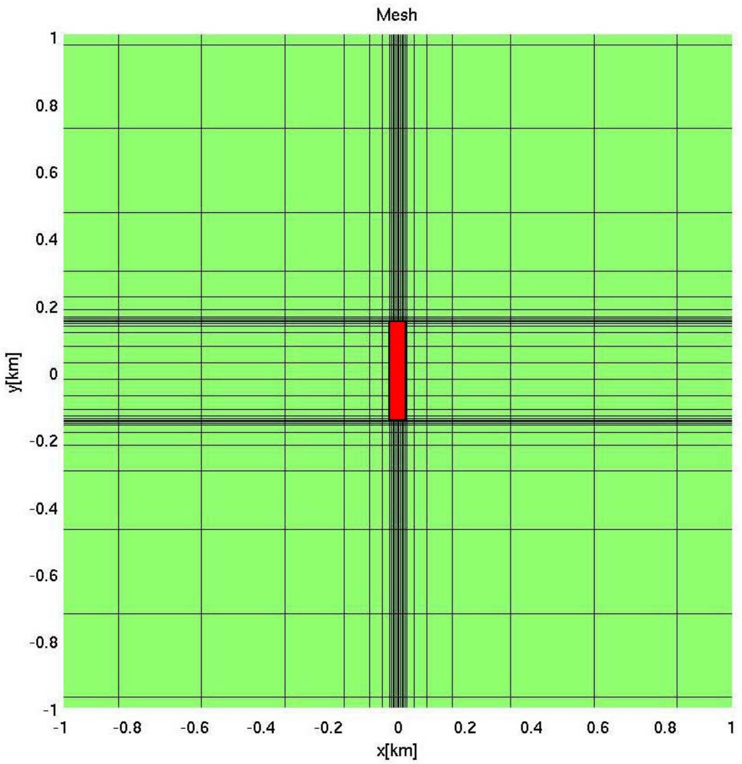

Figure Mat-2: mesh used for modelling the Matagami orebody model in 3D. The red rectangle in the middle of the figure is the vertical projection of the orebody.

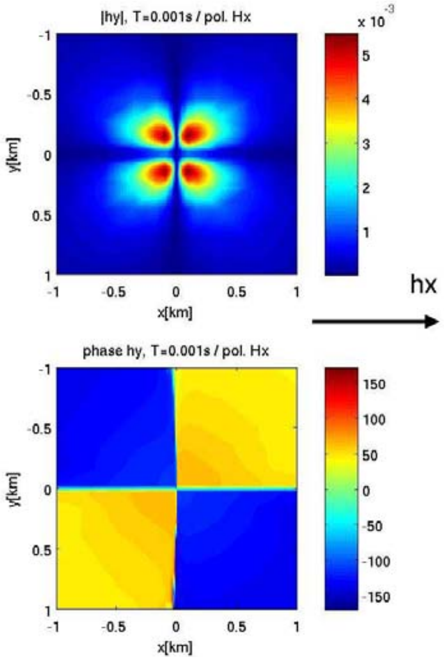

Figure Mat-3: amplitude and phase of Hy magnetic field generated by hx primary field polarization. The Hy field exists only close to the corners of the conductive structure where channelling exists and is zero elsewhere. The phase indicates that the Hy field is in the opposite direction at two neighbouring corners of the structure.

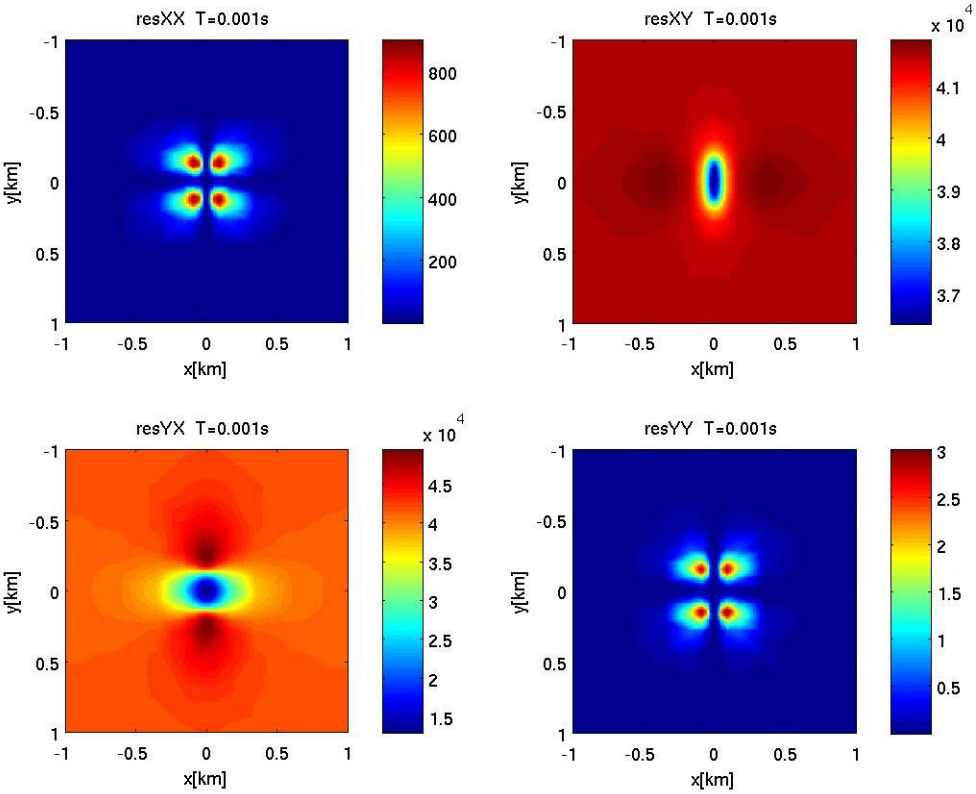

Figure Mat-4: apparent resistivities (Ω.m) at T = 0.001 s (F = 1000 Hz) for each impedance tensor element. The body is displayed as a resistive low in ρ_{xy} and ρ_{yx}.

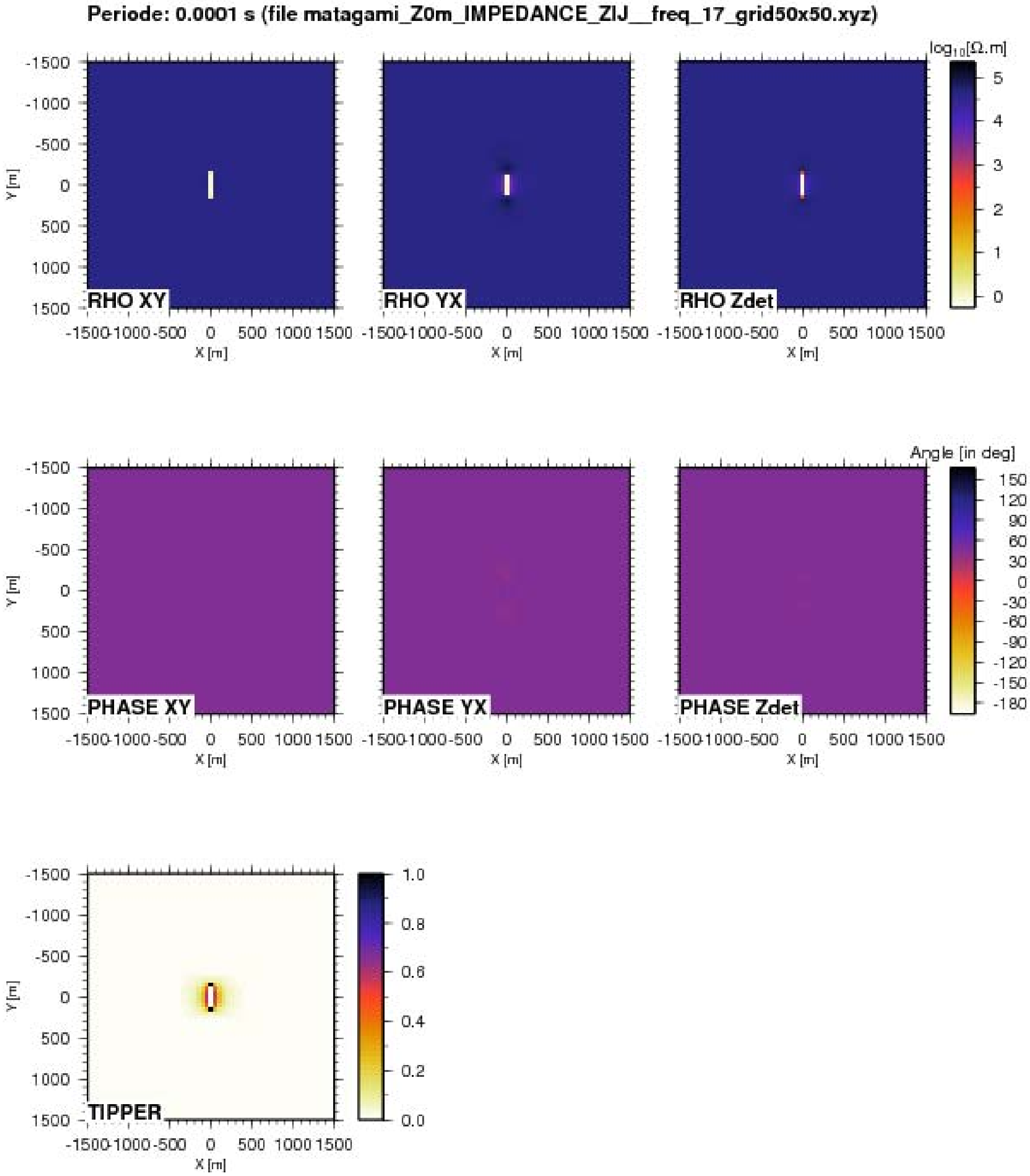

Figure Mat-5: apparent resistivities and phases, and tipper at T = 10^{-4} s (F = 10,000 Hz). Apparent resistivities and phases are shown for the xy, yx and determinant impedances.

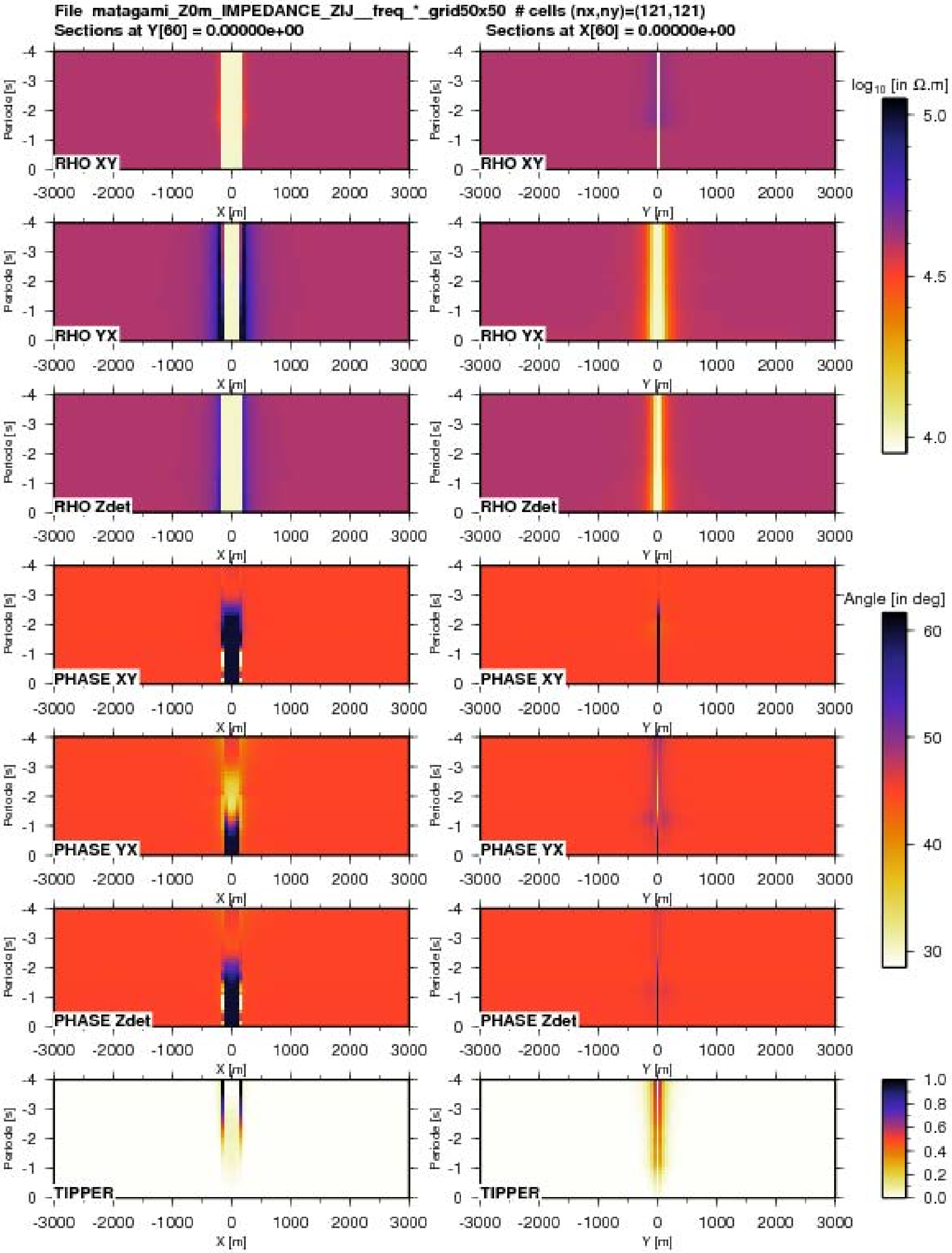

Figure Mat-6: pseudo-sections of apparent resistivities and phases, and tippers for two orthogonal profiles through the center of the outcropping conductive structure.

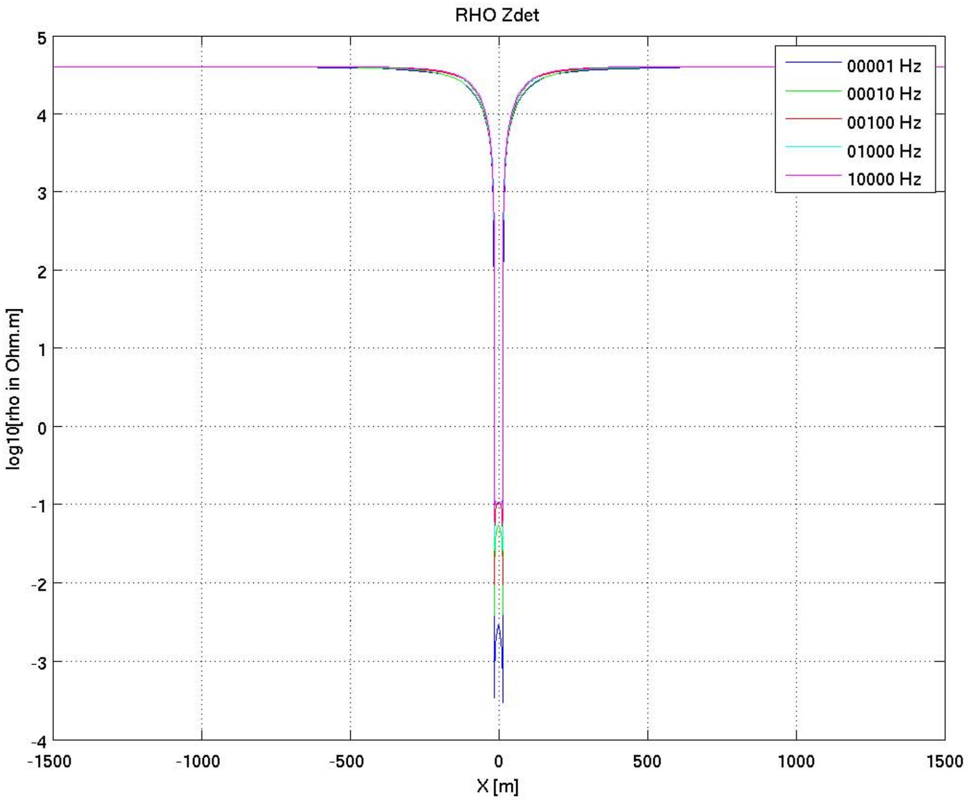

Figure Mat-7: profile y = 0 across the model: apparent resistivity profiles ρ_{det} at selected frequencies for a body at z = 0 m.

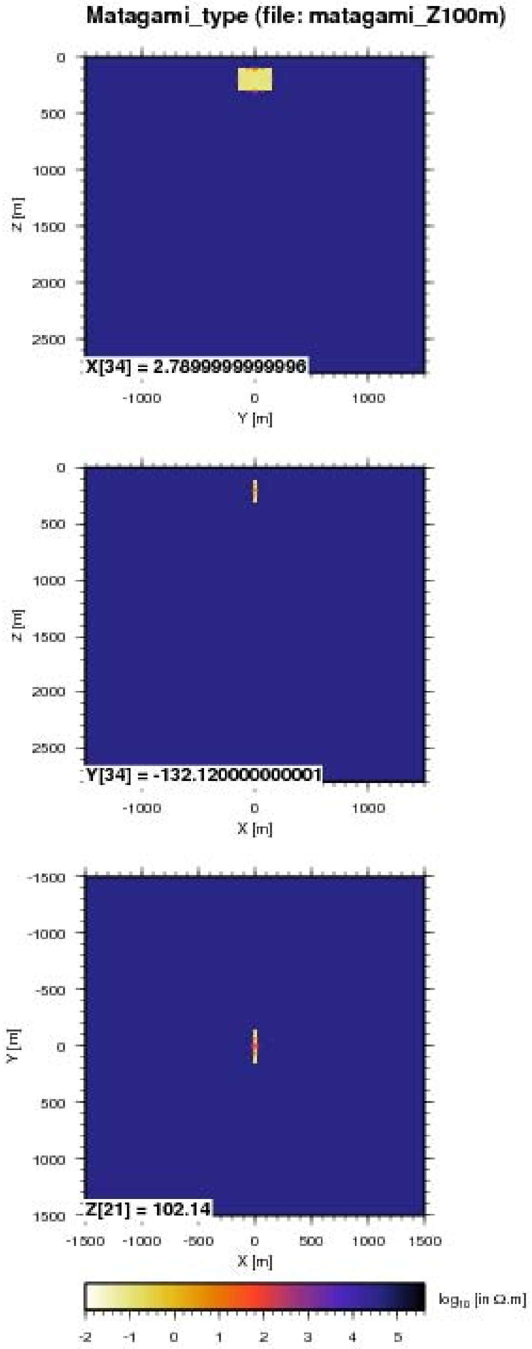

Figure Mat-8: model of Matagami orebody at a depth of 100 m. Resistivities of orebody and host rock are 0.1 Ω.m and 40,000 Ω.m respectively.

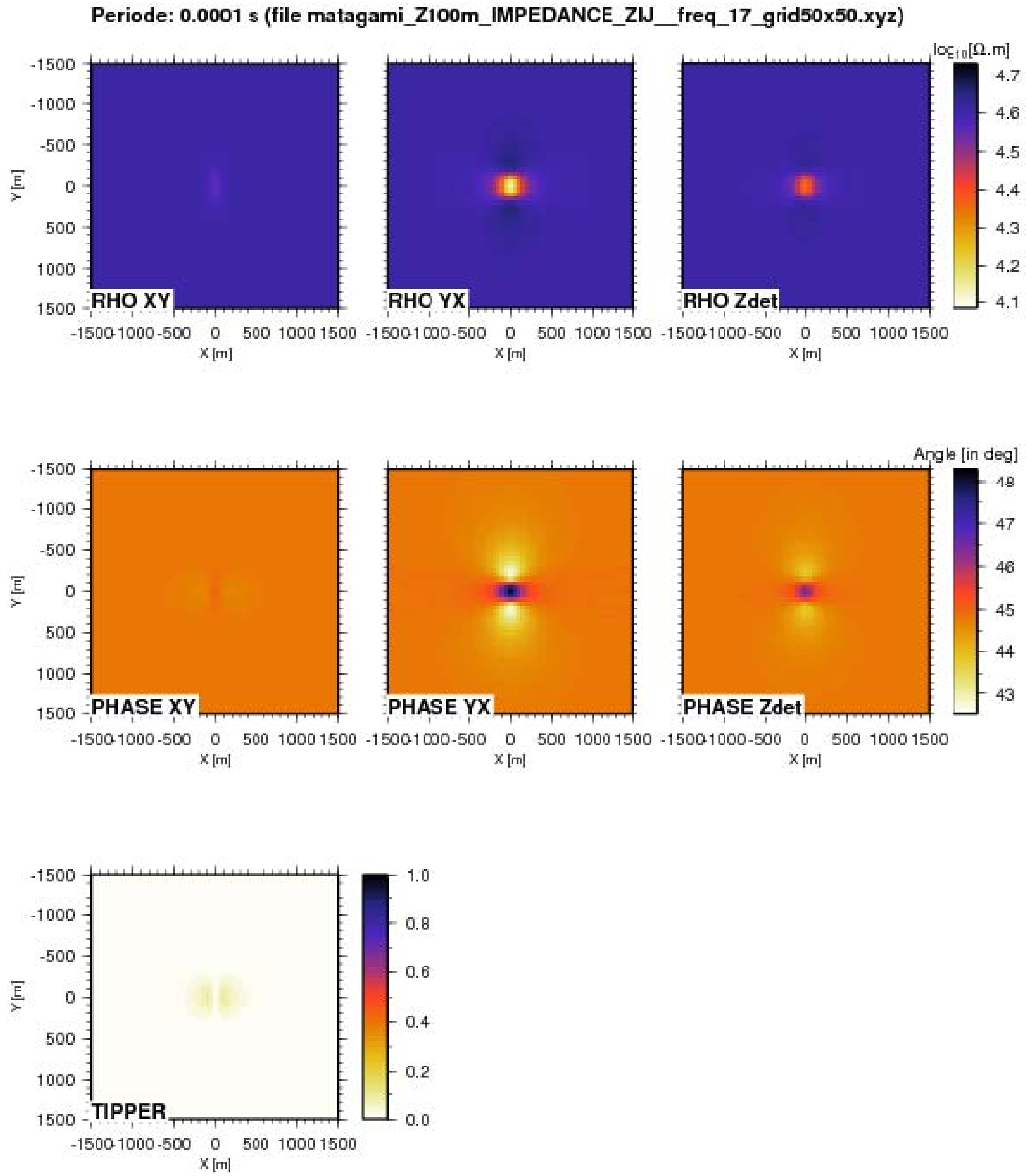

Figure Mat-9: apparent resistivities and phases, and tipper at T = 10^{-4} s (F = 10,000 Hz) for Matagami model at z = 100 m. Apparent resistivities and phases are shown for the xy, yx and determinant impedances.

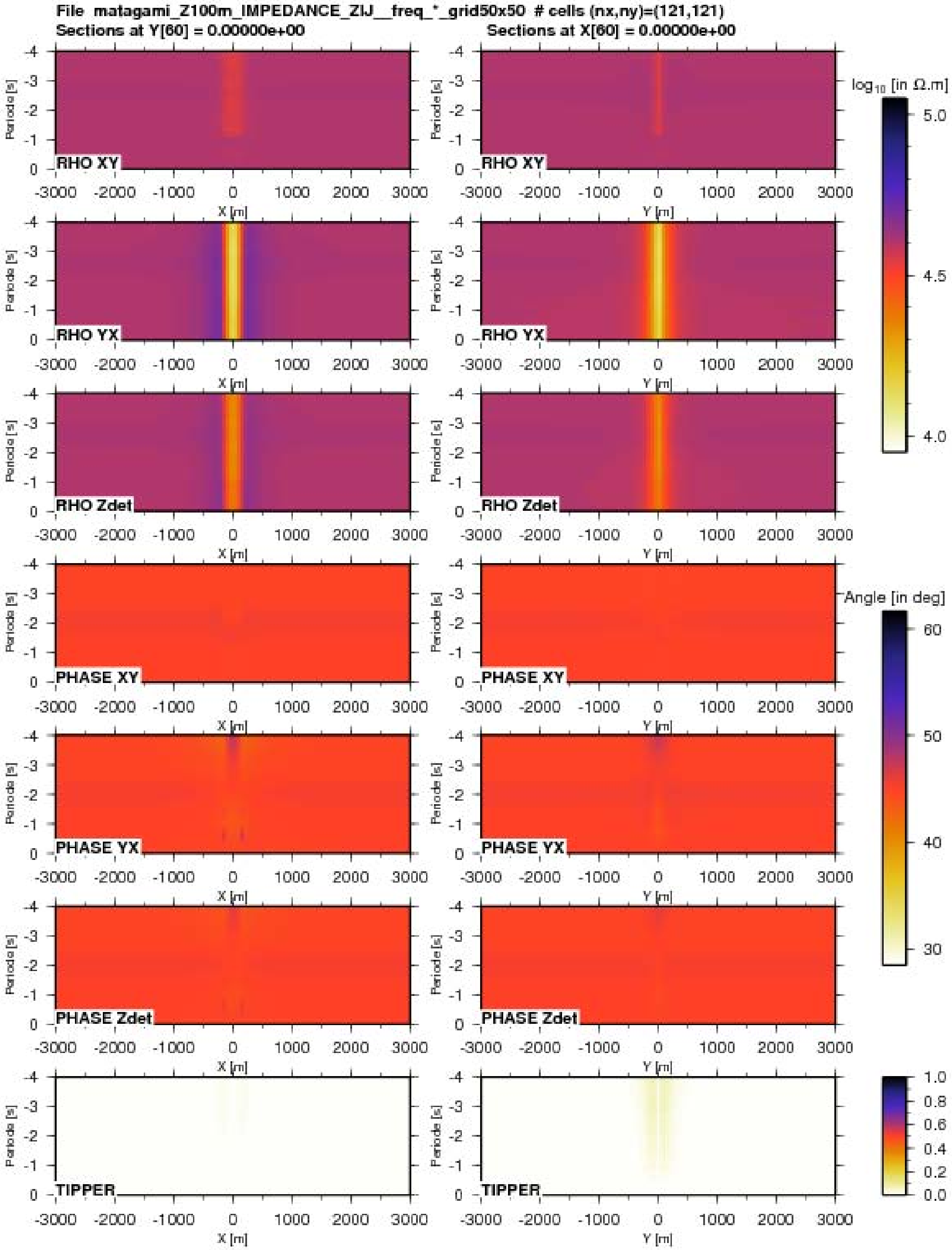

Figure Mat-10: pseudo-sections of apparent resistivities and phases, and tippers for two orthogonal profiles through the center of the outcropping conductive structure located at z = 100 m.

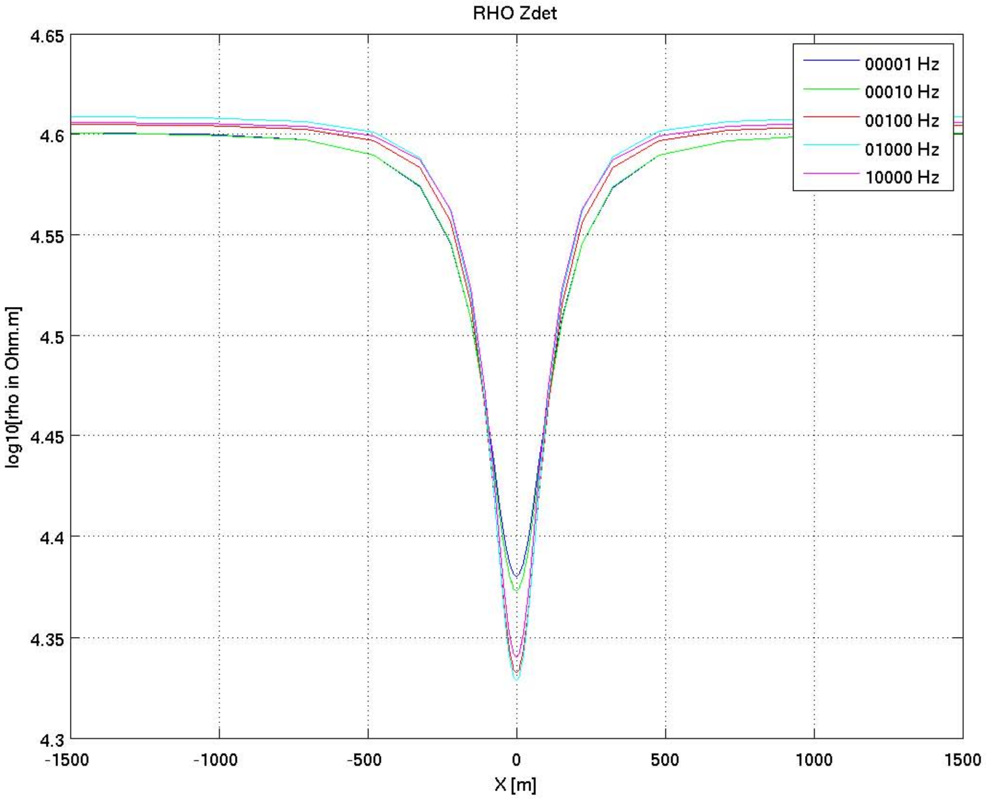

Figure Mat-11: profile y = 0 across the model: apparent resistivity profiles ρ_{det} at selected frequencies for a body at z = 100 m.

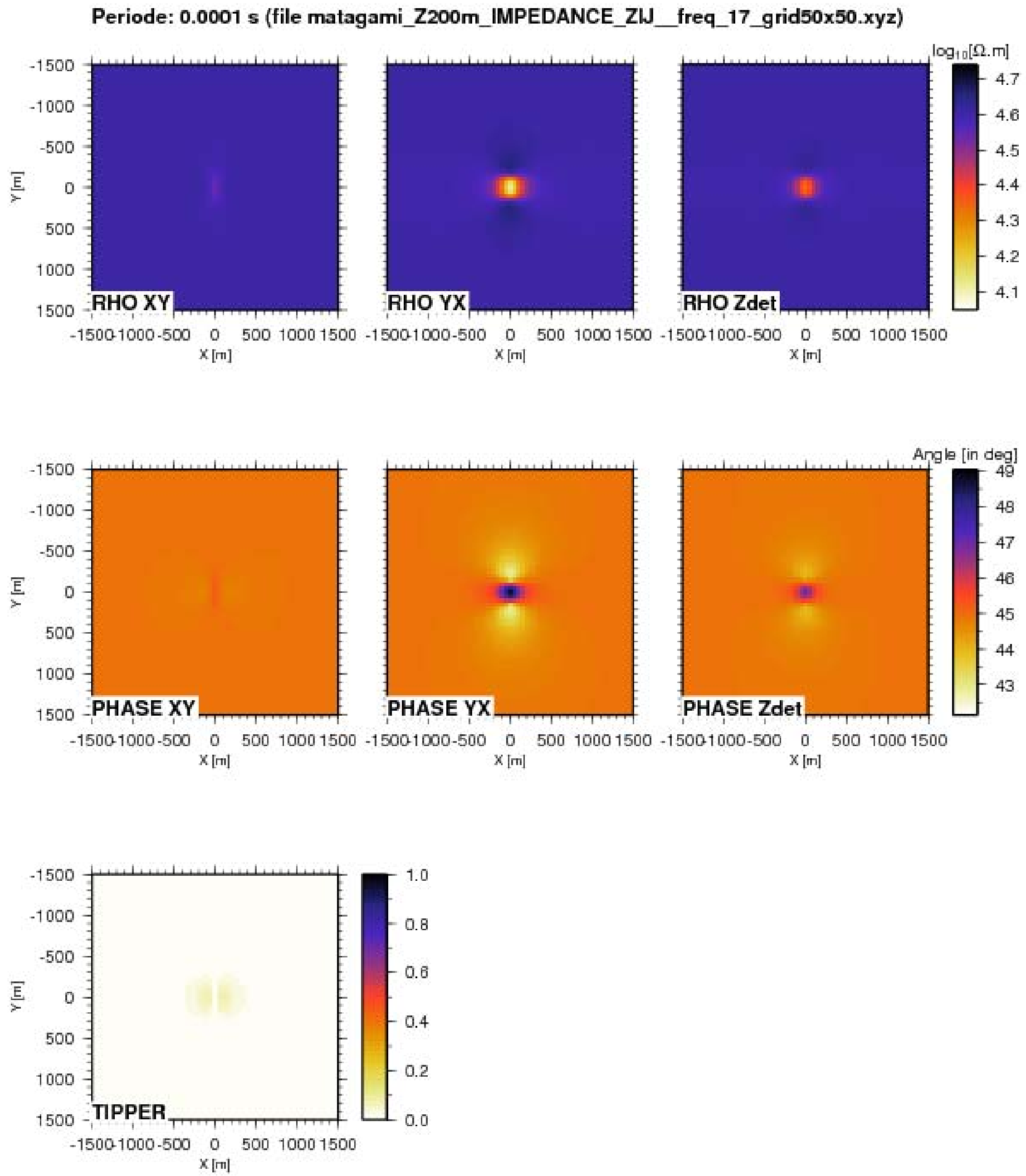

Figure Mat-12: apparent resistivities and phases, and tipper at T = 10^{-4} s (F = 10,000 Hz) for Matagami model at z = 200 m. Apparent resistivities and phases are shown for the xy, yx and determinant impedances.

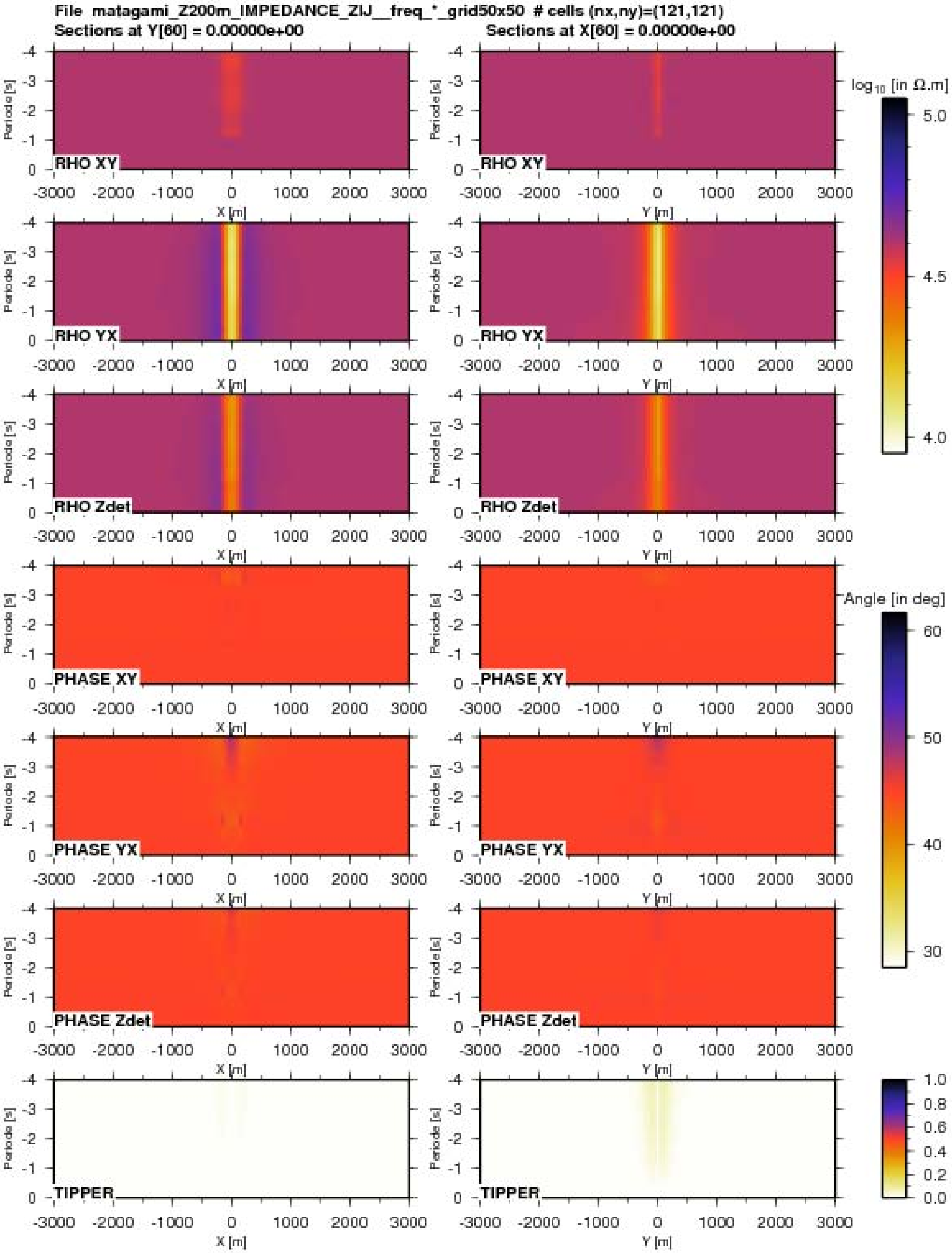

Figure Mat-13: pseudo-sections of apparent resistivities and phases, and tippers for two orthogonal profiles through the center of the outcropping conductive structure located at z = 200 m.

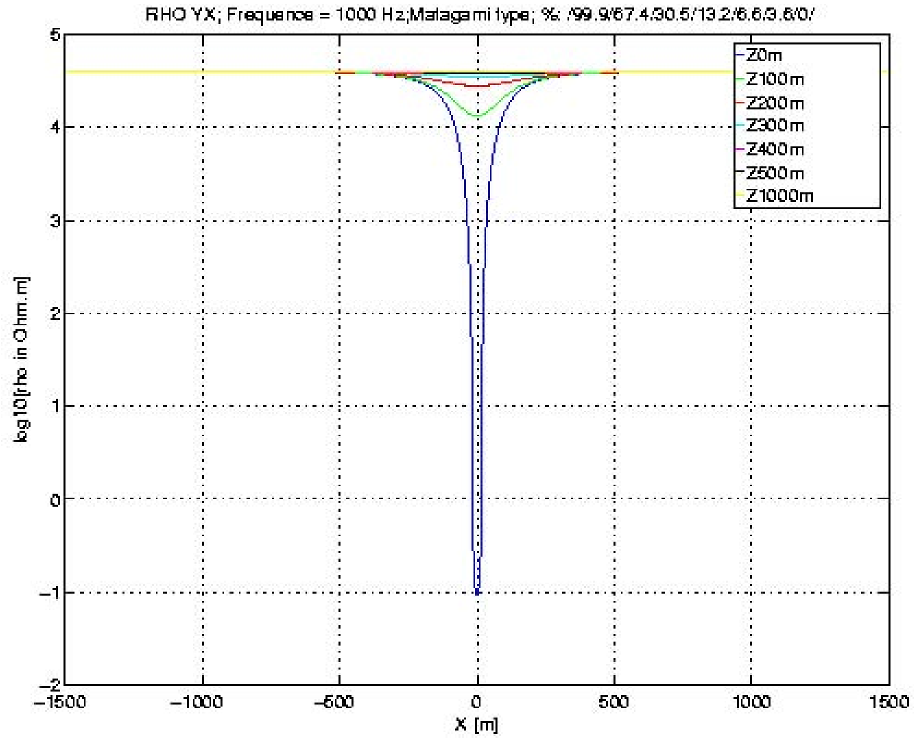

Figure Mat-14: ρ_{yx} profile along X-axis (y = 0) at F = 1000 Hz for various depths.

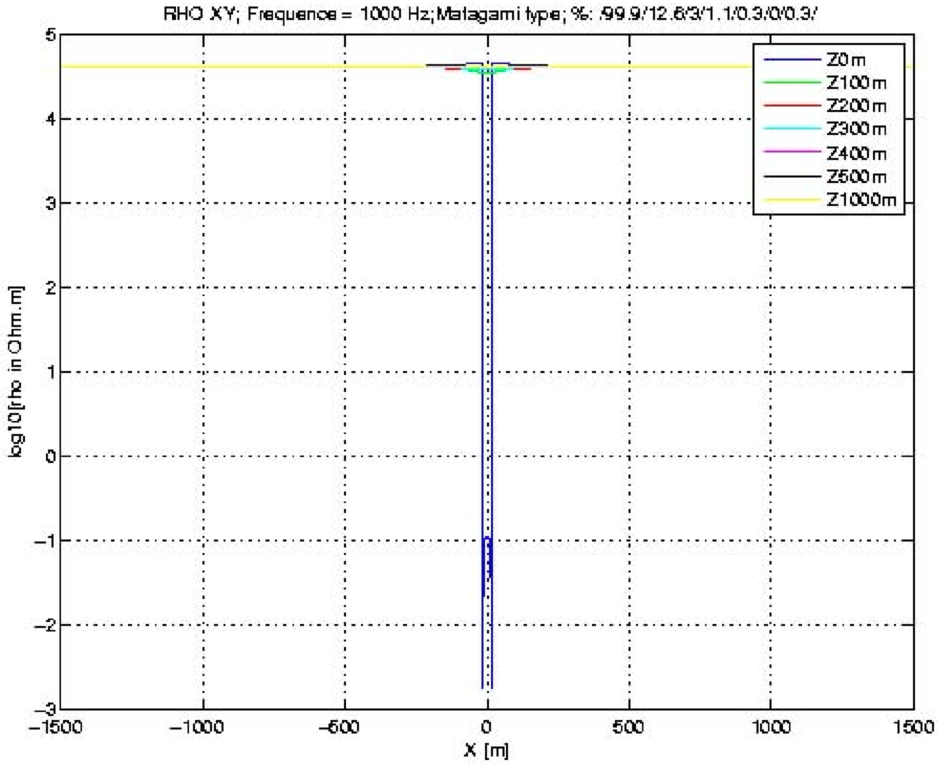

Figure Mat-15: ρ_{xy} profile along X-axis (y = 0) at F = 1000 Hz for various depths.

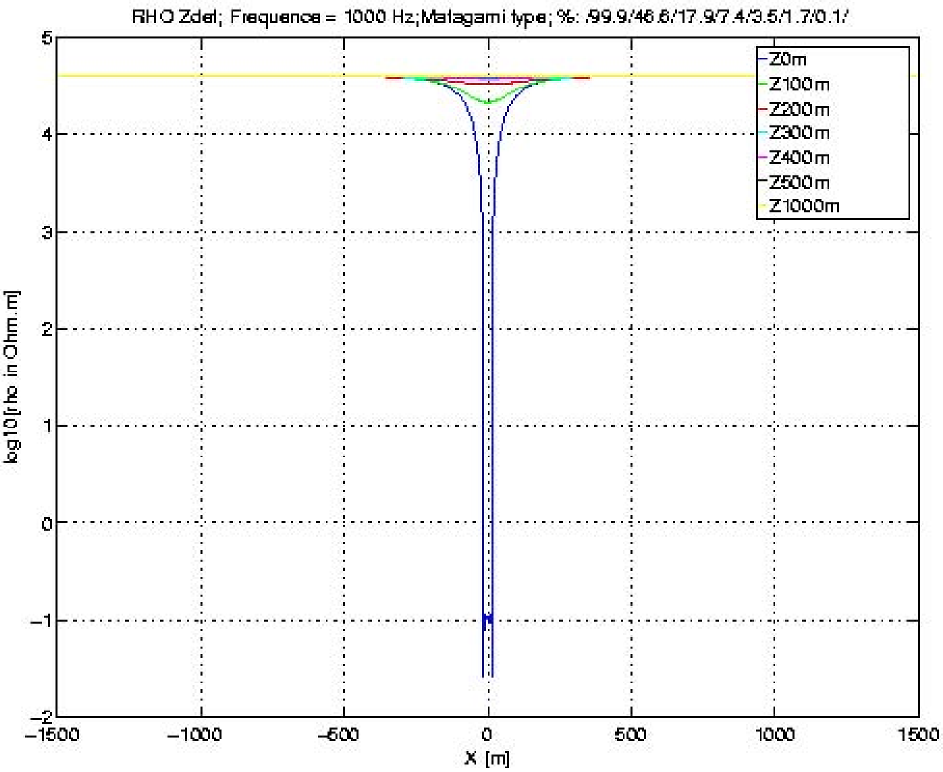

Figure Mat-16: ρ_{det} profile along X-axis (y = 0) at F = 1000 Hz for various depths.

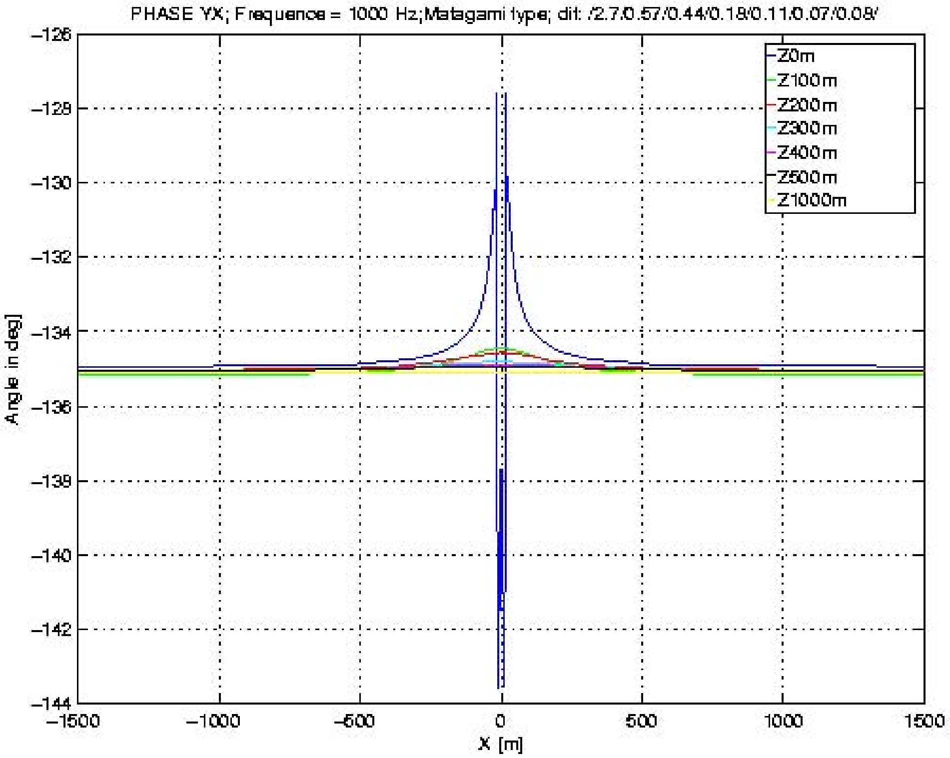

Figure Mat-17: φ_{yx} profile along X-axis (y = 0) at F = 1000 Hz for various depths.

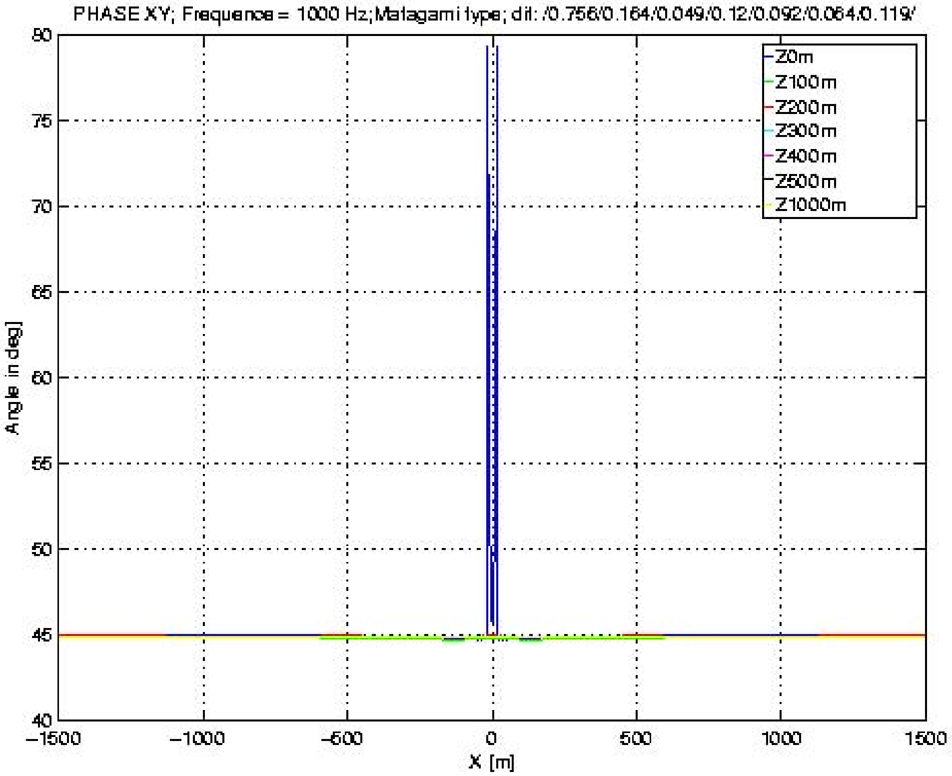

Figure Mat-18: φ_{xy} profile along X-axis (y = 0) at F = 1000 Hz for various depths.

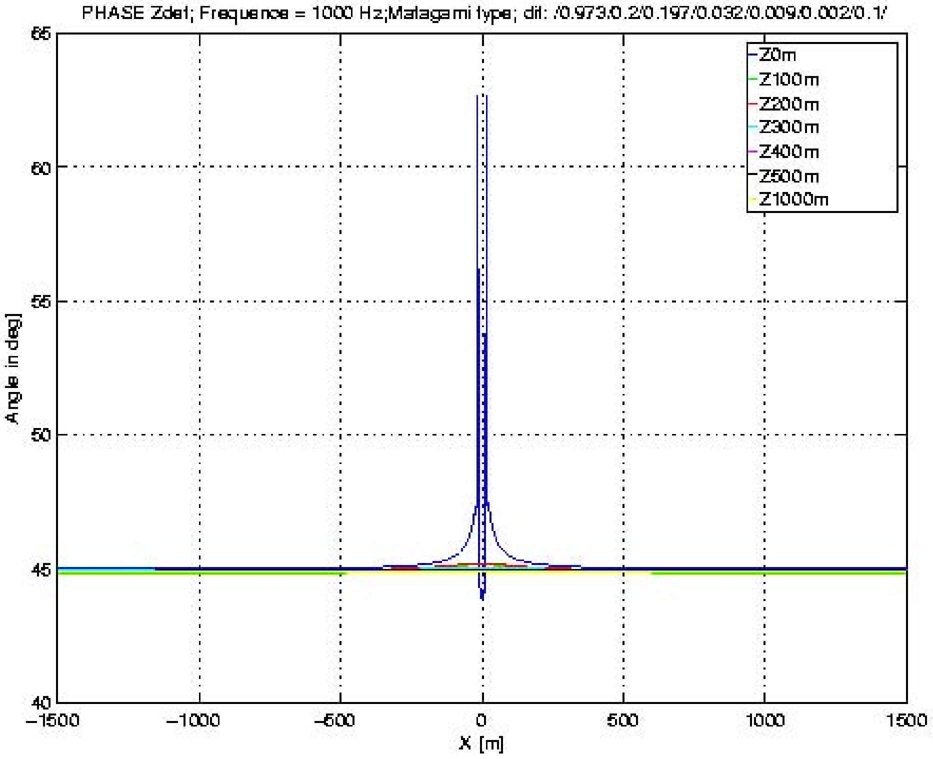

Figure Mat-19: φ_{det} profile along X-axis (y = 0) at F = 1000 Hz for various depths.

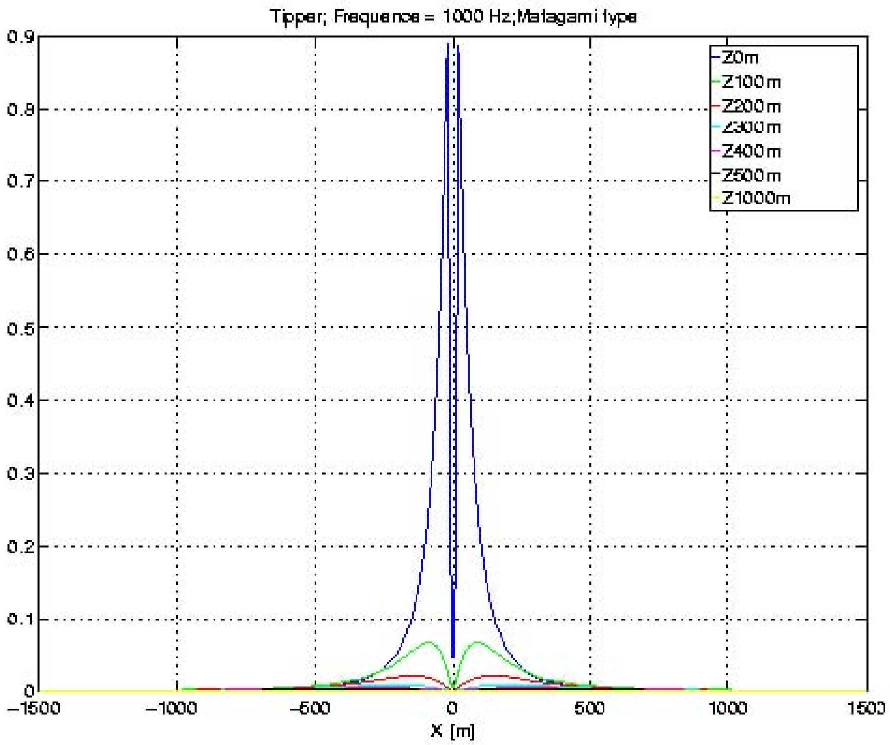

Figure Mat-20: tipper profile along X-axis (y = 0) at F = 1000 Hz for various depths.

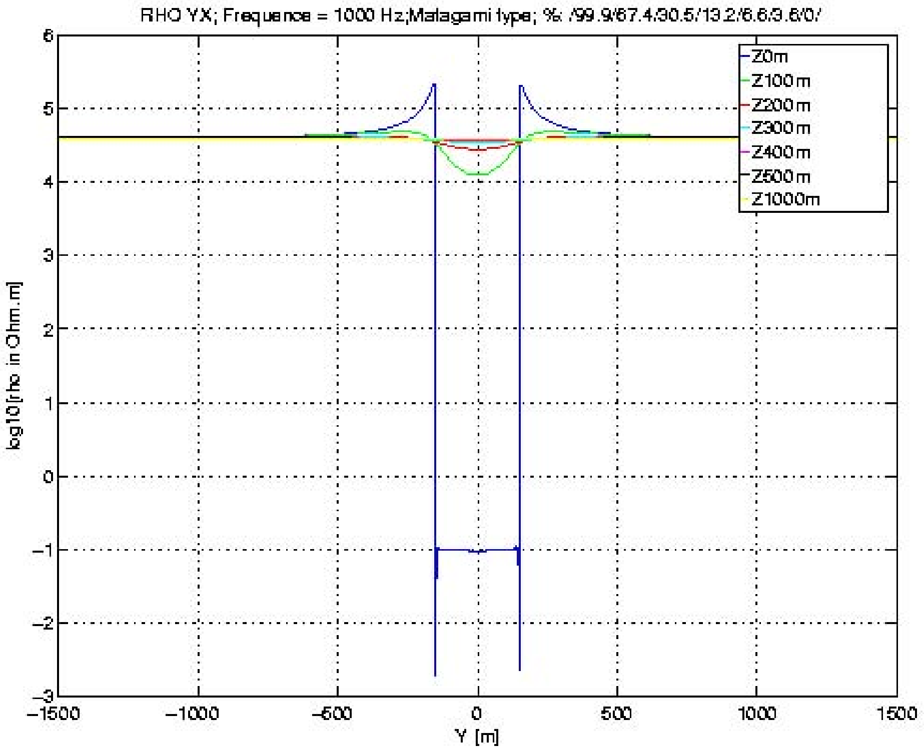

Figure Mat-21: ρ_{yx} profile along Y-axis (x = 0) at F = 1000 Hz for various depths.

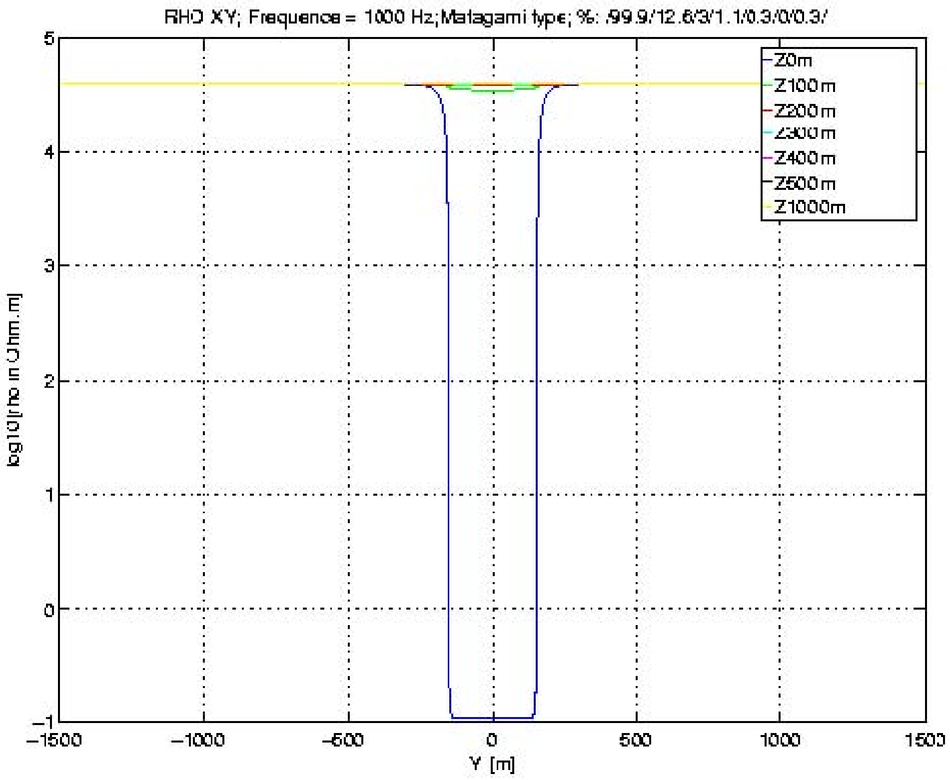

Figure Mat-22: ρ_{xy} profile along Y-axis (x = 0) at F = 1000 Hz for various depths.

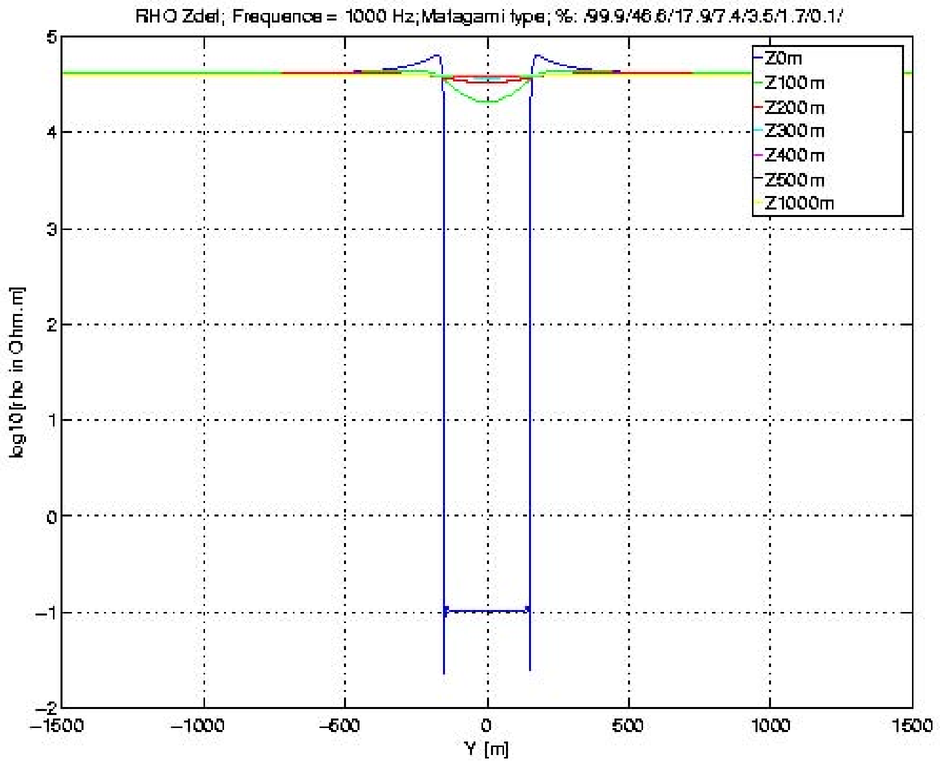

Figure Mat-23: ρ_{det} profile along Y-axis (x = 0) at F = 1000 Hz for various depths.

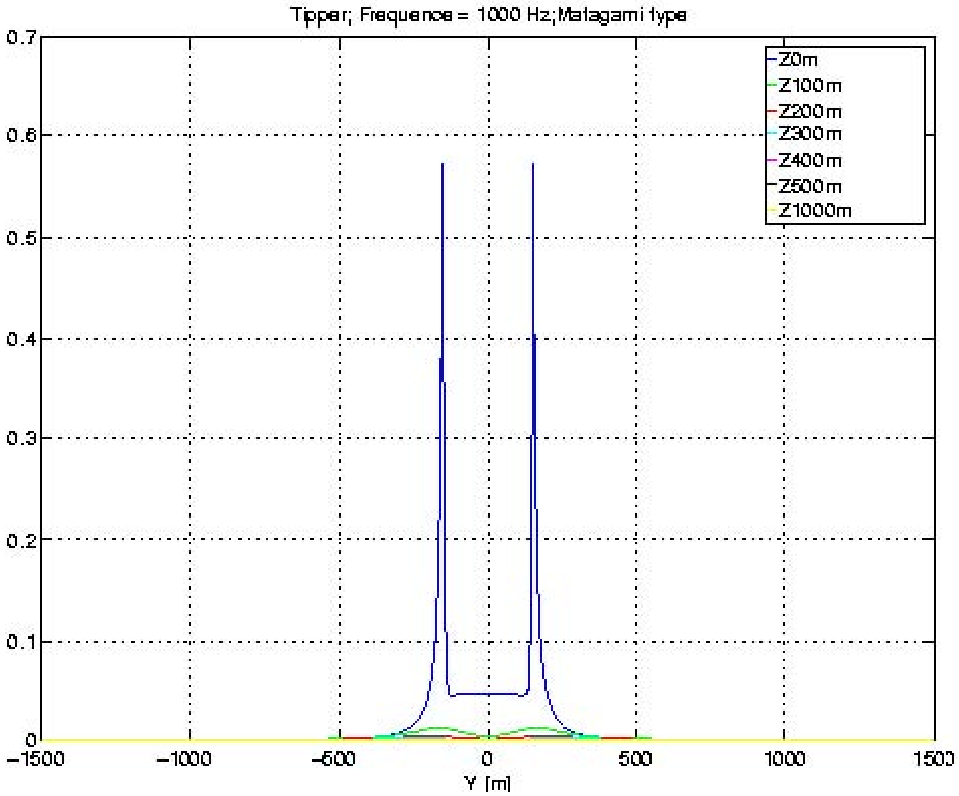

Figure Mat-24: tipper profile along Y-axis (x = 0) at F = 1000 Hz for various depths.

VMS1

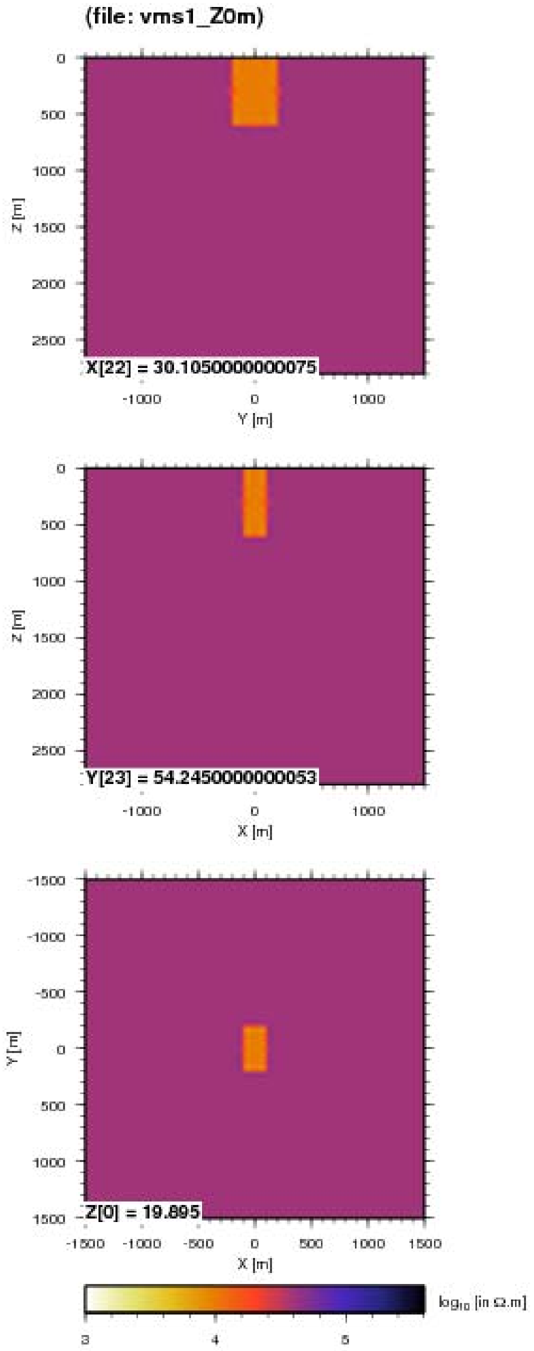

Figure VMS1-1: model of an alteration zone of 10,000 Ω.m in a resistive host rock (40,000 Ω.m). Dimensions are Ly = 400 m, L x=200m and Lz = 600 m.

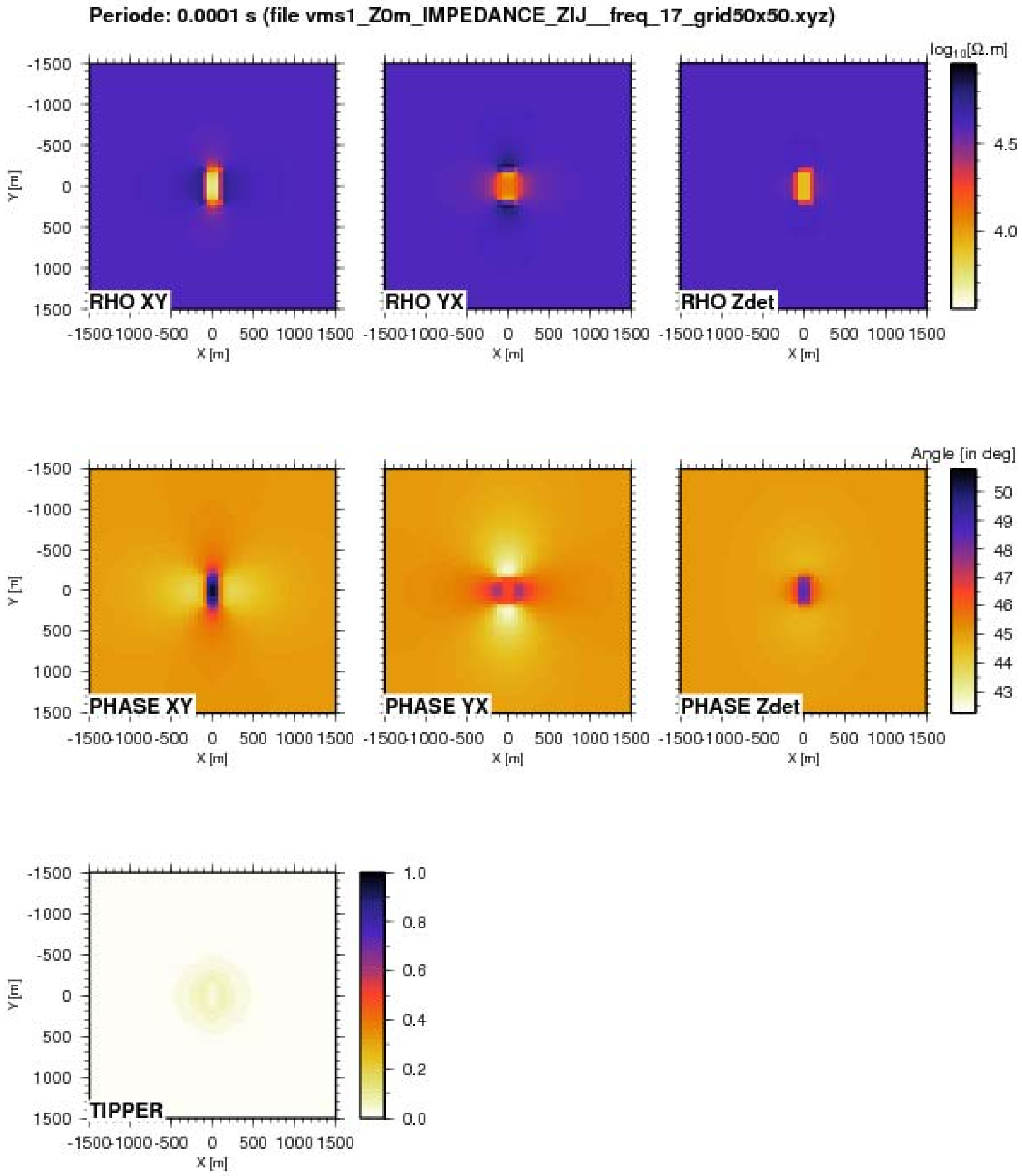

Figure VMS1-2: apparent resistivities and phases, and tipper at T = 10^{-4} s (F = 10,000 Hz). Apparent resistivities and phases are shown for the xy, yx and determinant impedances. Depth z =0 m.

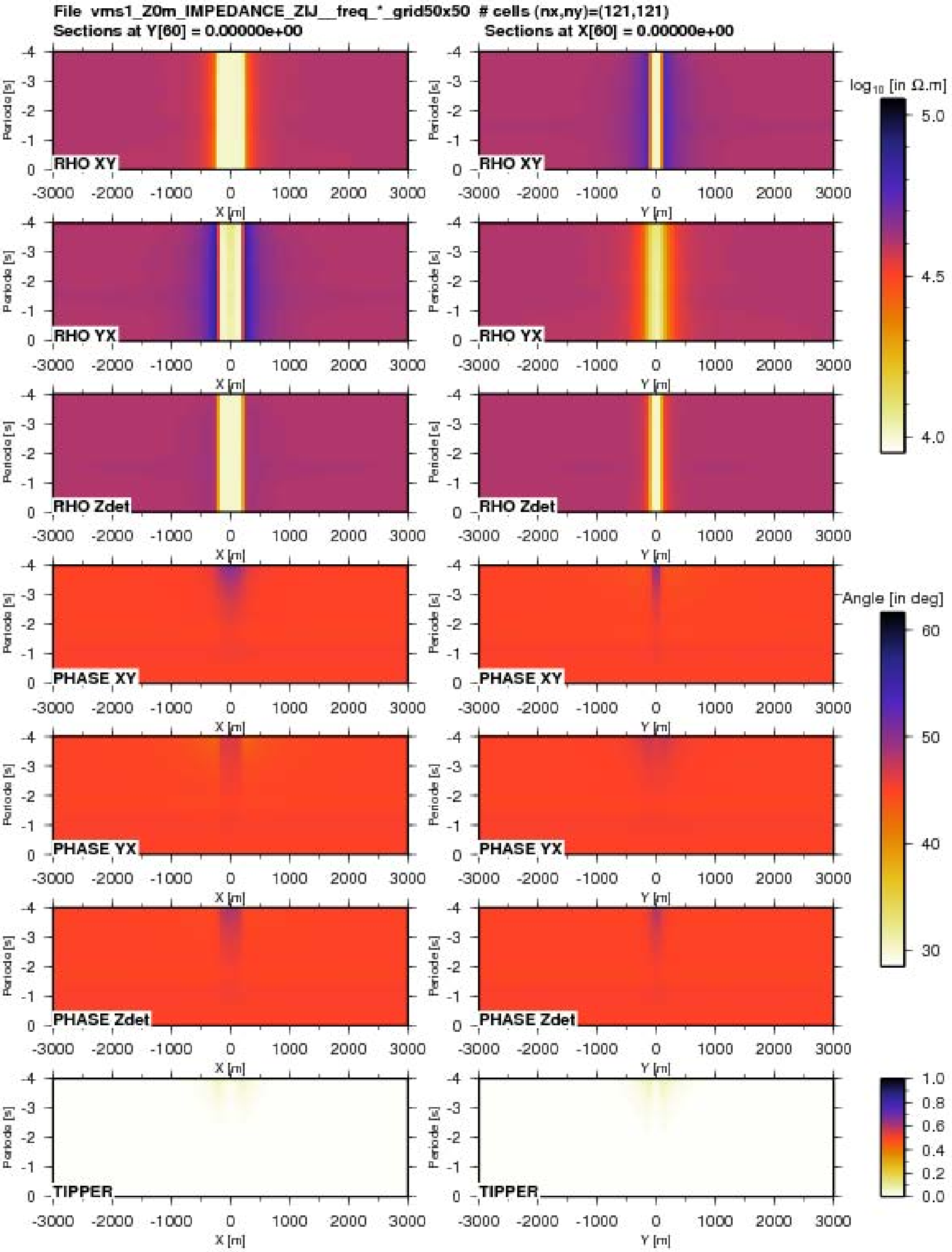

Figure VMS1-3: pseudo-sections of apparent resistivities and phases, and tippers for two orthogonal profiles through the center of the outcropping conductive structure (z = 0 m).

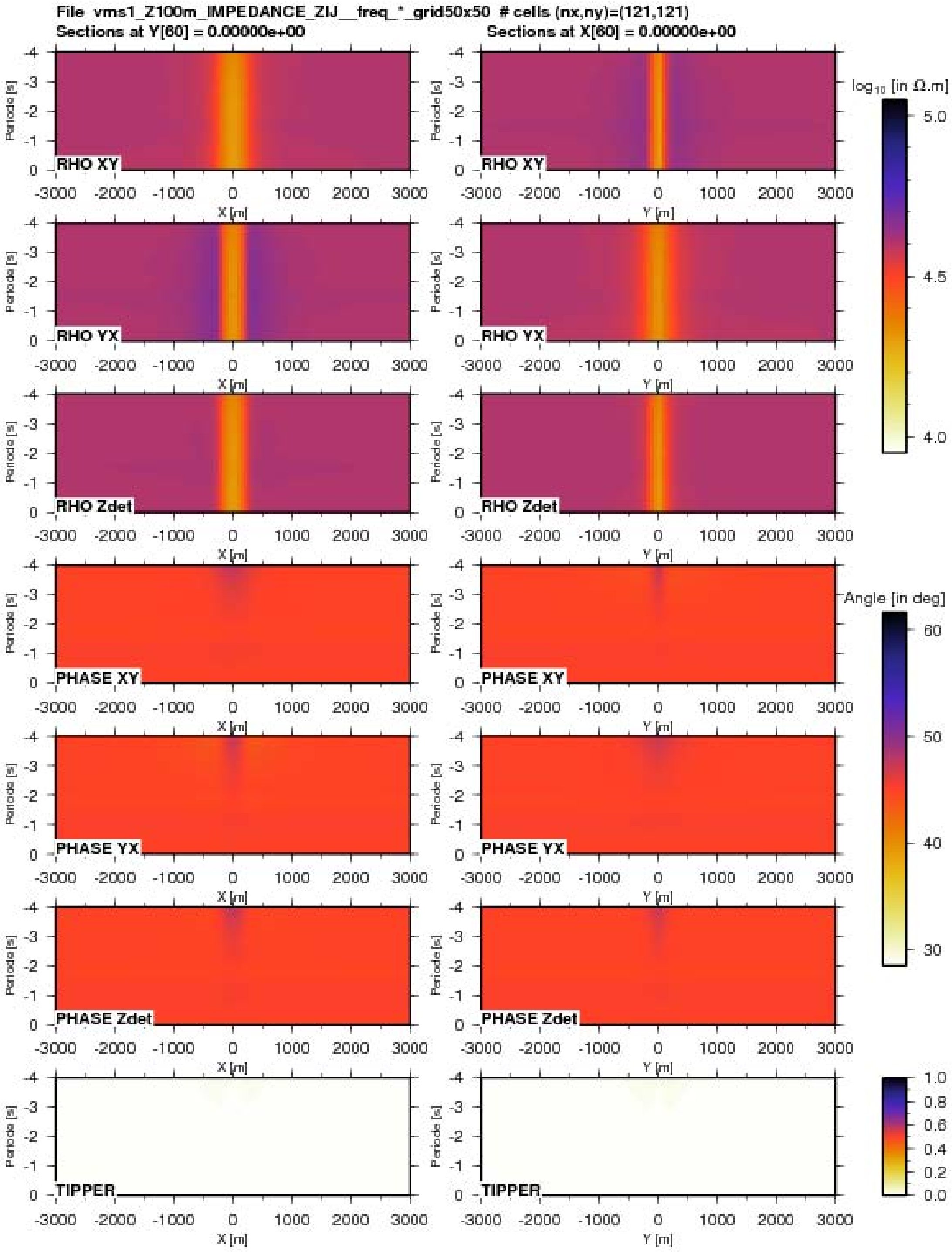

Figure VMS1-4: pseudo-sections of apparent resistivities and phases, and tippers for two orthogonal profiles through the center of the conductive structure (z = 100 m).

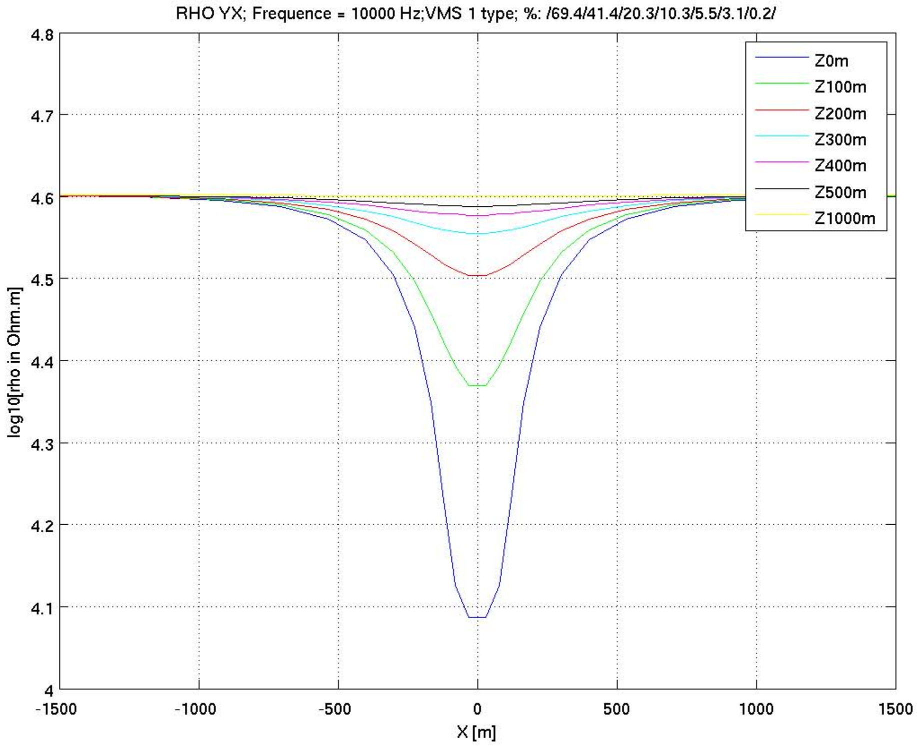

Figure VMS1-5: ρ_{yx} profile along X-axis (y = 0) at F = 10,000 Hz for various depths.

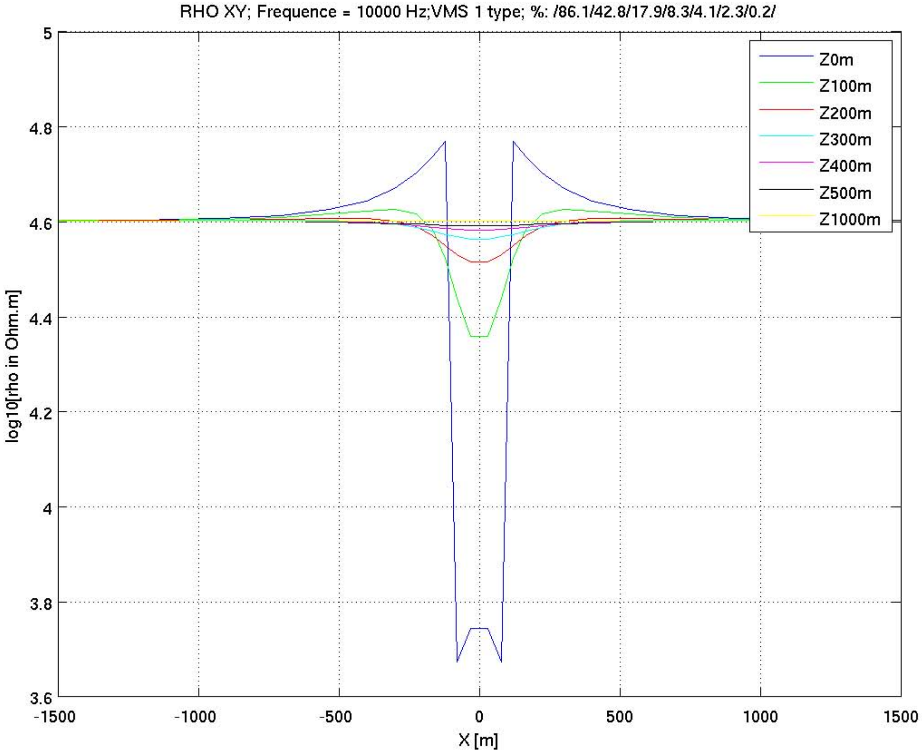

Figure VMS1-6: ρ_{xy} profile along X-axis (y = 0) at F = 10,000 Hz for various depths.

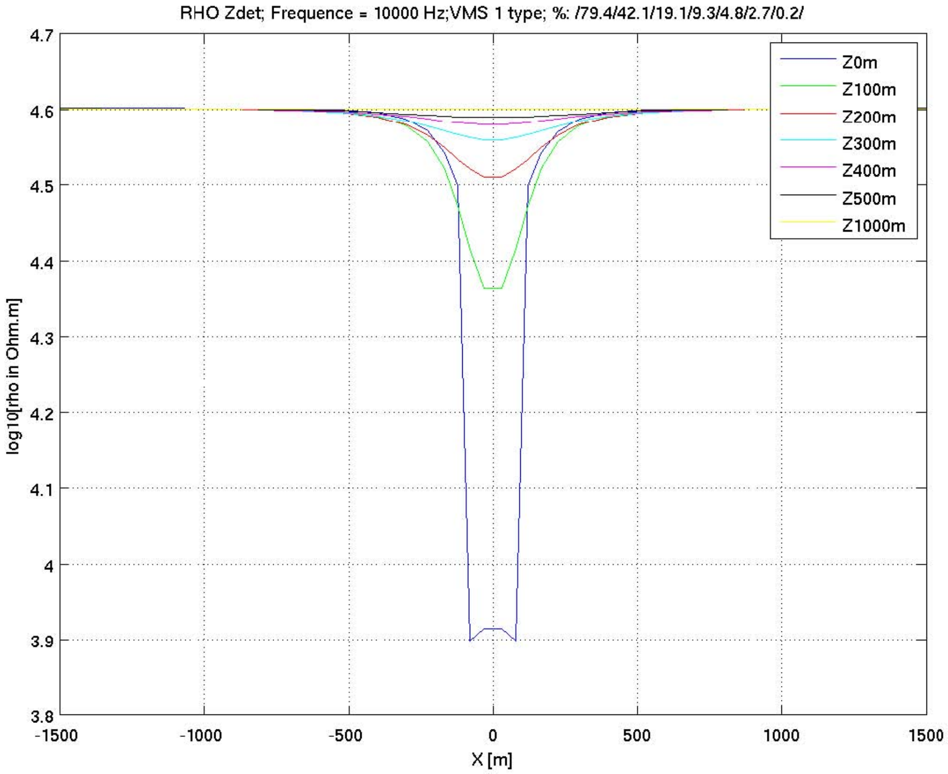

Figure VMS1-7: ρ_{det} profile along X-axis (y = 0) at F = 10,000 Hz for various depths.

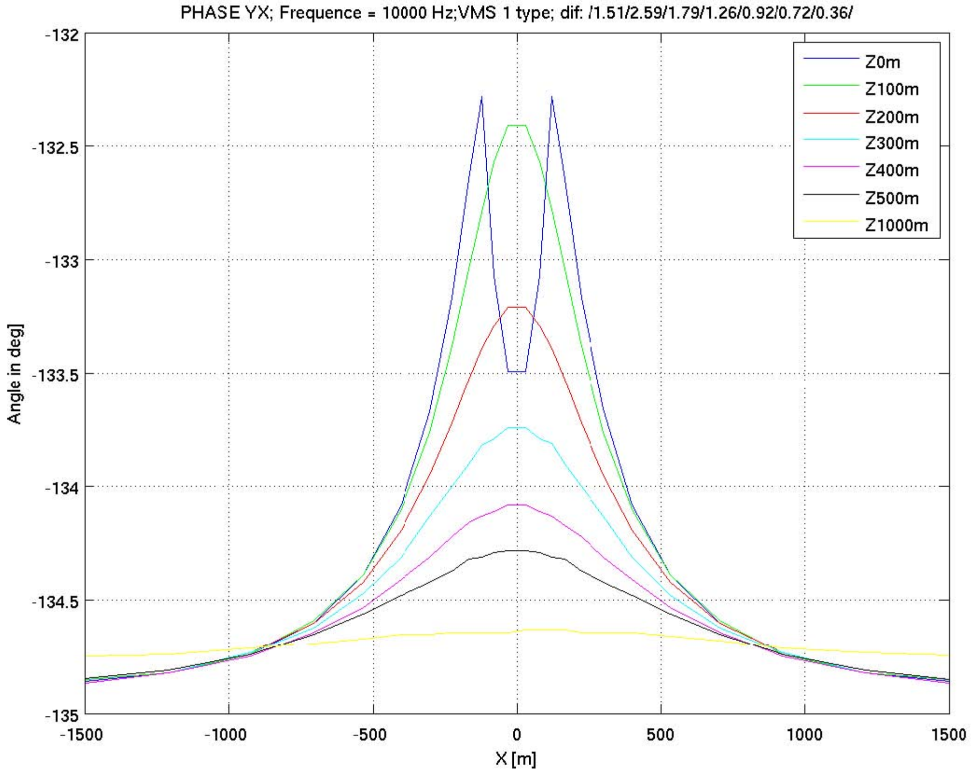

Figure VMS1-8: φ_{yx} profile along X-axis (y = 0) at F = 10,000 Hz for various depths.

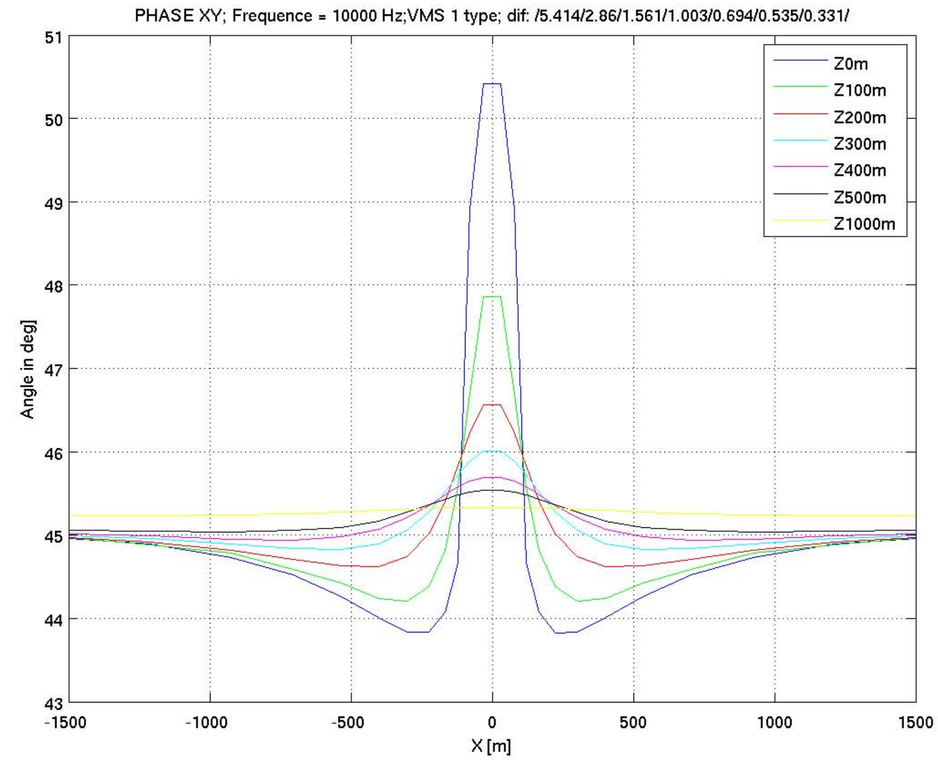

Figure VMS1-9: φ_{xy} profile along X-axis (y = 0) at F = 10,000 Hz for various depths.

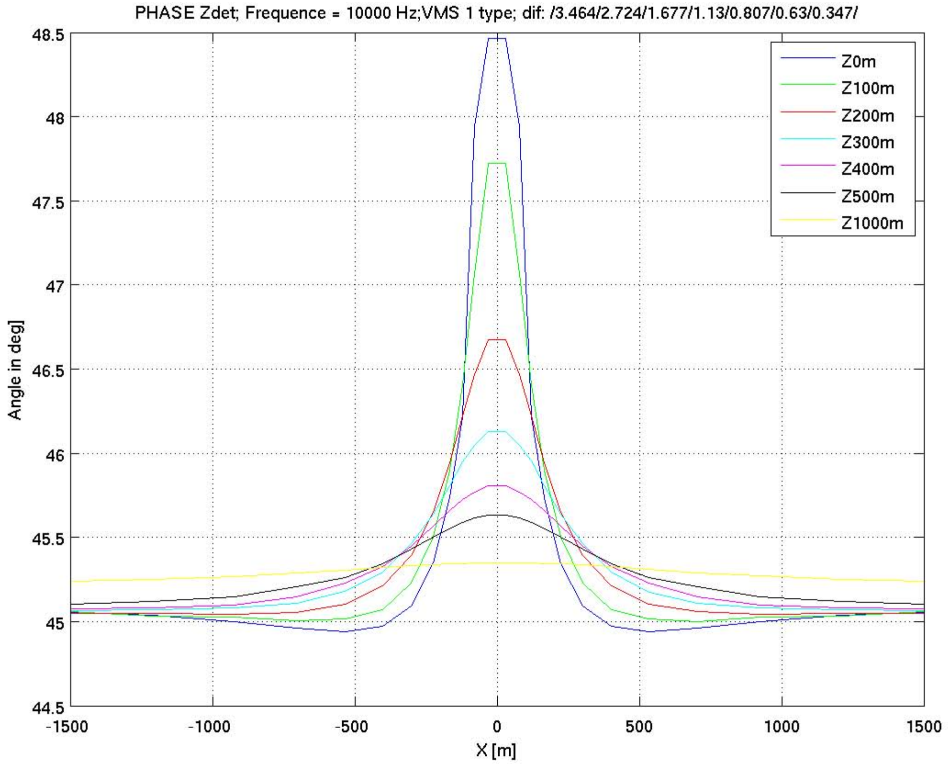

Figure VMS1-10: φ_{det} profile along X-axis (y = 0) at F = 10,000 Hz for various depths.

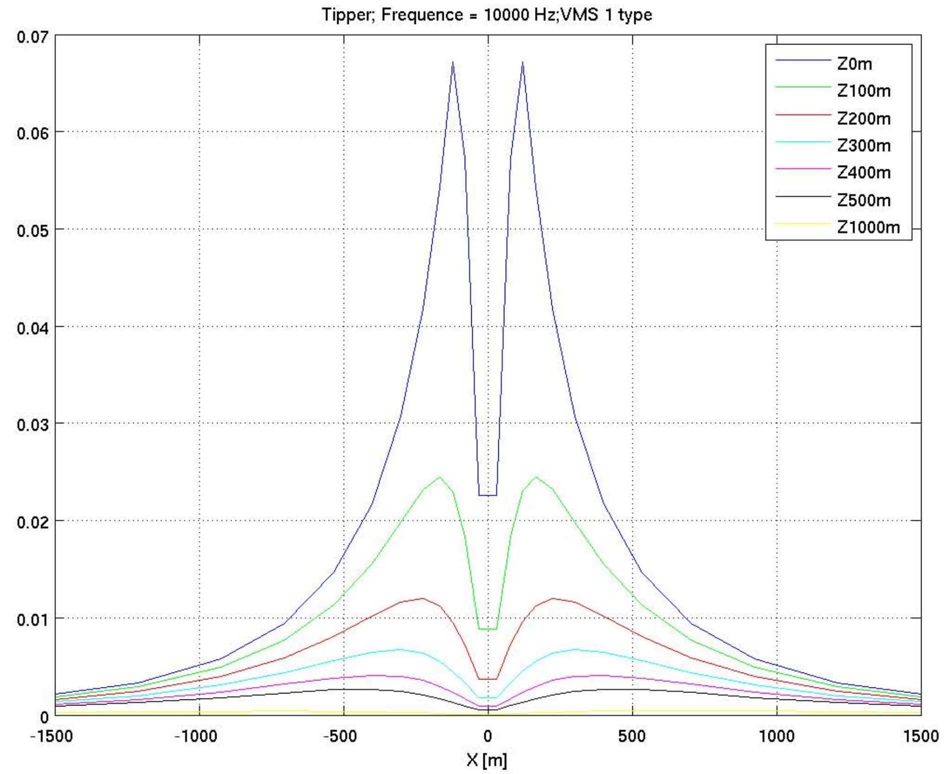

Figure VMS1-11: tipper profile along X-axis (y = 0) at F = 10,000 Hz for various depths.

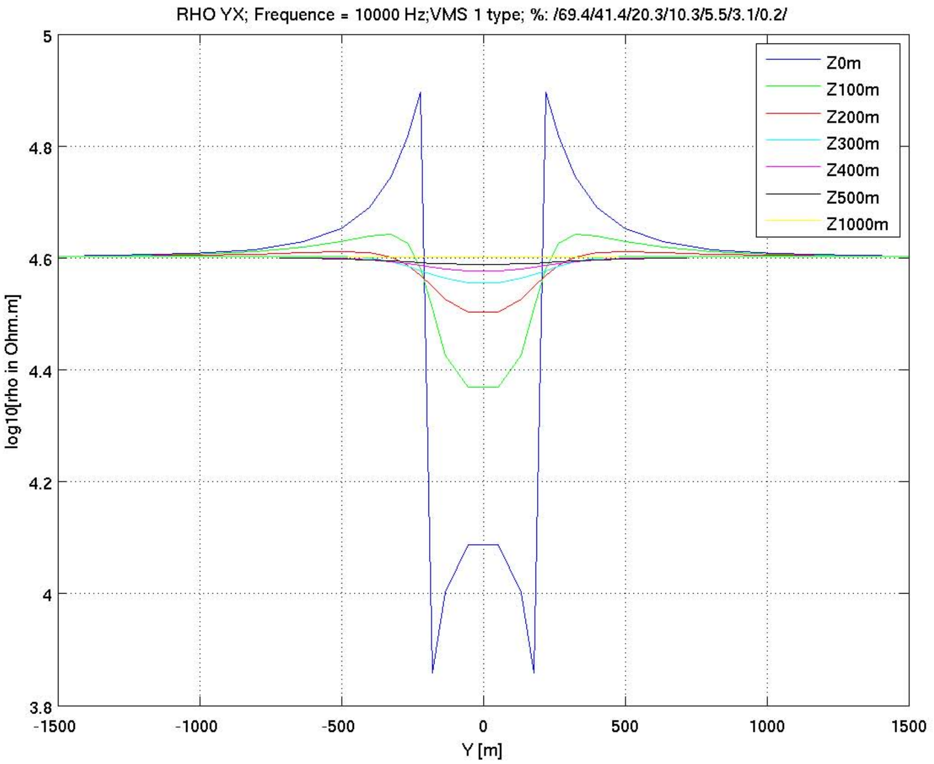

Figure VMS1-12: ρ_{yx} profile along Y-axis (x = 0) at F = 10,000 Hz for various depths.

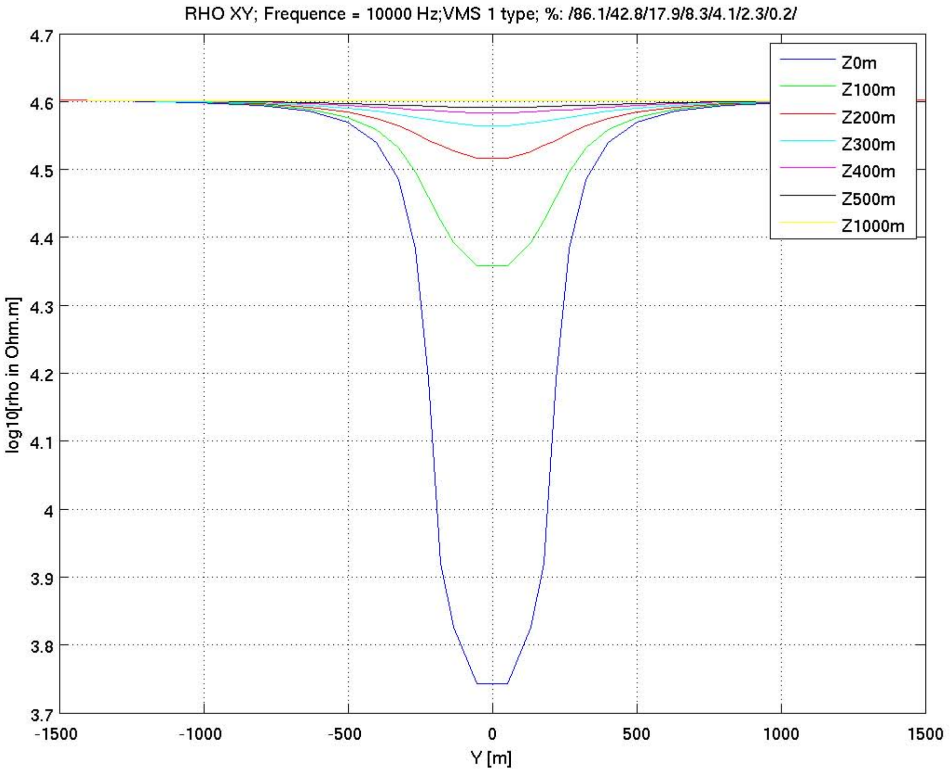

Figure VMS1-13: ρ_{xy} profile along Y-axis (x = 0) at F = 10,000 Hz for various depths.

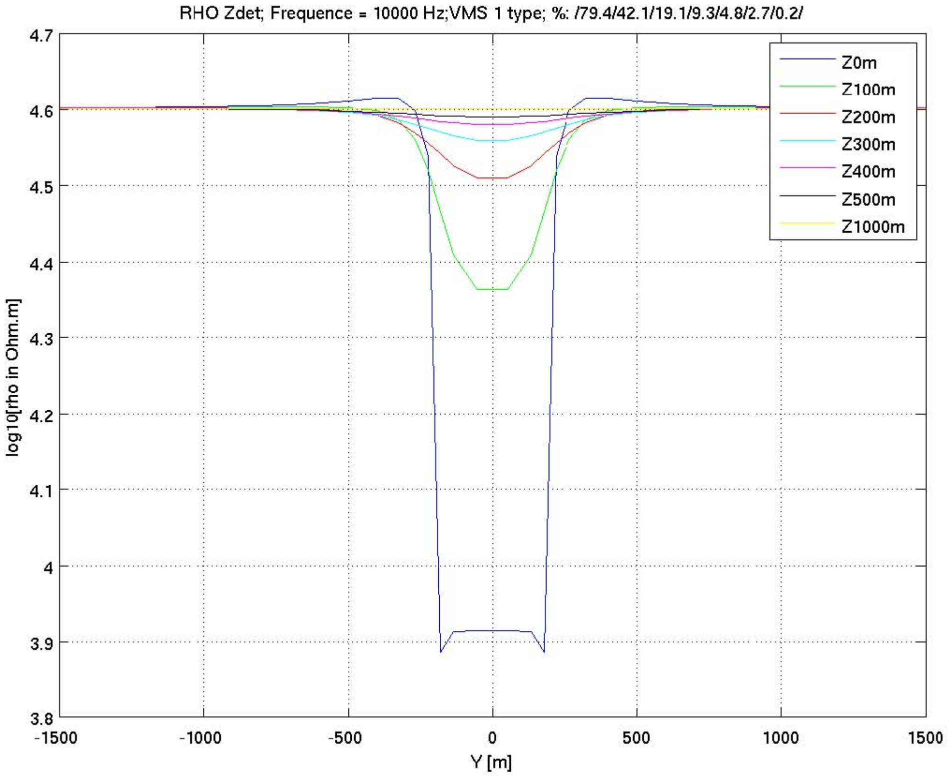

Figure VMS1-14: ρ_{det} profile along Y-axis (x = 0) at F = 10,000 Hz for various depths.

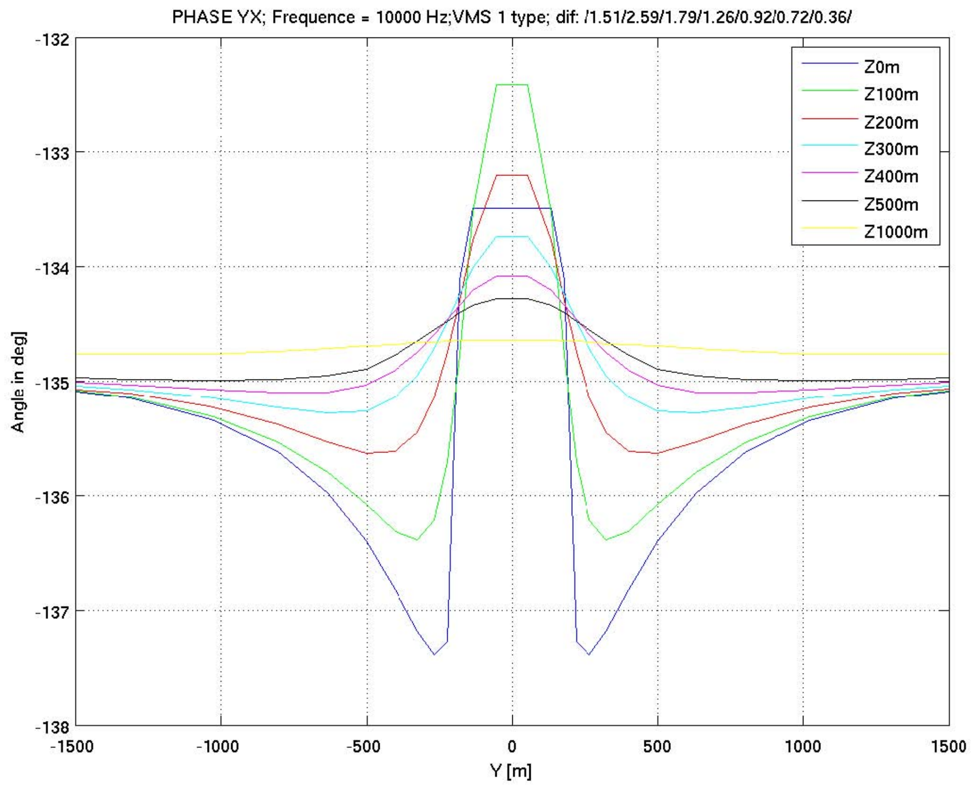

Figure VMS1-15: φ_{yx} profile along Y-axis (x = 0) at F = 10,000 Hz for various depths.

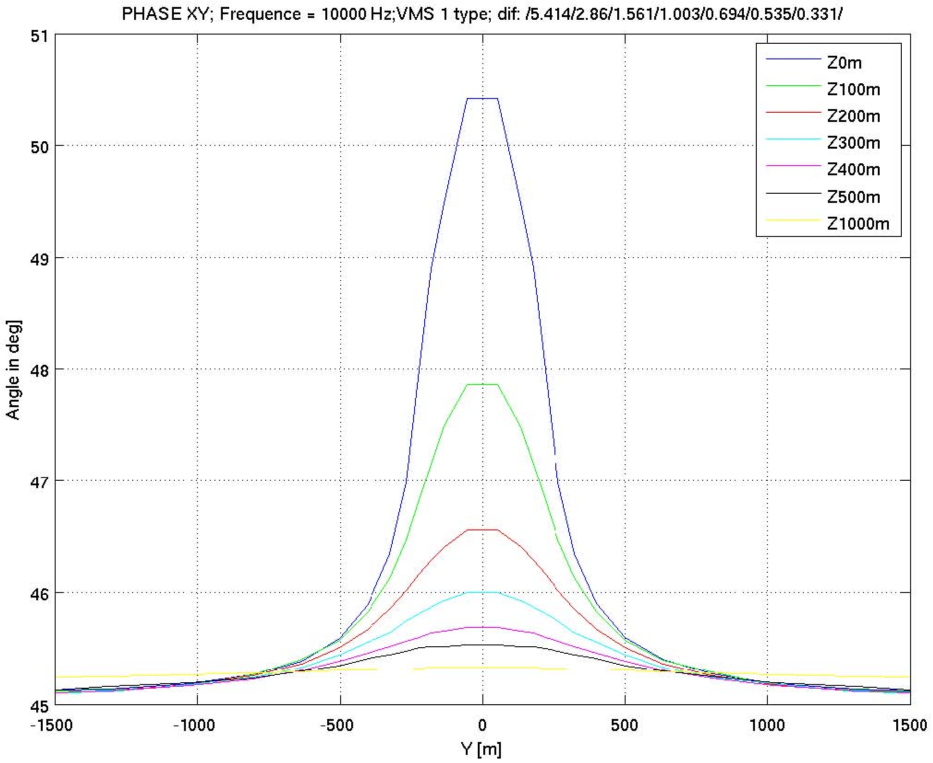

Figure VMS1-16: φ_{xy} profile along Y-axis (x = 0) at F = 10,000 Hz for various depths.

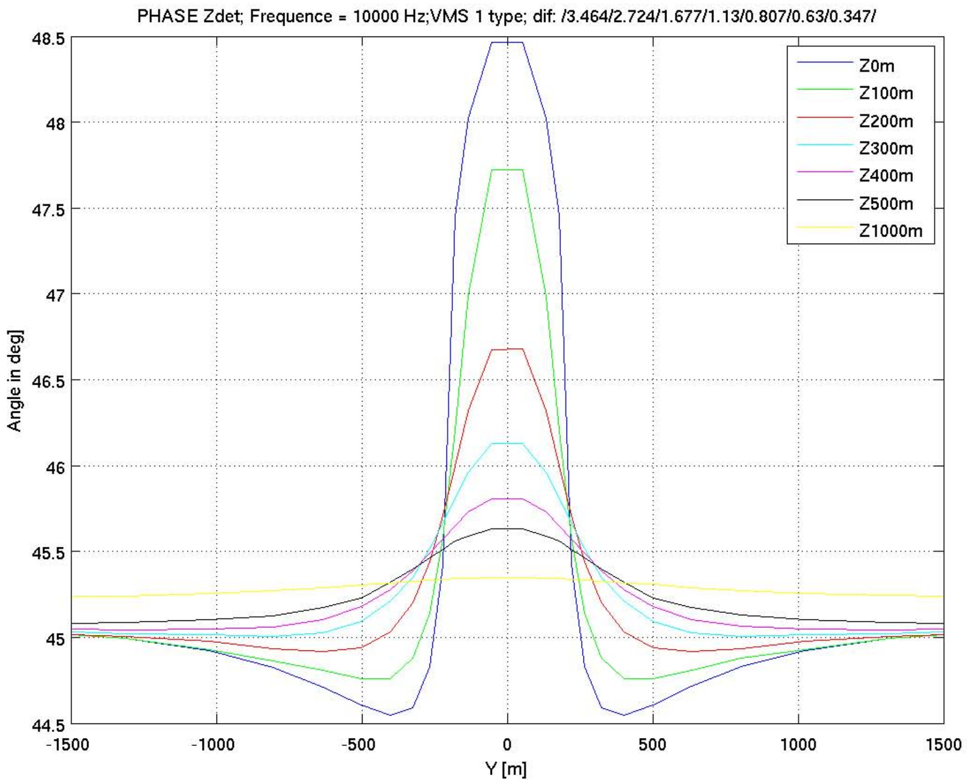

Figure VMS1-17: φ_{det} profile along Y-axis (x = 0) at F = 10,000 Hz for various depths.

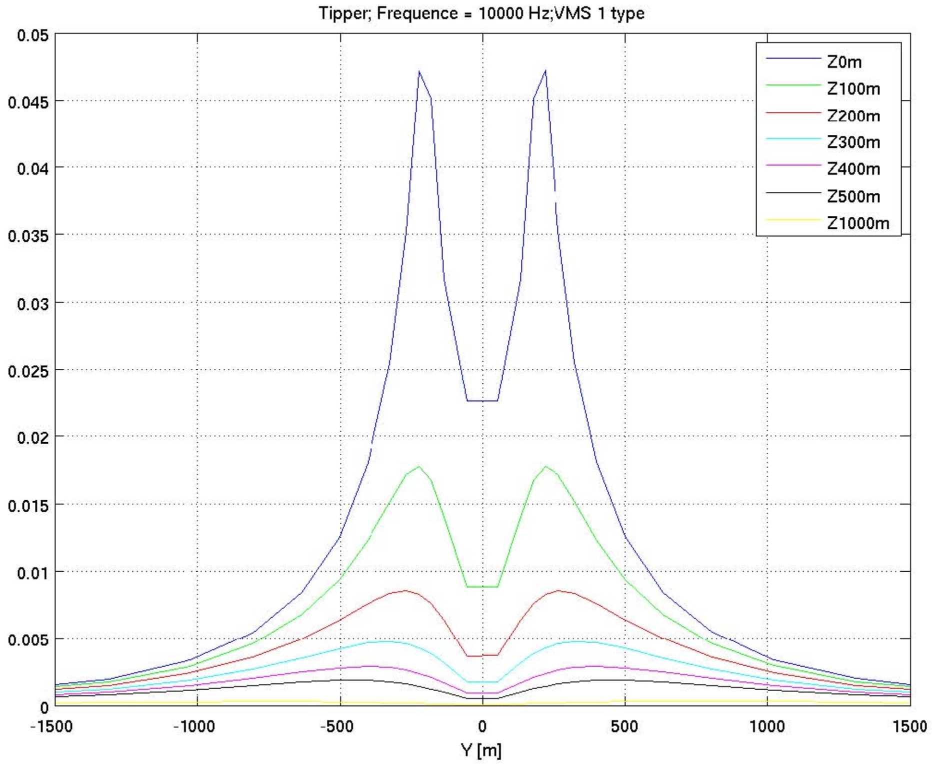

Figure VMS1-18: tipper profile along Y-axis (x = 0) at F = 10,000 Hz for various depths.

VMS2

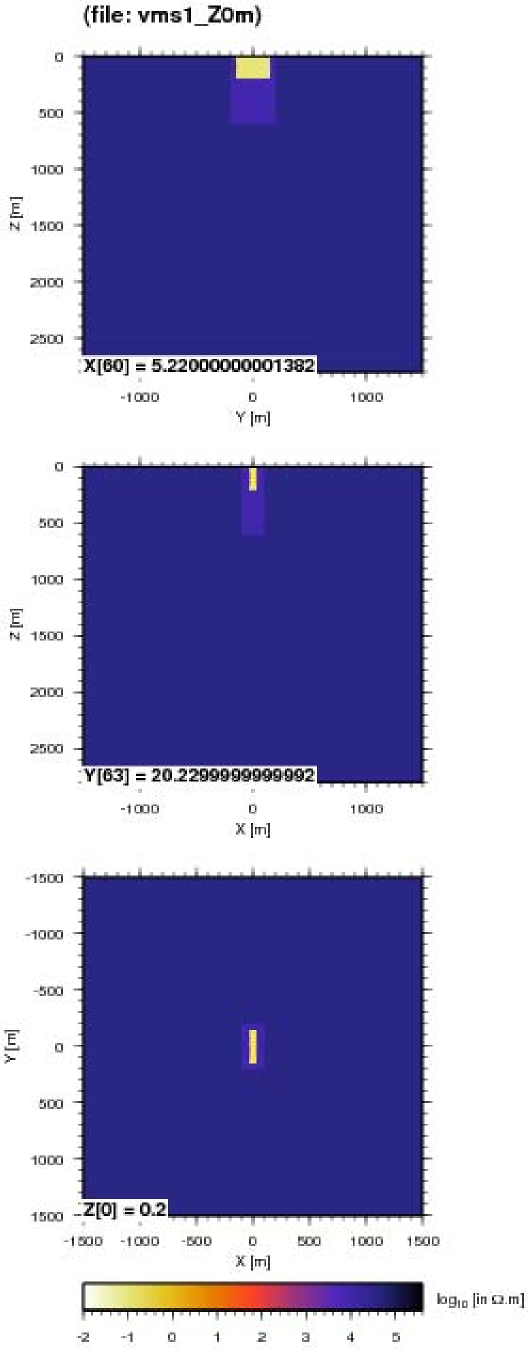

Figure VMS2-1: model of a conductive 0.1 Ω.m orebody (Matagami-type) included within an alteration zone of 10,000 Ω.m in a resistive host rock (40,000 Ω.m). Dimensions are 200 m x 30 m x 300 m for the orebody and 400 m x 200m x 600 m for the alteration zone. The mineralization is outcropping (z = 0).

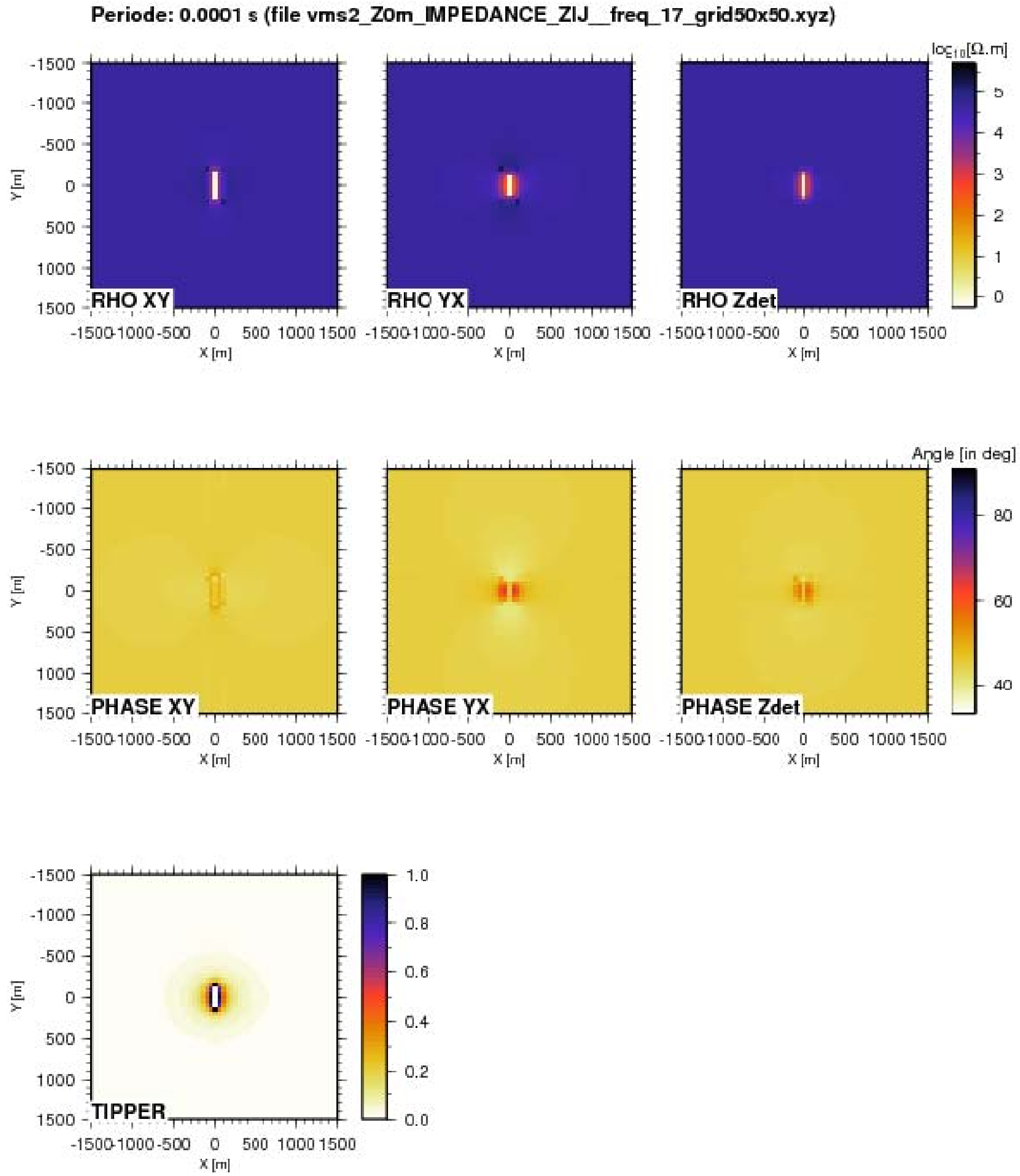

Figure VMS2-2: apparent resistivities and phases, and tipper at T = 10^{-4} s (F = 10,000 Hz). Apparent resistivities and phases are shown for the xy, yx and determinant impedances. Depth z = 0 m.

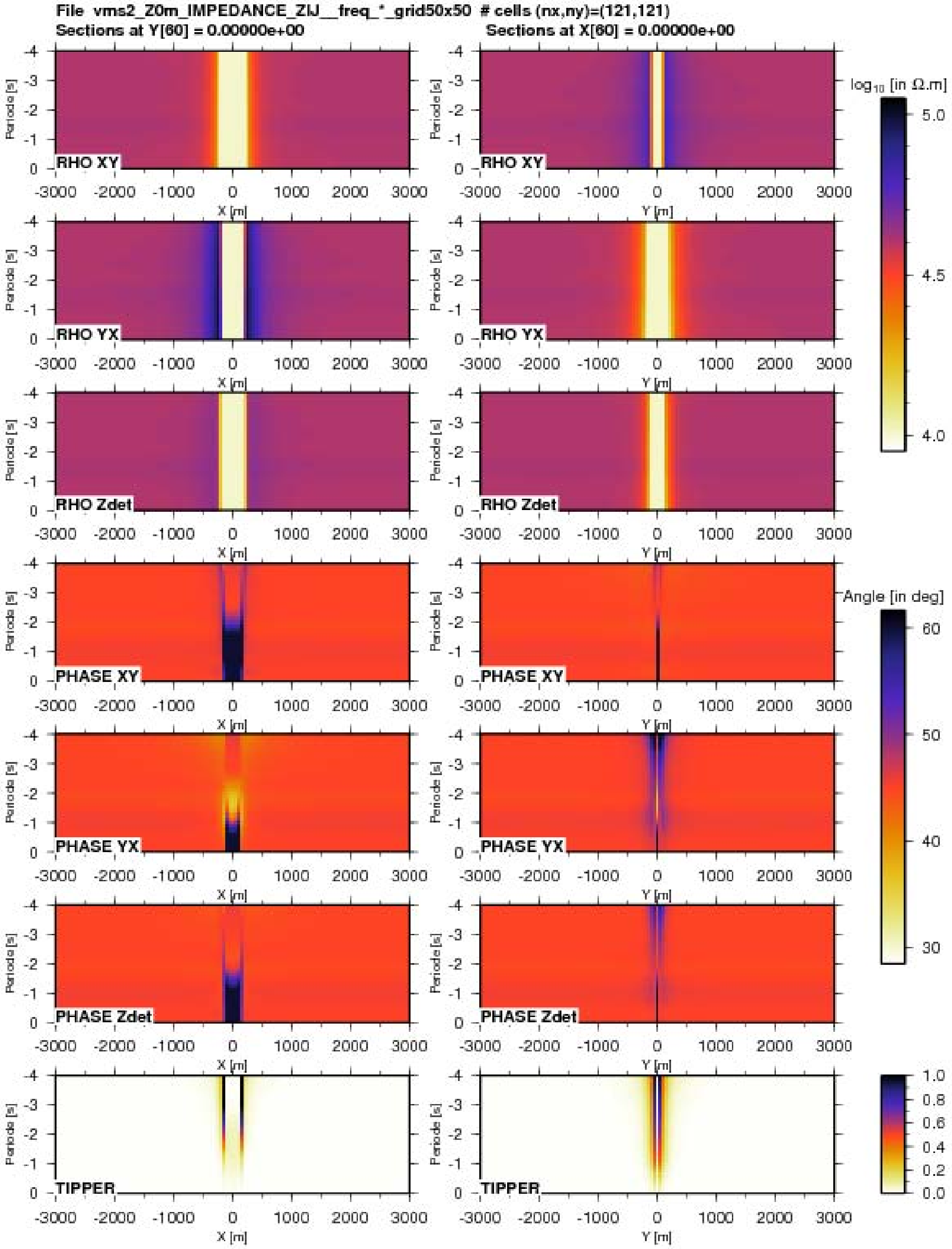

Figure VMS2-3: pseudo-sections of apparent resistivities and phases, and tippers for two orthogonal profiles through the center of the outcropping conductive structure (z = 0 m).

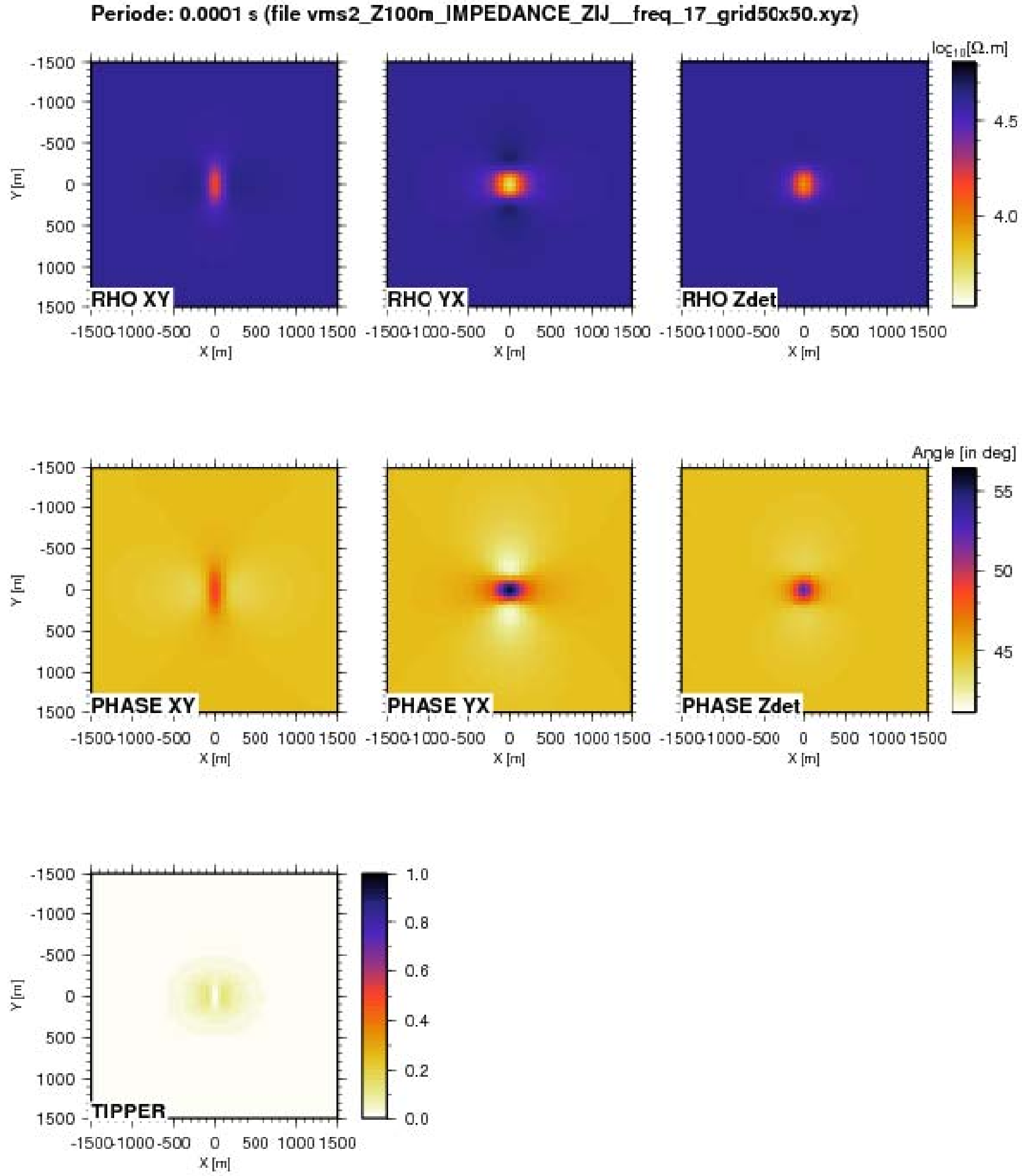

Figure VMS2-4: apparent resistivities and phases, and tipper at T = 10^{-4} s (F = 10,000 Hz). Apparent resistivities and phases are shown for the xy, yx and determinant impedances. Depth z =100 m.

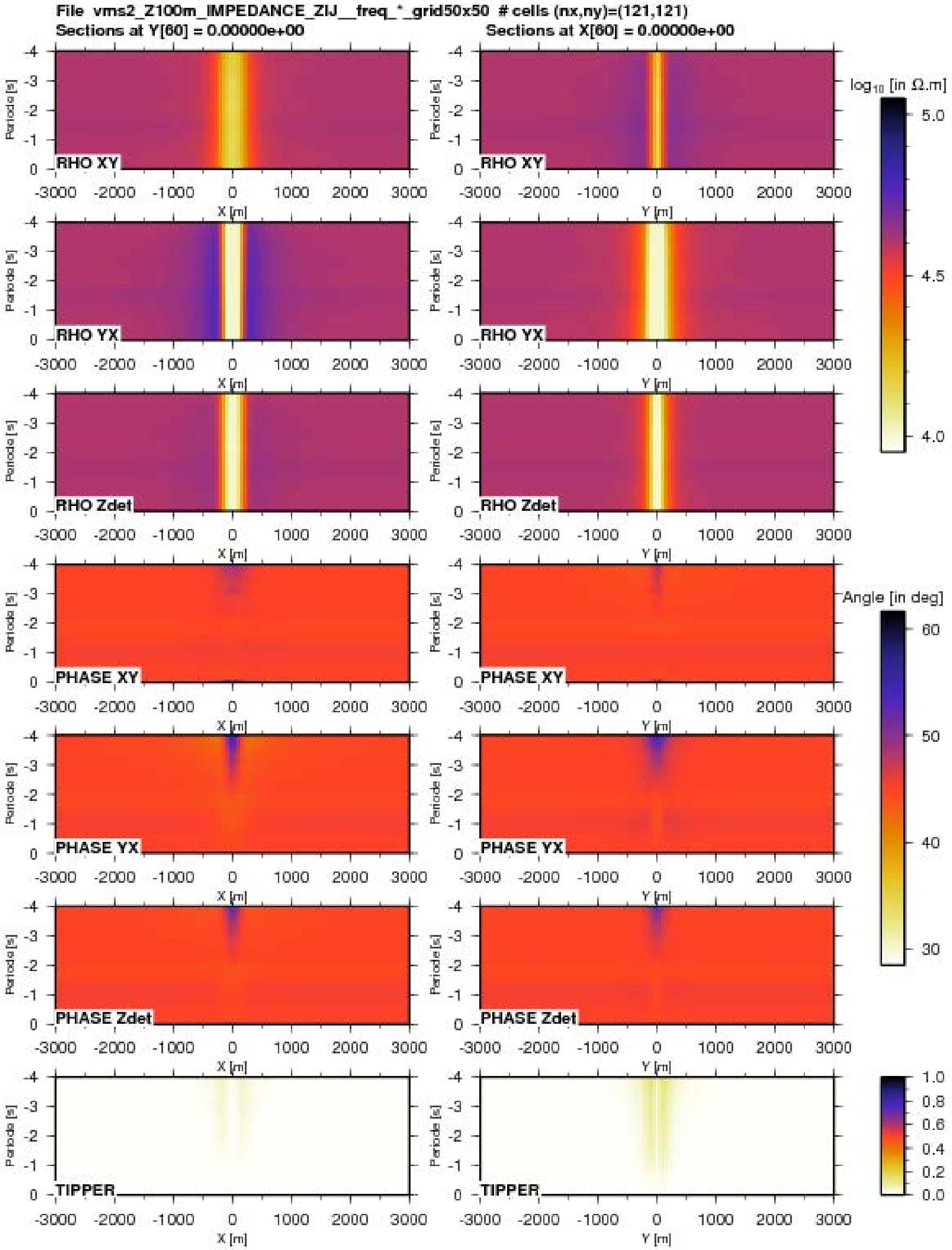

Figure VMS2-5: pseudo-sections of apparent resistivities and phases, and tippers for two orthogonal profiles through the center of the conductive structure (z = 100 m).

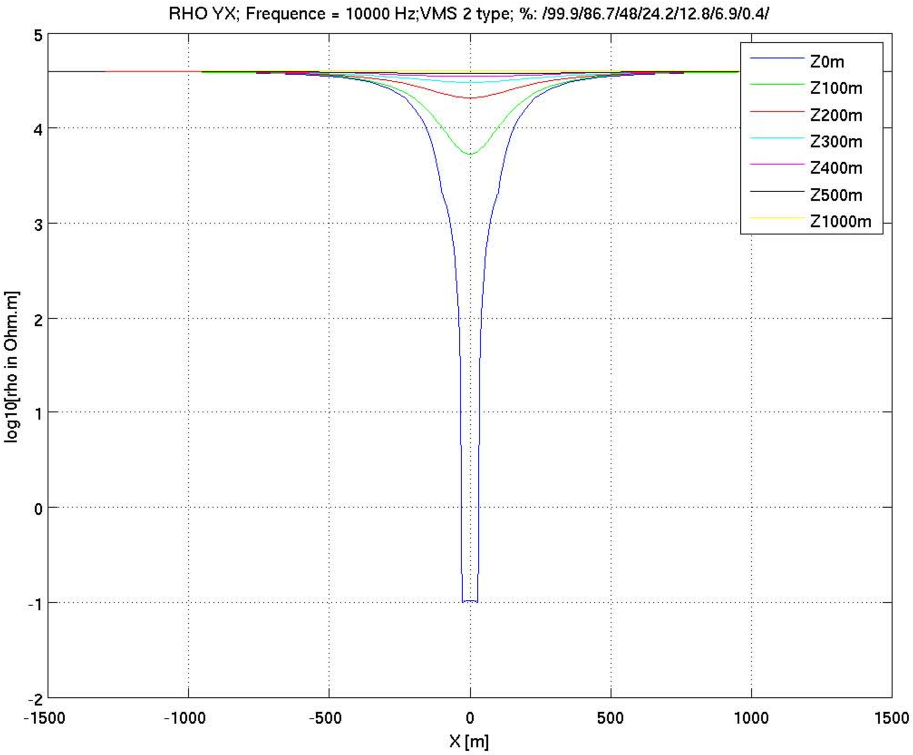

Figure VMS2-6: ρ_{yx} profile along X-axis (y = 0) at F = 10,000 Hz for various depths.

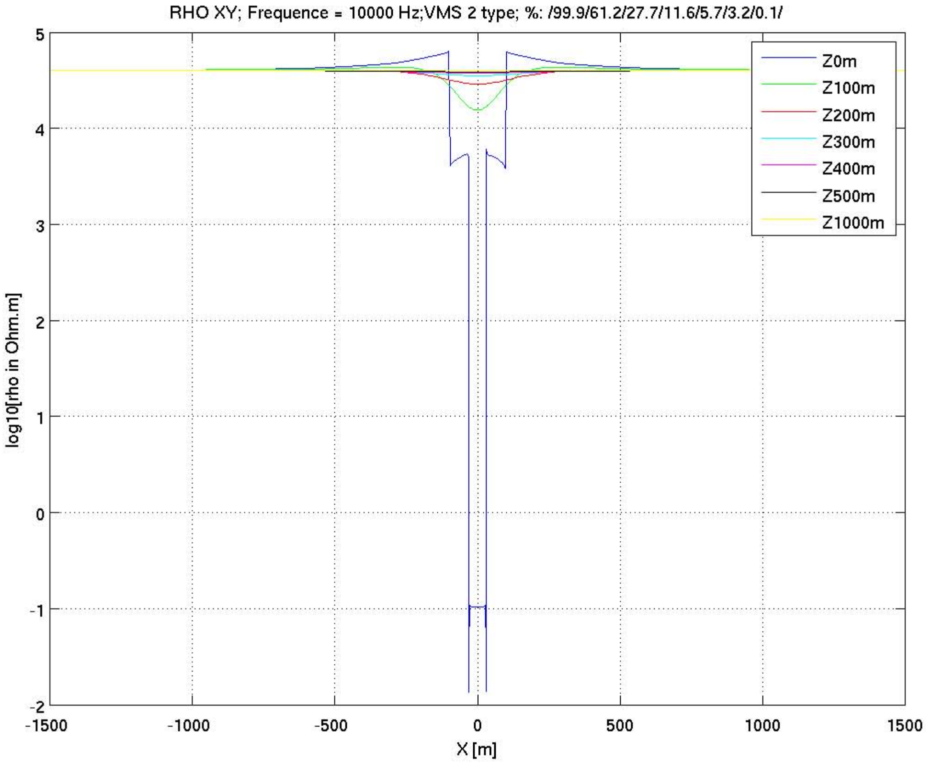

Figure VMS2-7: ρ_{xy} profile along X-axis (y = 0) at F = 10,000 Hz for various depths.

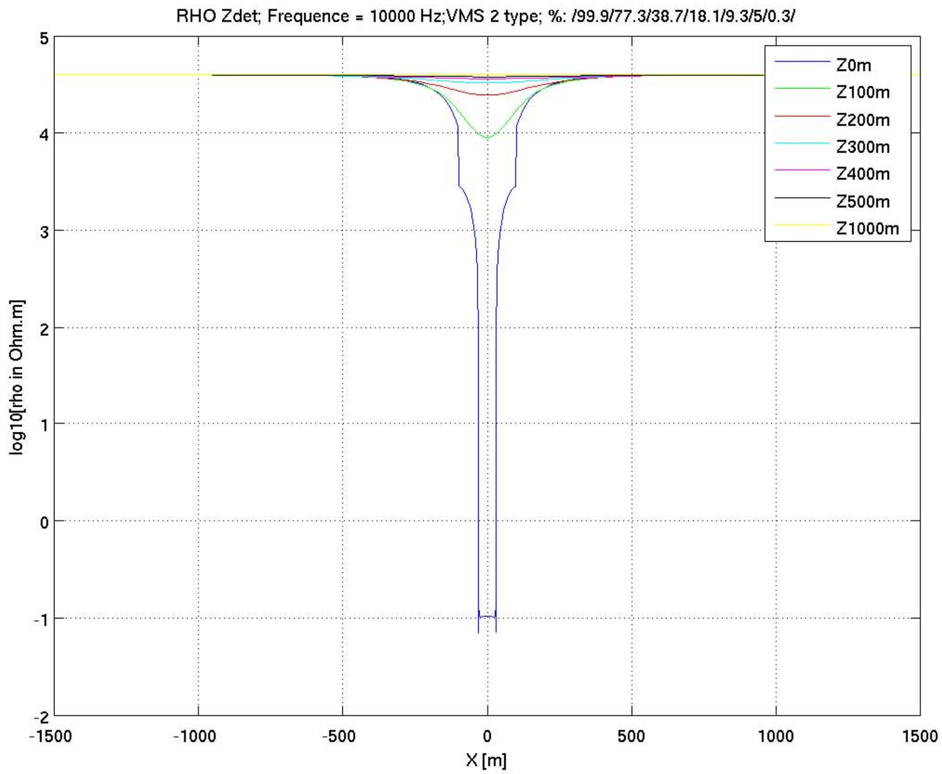

Figure VMS2-8: ρ_{det} profile along X-axis (y = 0) at F = 10,000 Hz for various depths.

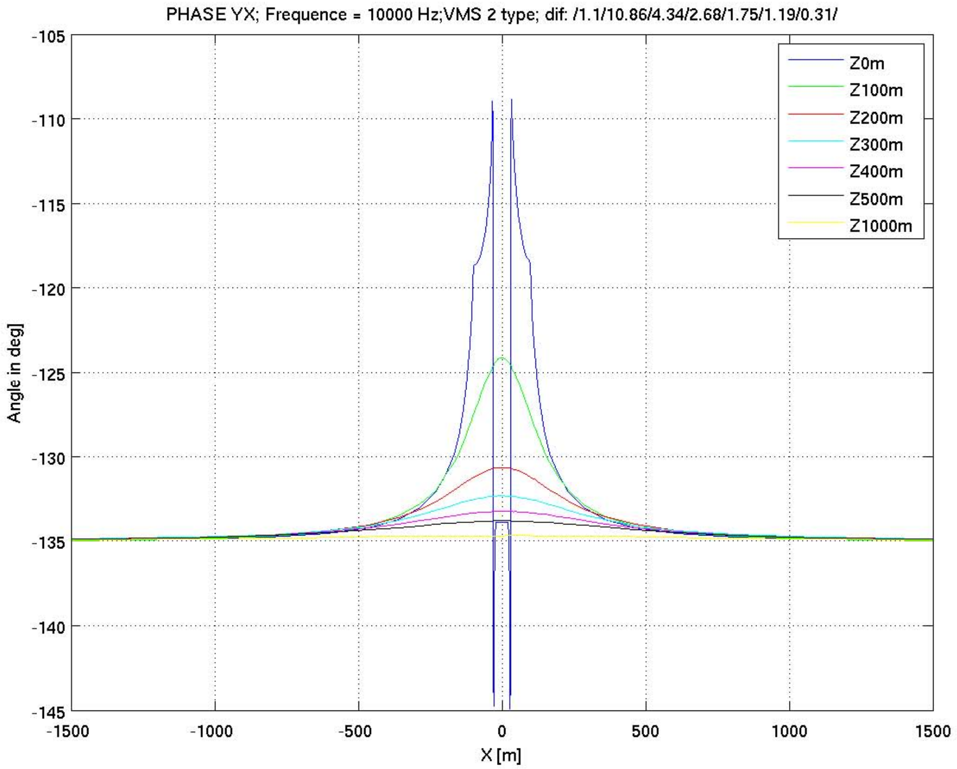

Figure VMS2-9: φ_{yx} profile along X-axis (y = 0) at F = 10,000 Hz for various depths.

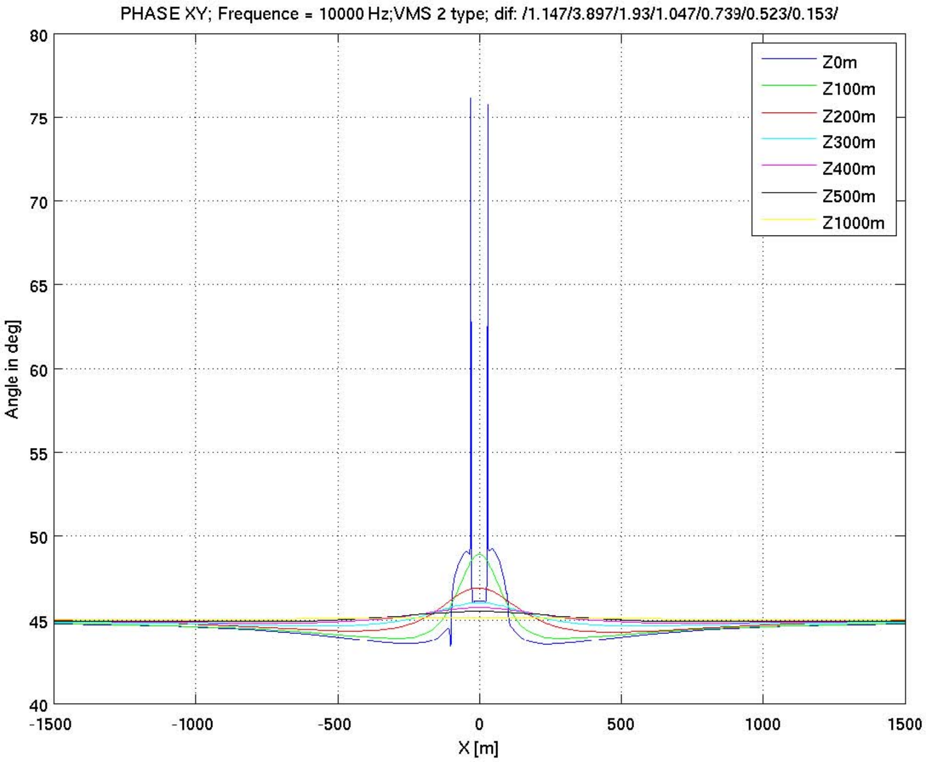

Figure VMS2-10: φ_{xy} profile along X-axis (y = 0) at F = 10,000 Hz for various depths.

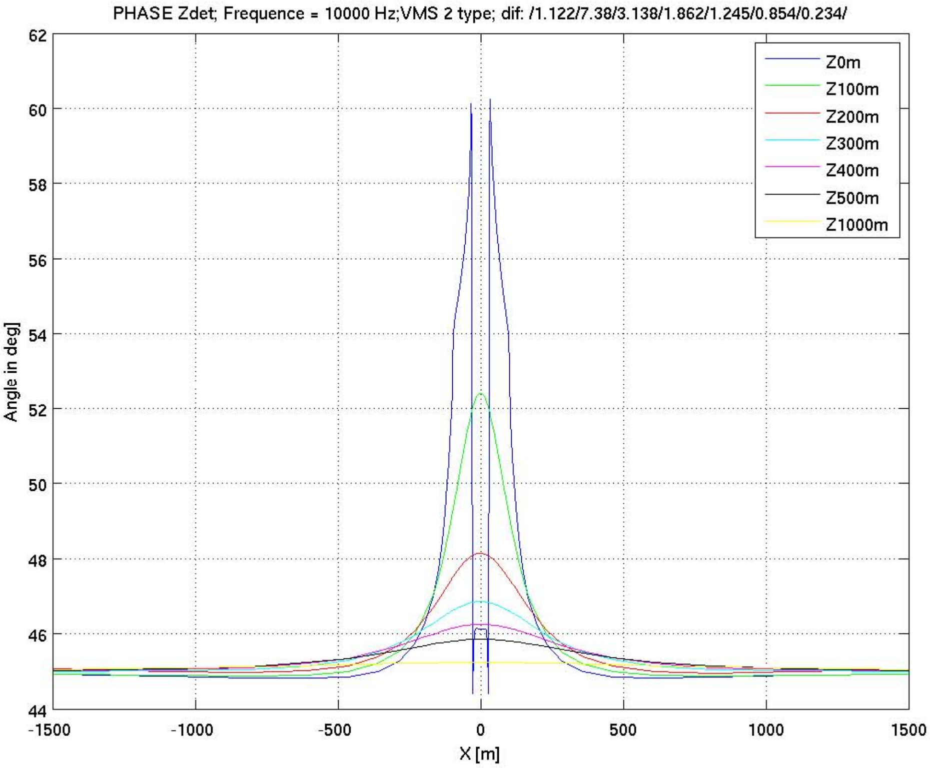

Figure VMS2-11: φ_{det} profile along X-axis (y = 0) at F = 10,000 Hz for various depths.

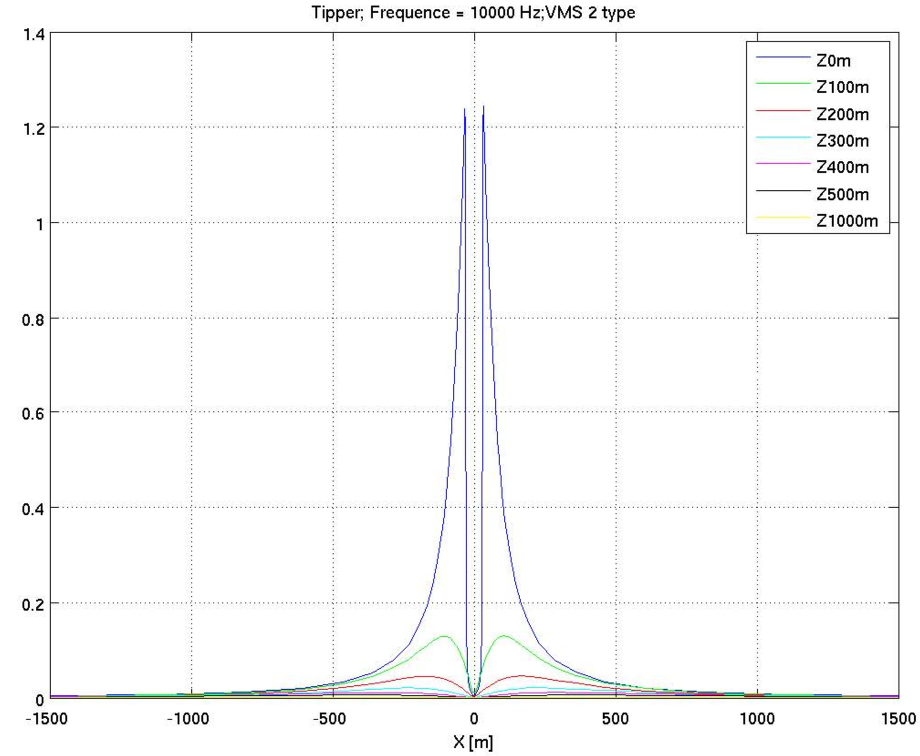

Figure VMS2-12: tipper profile along X-axis (y = 0) at F = 10,000 Hz for various depths.

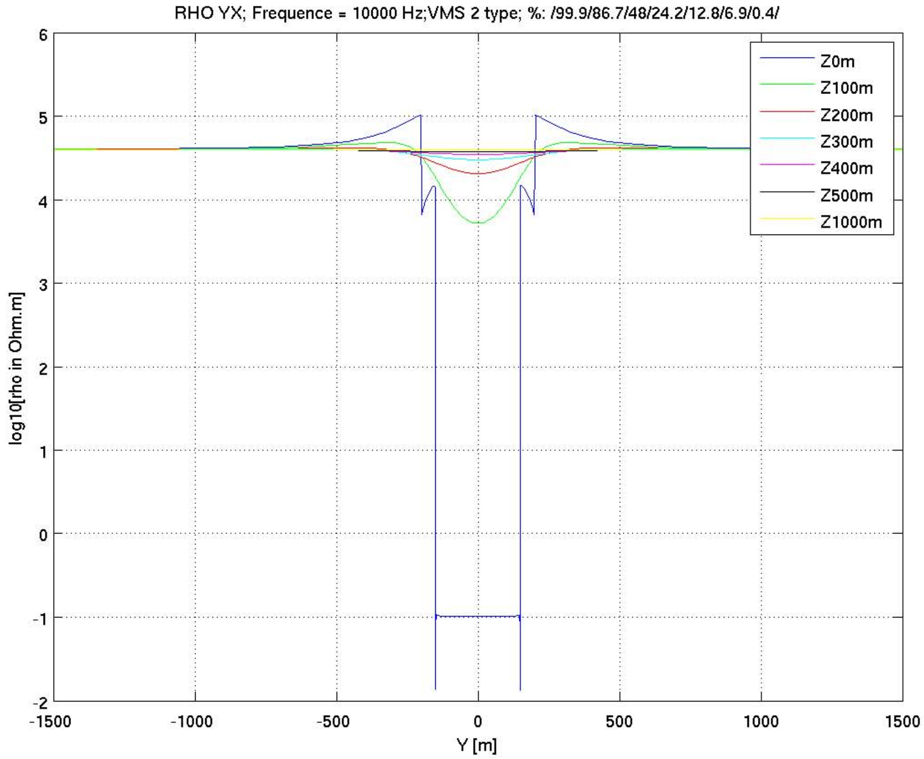

Figure VMS2-13: ρ_{yx} profile along Y-axis (x = 0) at F = 10,000 Hz for various depths.

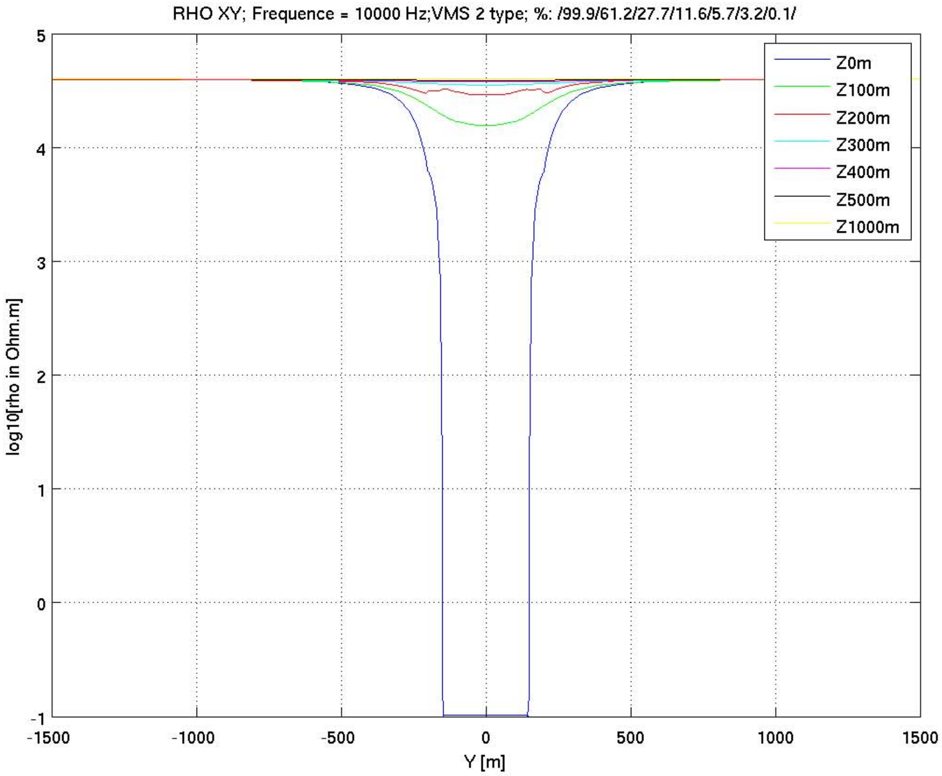

Figure VMS2-14: ρ_{xy} profile along Y-axis (x = 0) at F = 10,000 Hz for various depths.

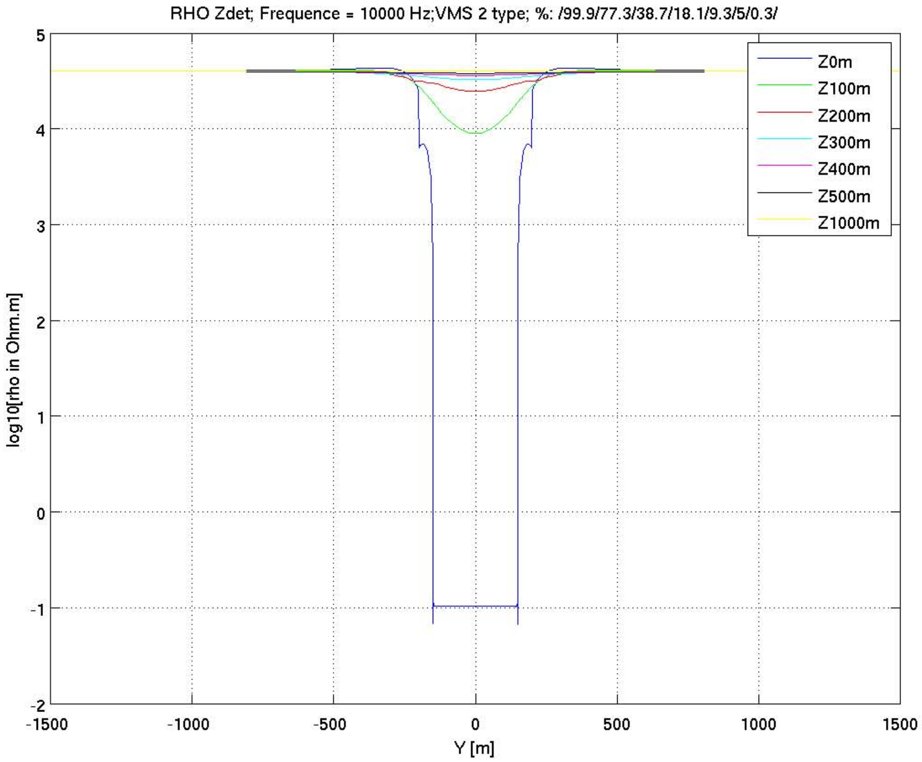

Figure VMS2-15: ρ_{det} profile along Y-axis (x = 0) at F = 10,000 Hz for various depths.

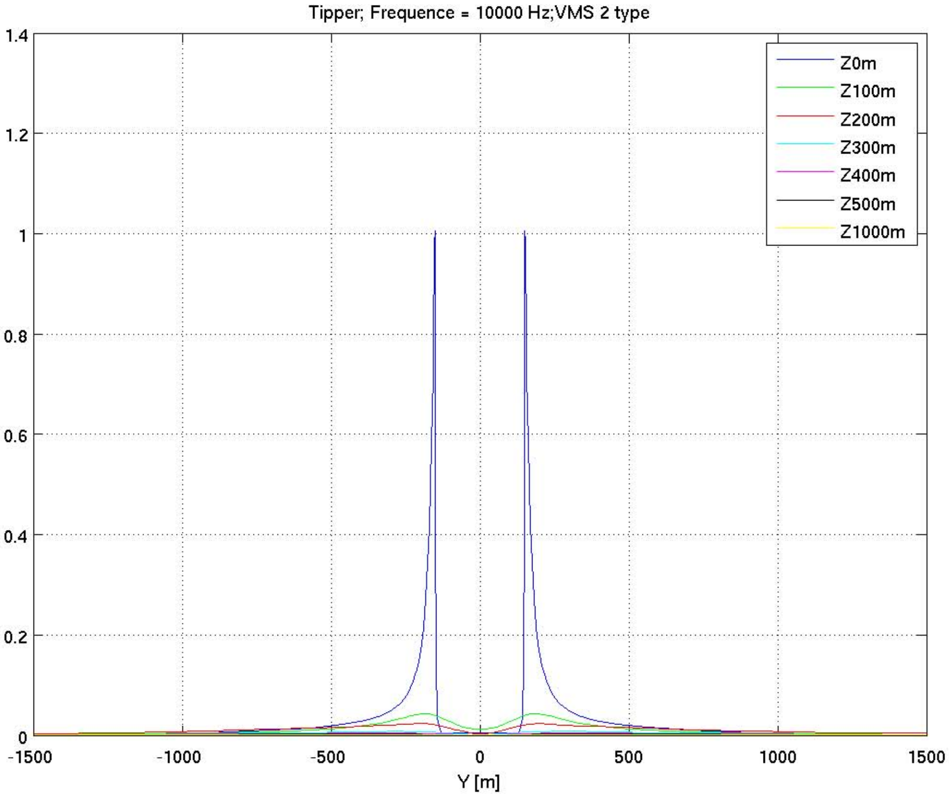

Figure VMS2-16: tipper profile along Y-axis (x = 0) at F = 10,000 Hz for various depths.

RAGLAN NI-TYPE DEPOSIT

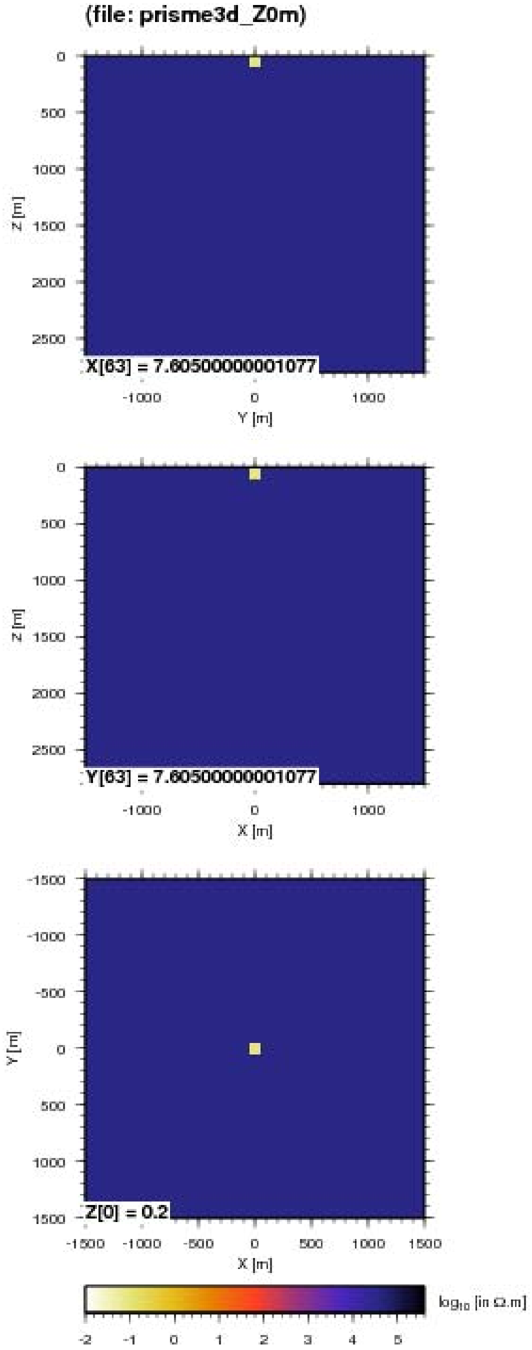

Figure RNI-1: typical Ni model of the Raglan mining camp (100m x 100m x 100m). Resistivities for the orebody and the host rock are 0.1 Ω.m and 40,000 Ω.m respectively.

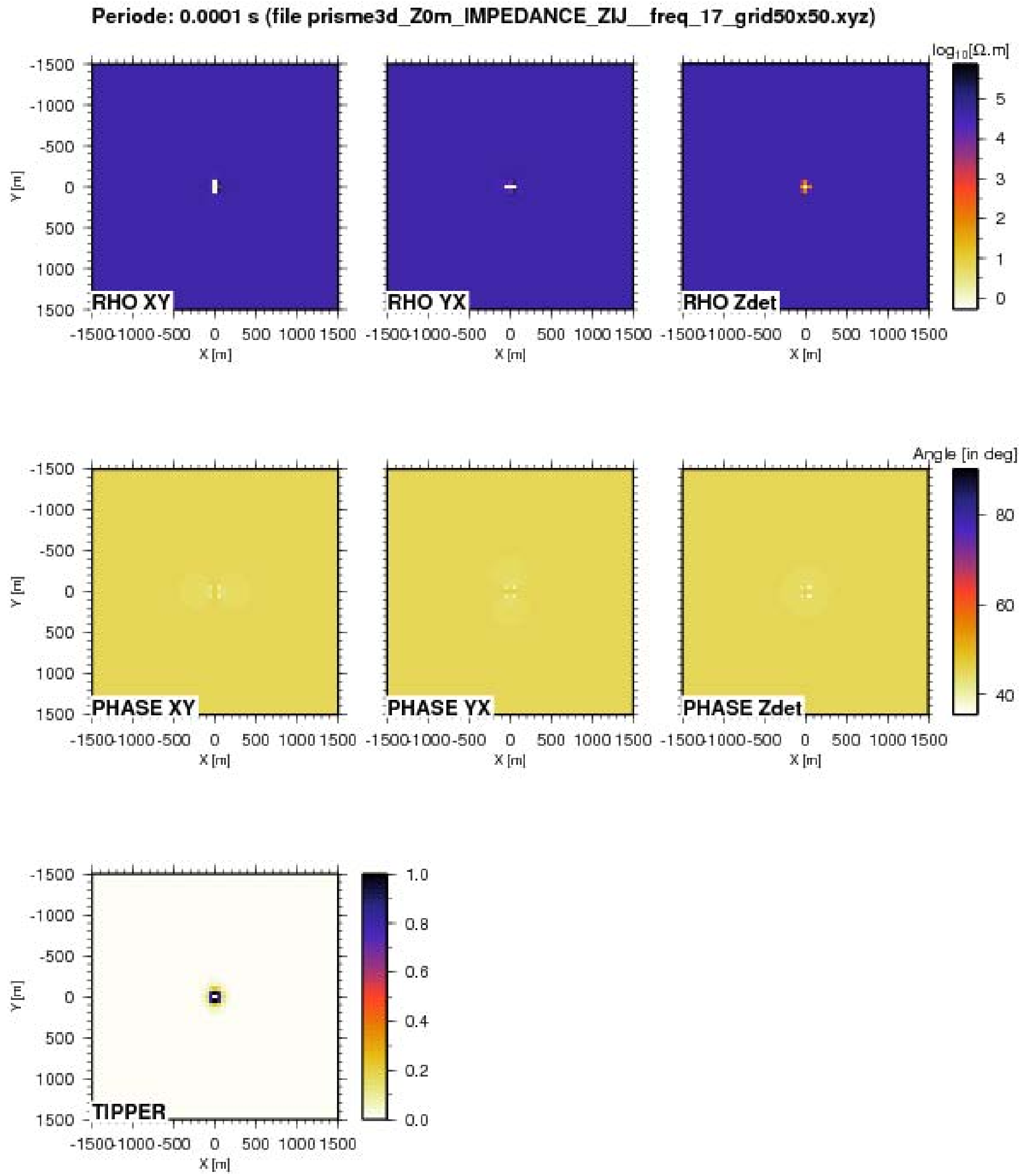

***Figure RNI-2**: apparent resistivities and phases, and tipper at T = 10^{-4} s (F = 10,000 Hz). Apparent resistivities and phases are shown for the xy, yx and determinant impedances.*

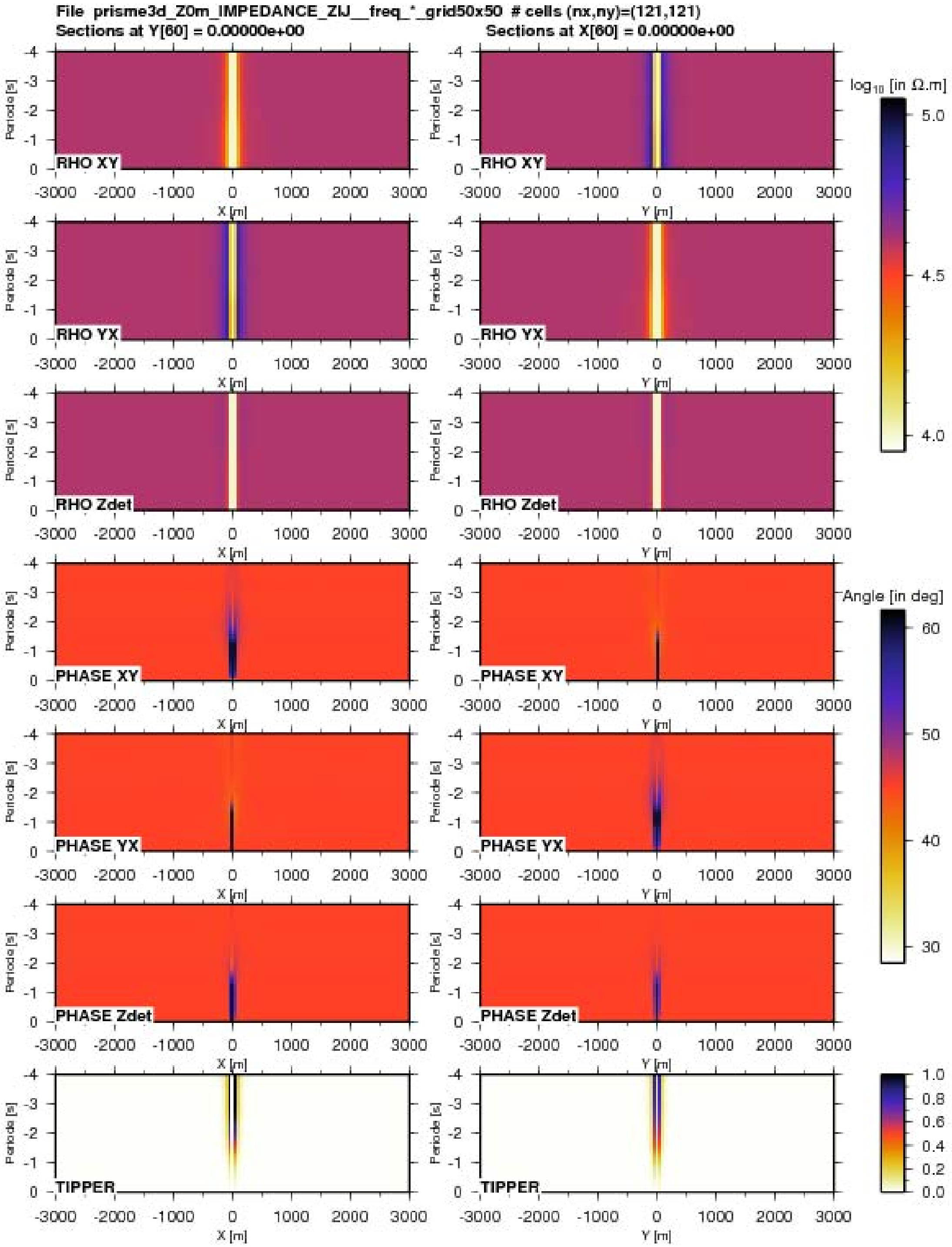

Figure RNI-3: pseudo-sections of apparent resistivities and phases, and tippers for two orthogonal profiles through the center of the outcropping conductive structure (z = 0 m).

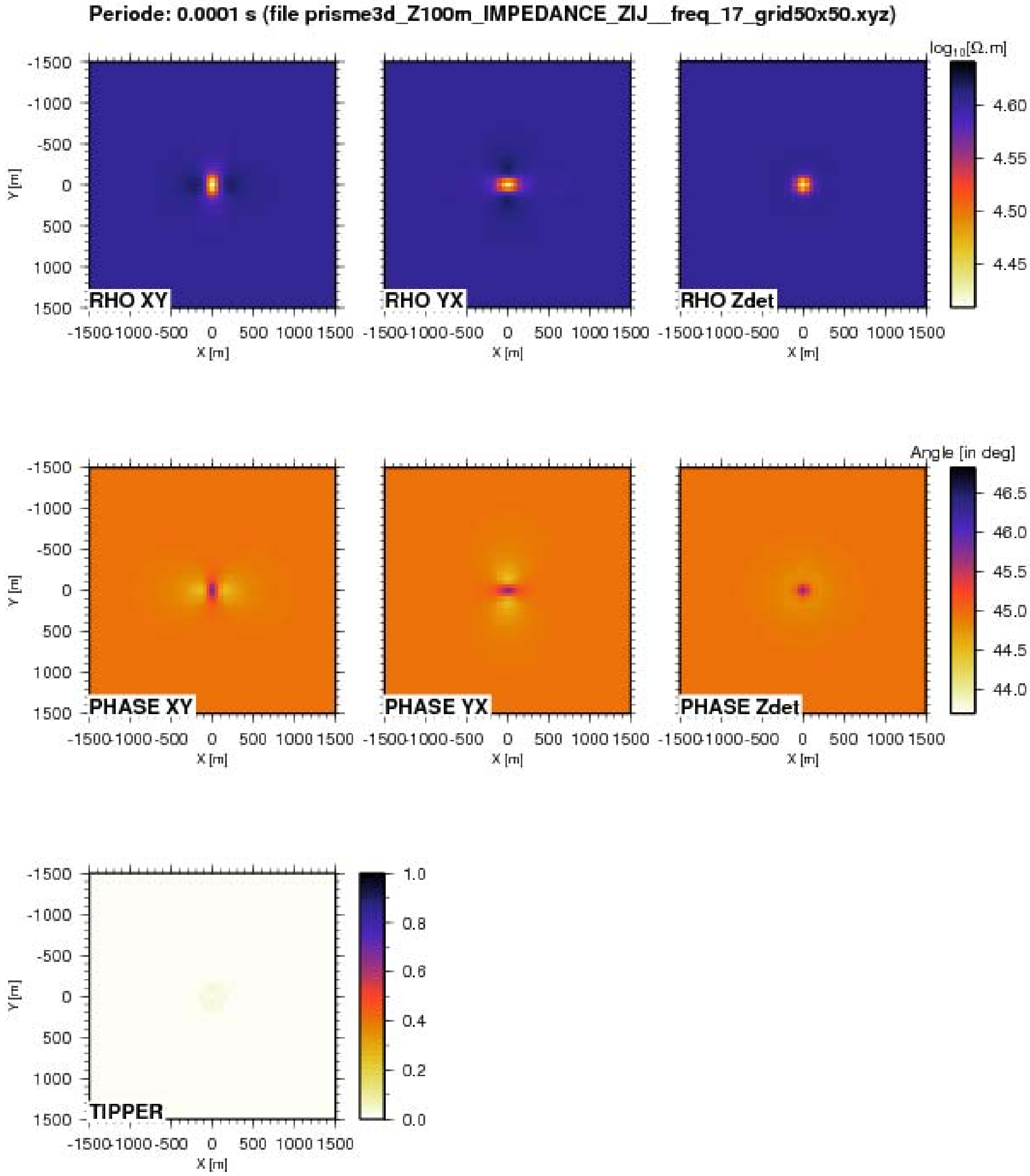

Figure RNI-4: apparent resistivities and phases, and tipper at T = 10^{-4} s (F = 10,000 Hz). Apparent resistivities and phases are shown for the xy, yx and determinant impedances at depth z = 100 m.

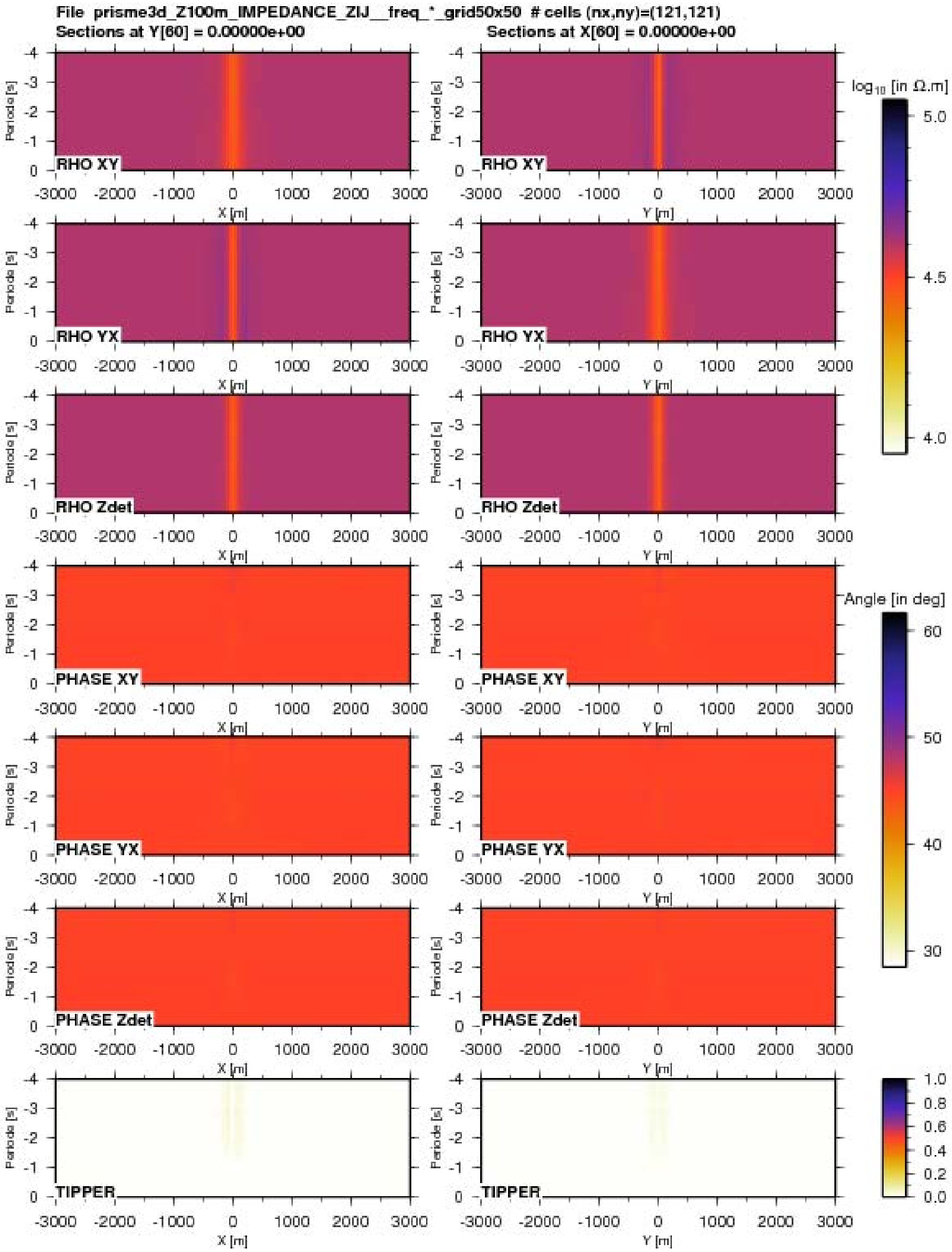

Figure RNI-5: pseudo-sections of apparent resistivities and phases, and tippers for two orthogonal profiles through the center of the conductive structure at z = 100 m.

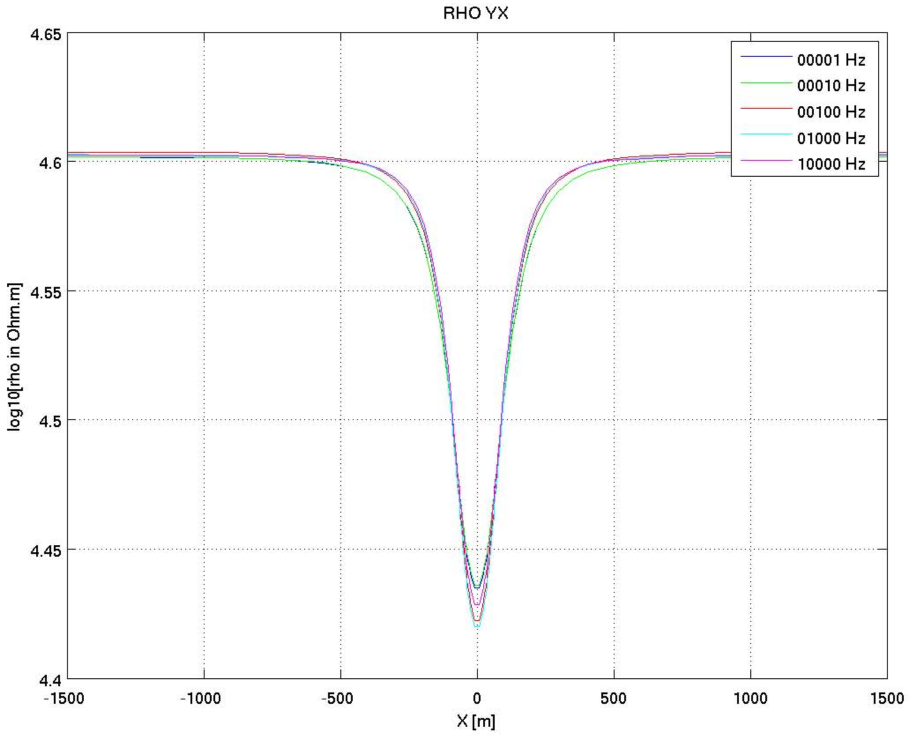

Figure RNI-6: ρ_{yx} profile along X-axis (y = 0) for conductive structure at z = 100 m for F = [1 Hz; 10,000 Hz].

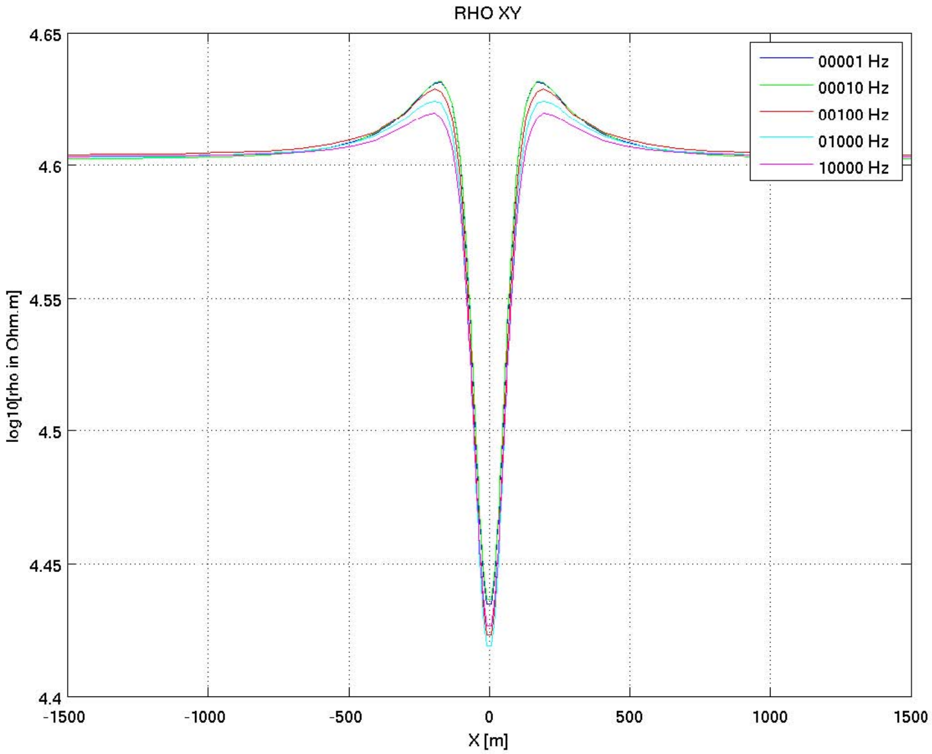

Figure RNI-7: ρ_{xy} profile along X-axis (y = 0) for conductive structure at z = 100 m for F = [1 Hz;

10,000 Hz].

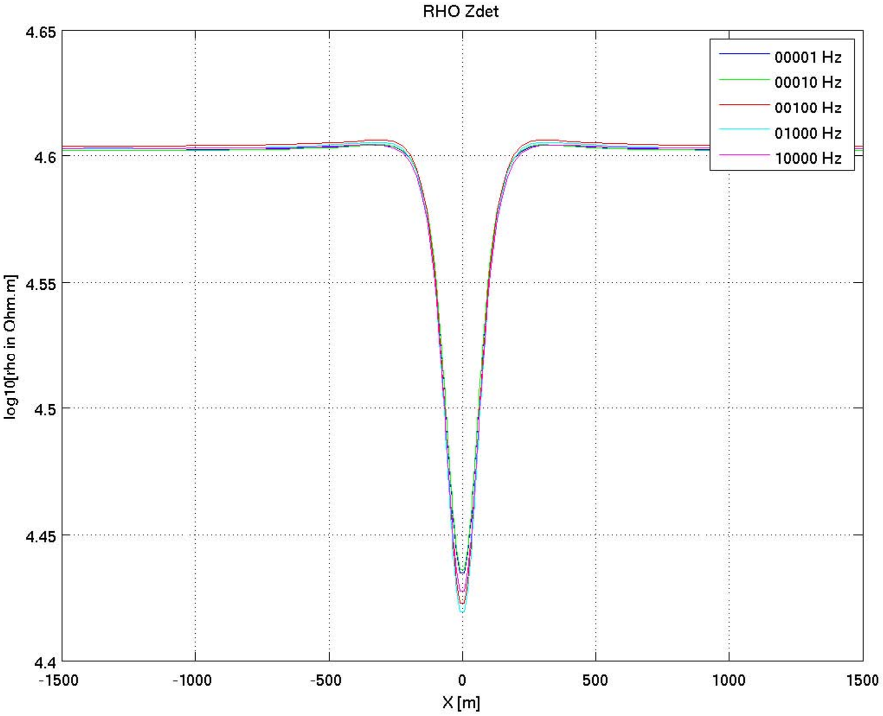

Figure RNI-8: ρ_{det} profile along X-axis (y = 0) for conductive structure at z = 100 m for F = [1 Hz; 10,000 Hz].

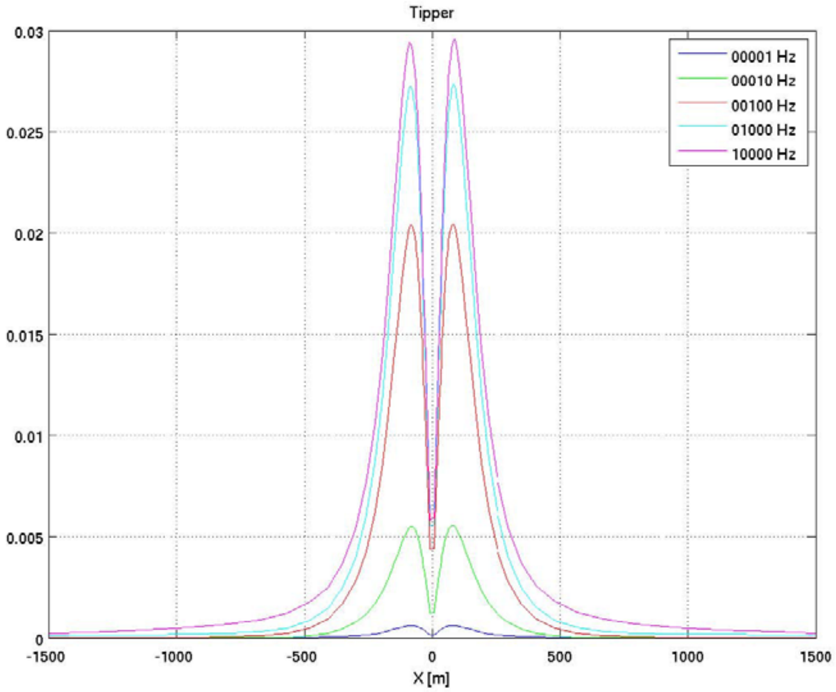

Figure RNI-9: tipper profile along X-axis (y = 0) for conductive structure at z = 100 m for F = [1 Hz; 10,000 Hz].

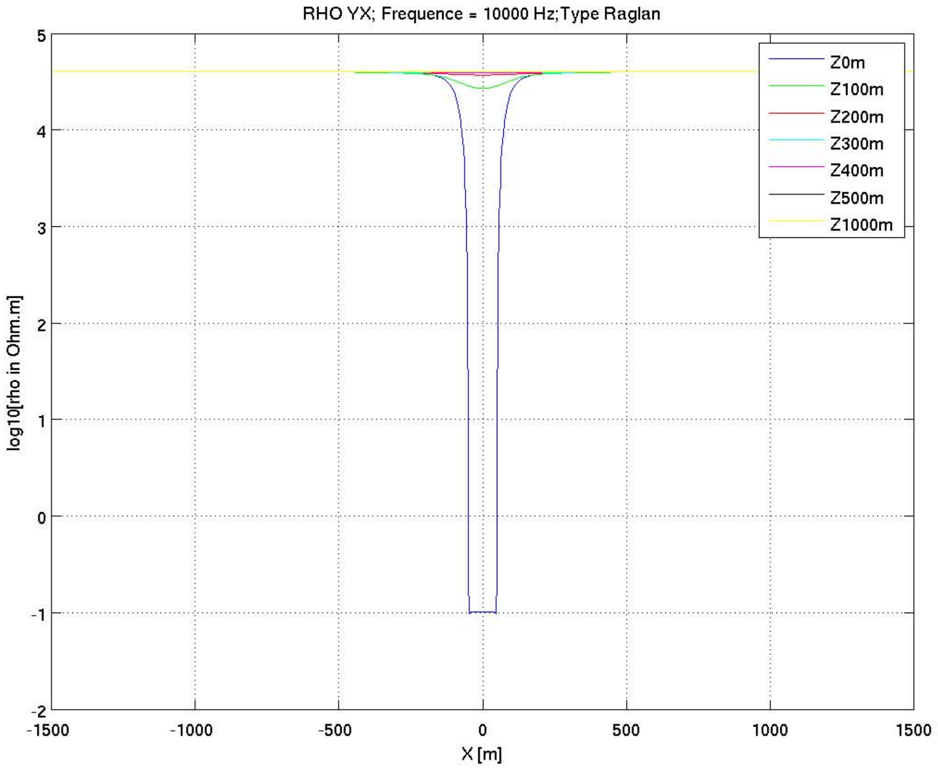

Figure RNI-10: *ρ_{yx} profile along X-axis (y = 0) at F = 10,000 Hz for various depths.*

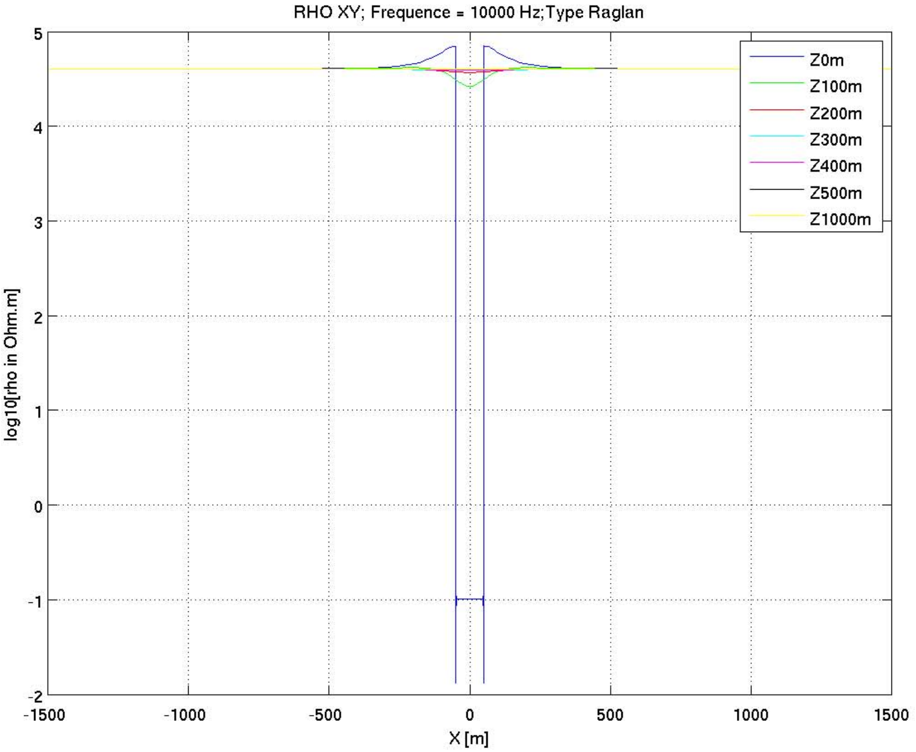

Figure RNI-11: *ρ_{xy} profile along X-axis (y = 0) at F = 10,000 Hz for various depths.*

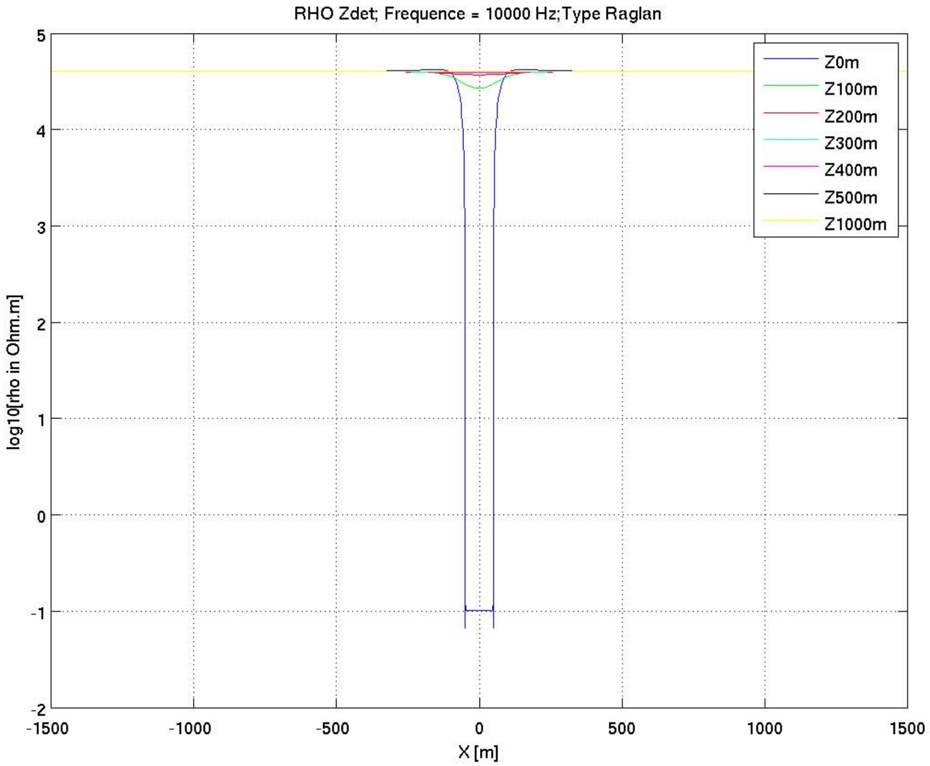

Figure RNI-12: ρ_{det} profile along X-axis (y = 0) at F = 10,000 Hz for various depths.

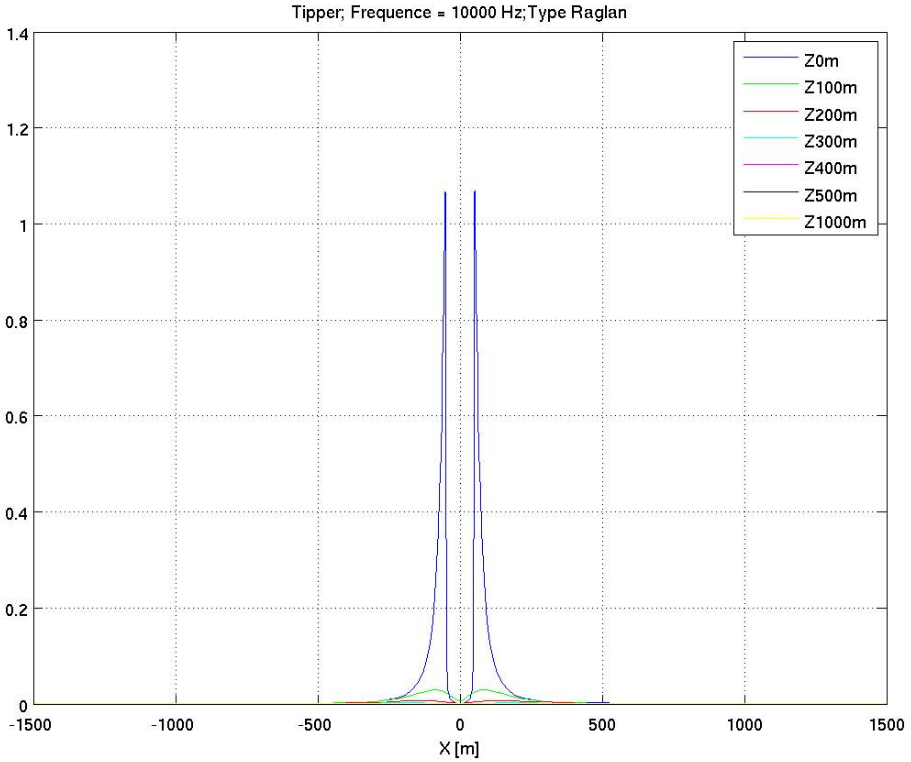

Figure RNI-13: tipper along X-axis (y = 0) at F = 10,000 Hz for various depths.

RAGLAN

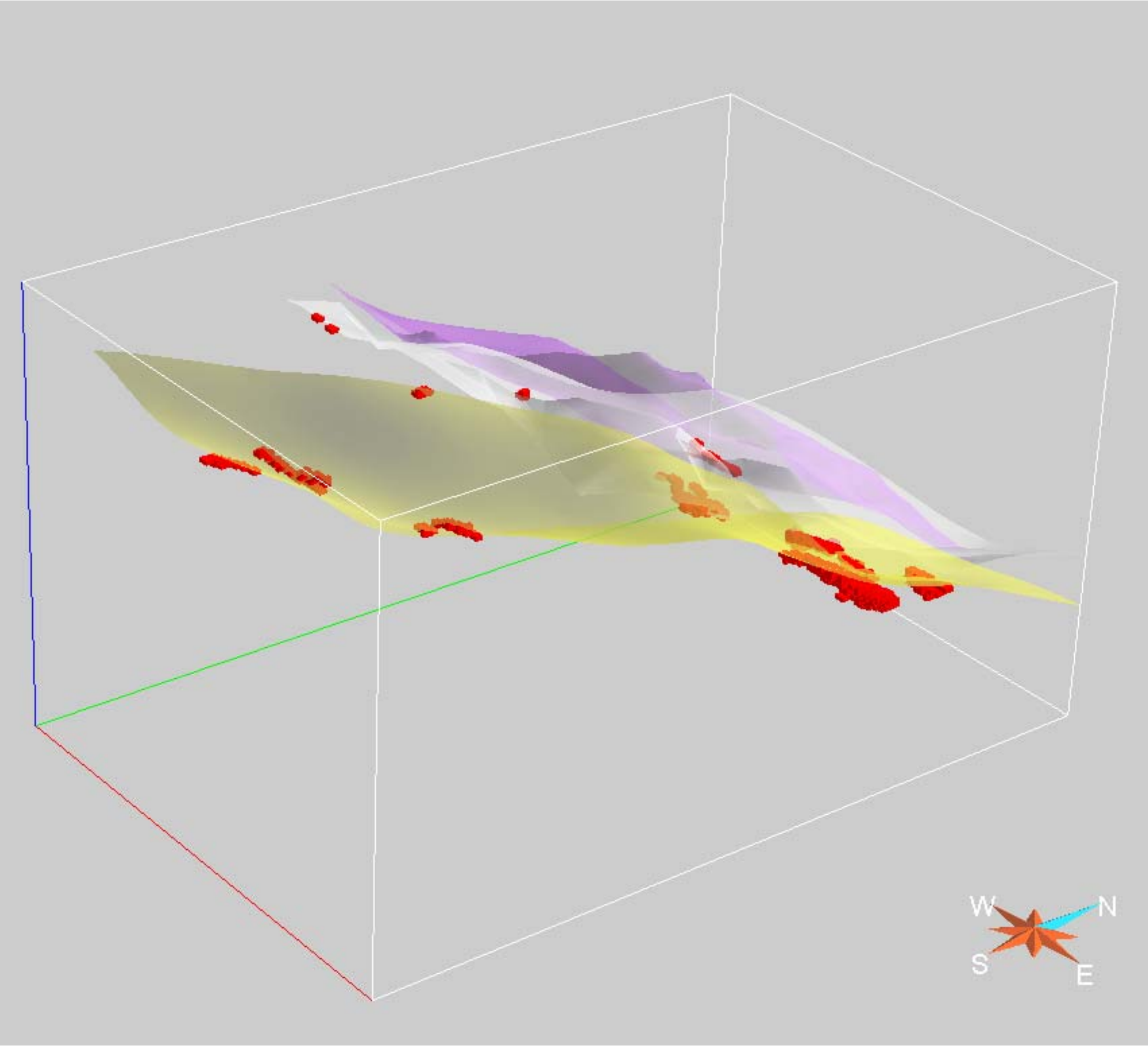

Figure RAG-1: a gOcad geological model of the Raglan mining camp showing the geological units and the position and geometries of the known nickel orebodies.

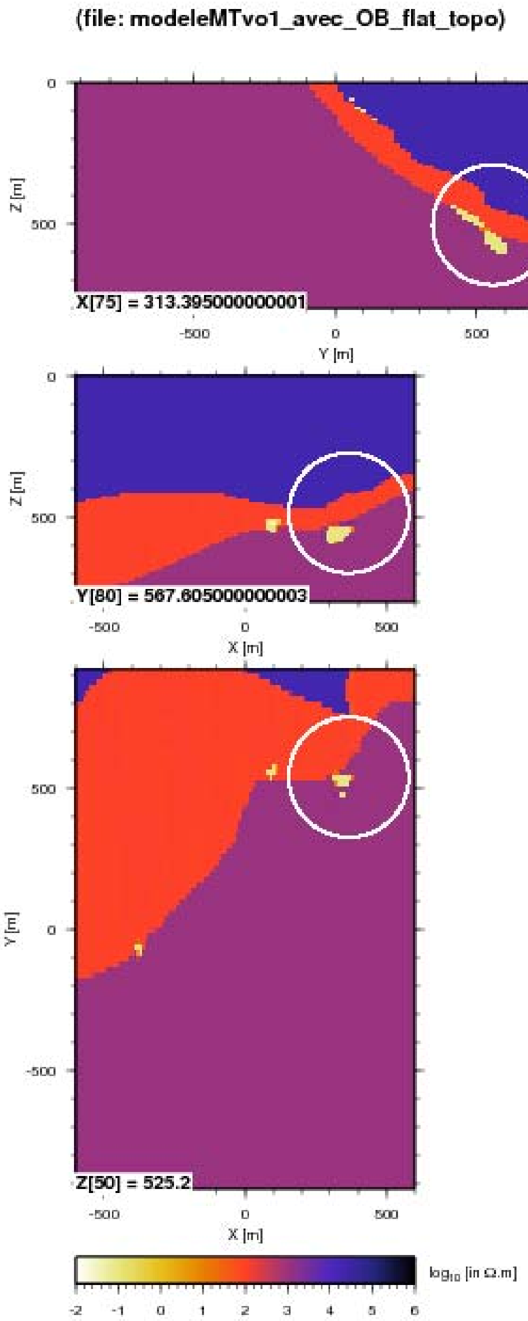

Figure RAG-2: Original model (model 0) of Raglan. Three slices of the Raglan mining camp resistivity model: (top) a NS cross-section running perpendicular to the main regional strike at X = 313.39; (middle) an EW cross-section at y = 567.6; (bottom) an horizontal slice at a depth of z = 525.2 m. Gabbro is displayed in purple (1,000 Ω.m), ultramafics in red (100 Ω.m), mafics in blue (20,000 Ω.m) and Ni-mineralization in yellow (0.1 Ω.m). Orebody 8H is circled in white.

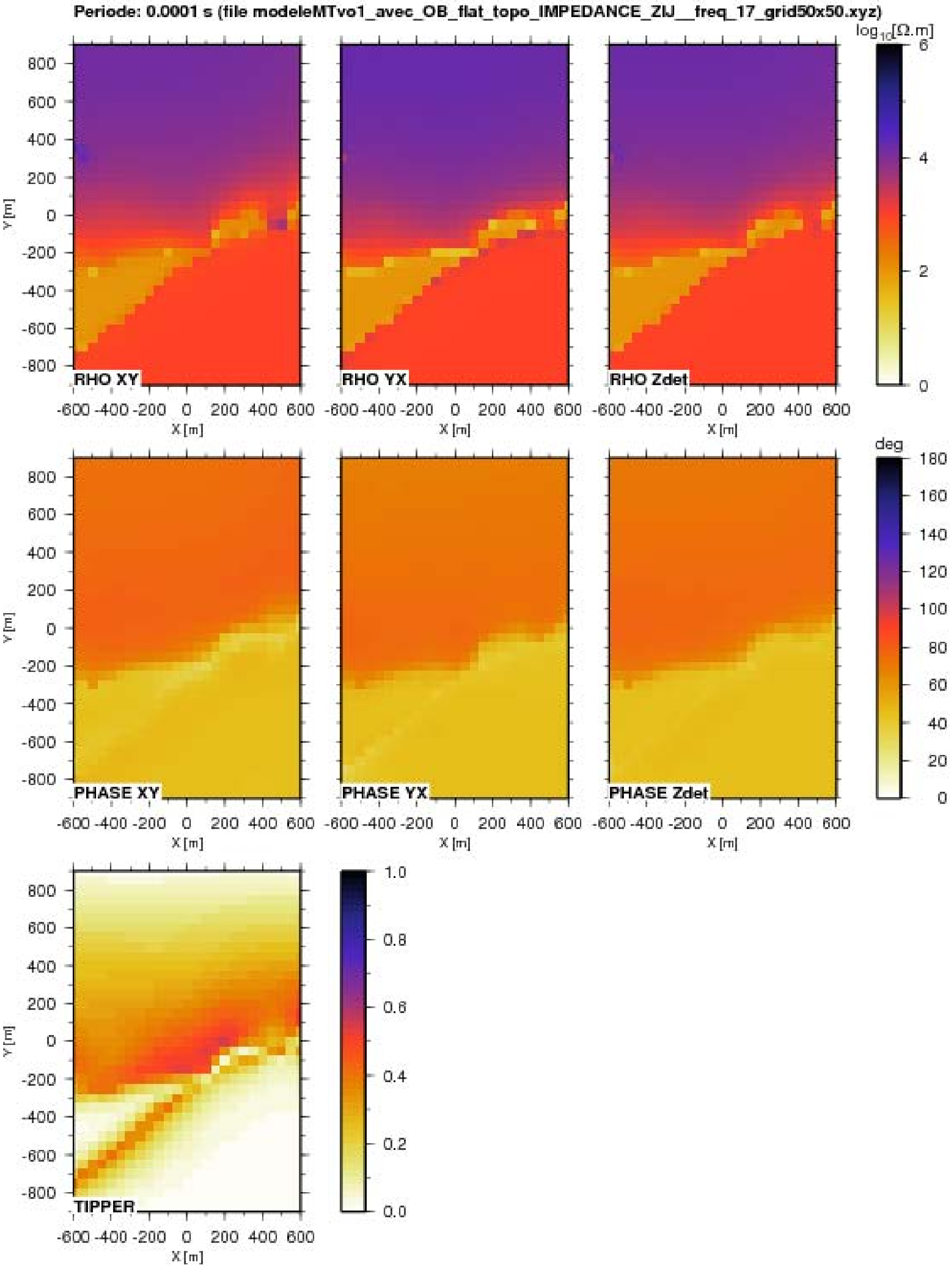

Figure RAG-3: maps showing apparent resistivities and phases (xy, yx and det) and tipper for F = 10^4 Hz. Apparent resistivities and tipper are sensitive to outcropping geology and delineation of the lithologies is particularly impressive.

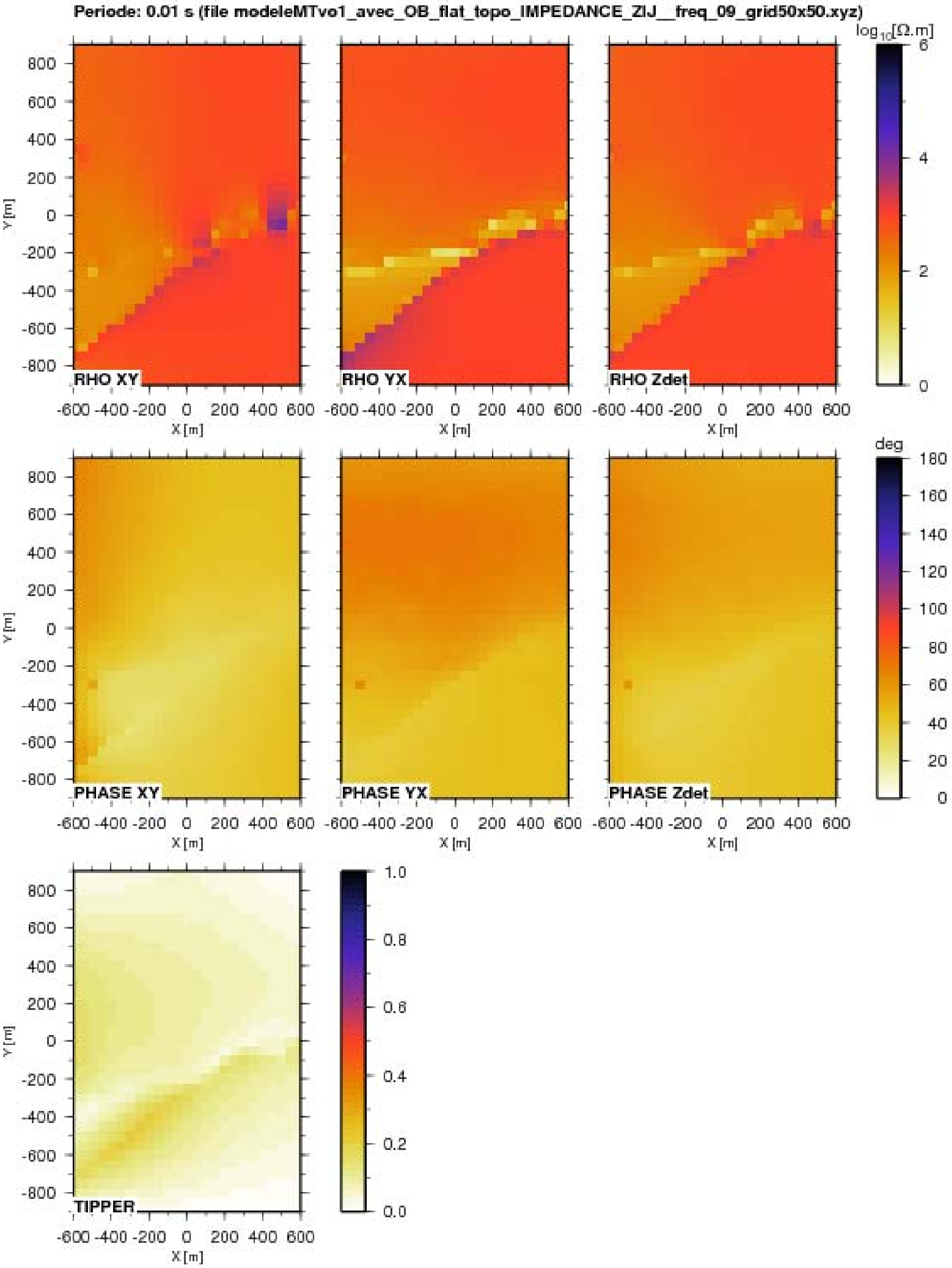

Figure RAG-4: maps showing apparent resistivities and phases (xy, yx and det) and tipper for F = 10^2 Hz. Apparent resistivities and tipper are sensitive to the geology but delineation of the lithologies is poorer than at F = 10^4 Hz.

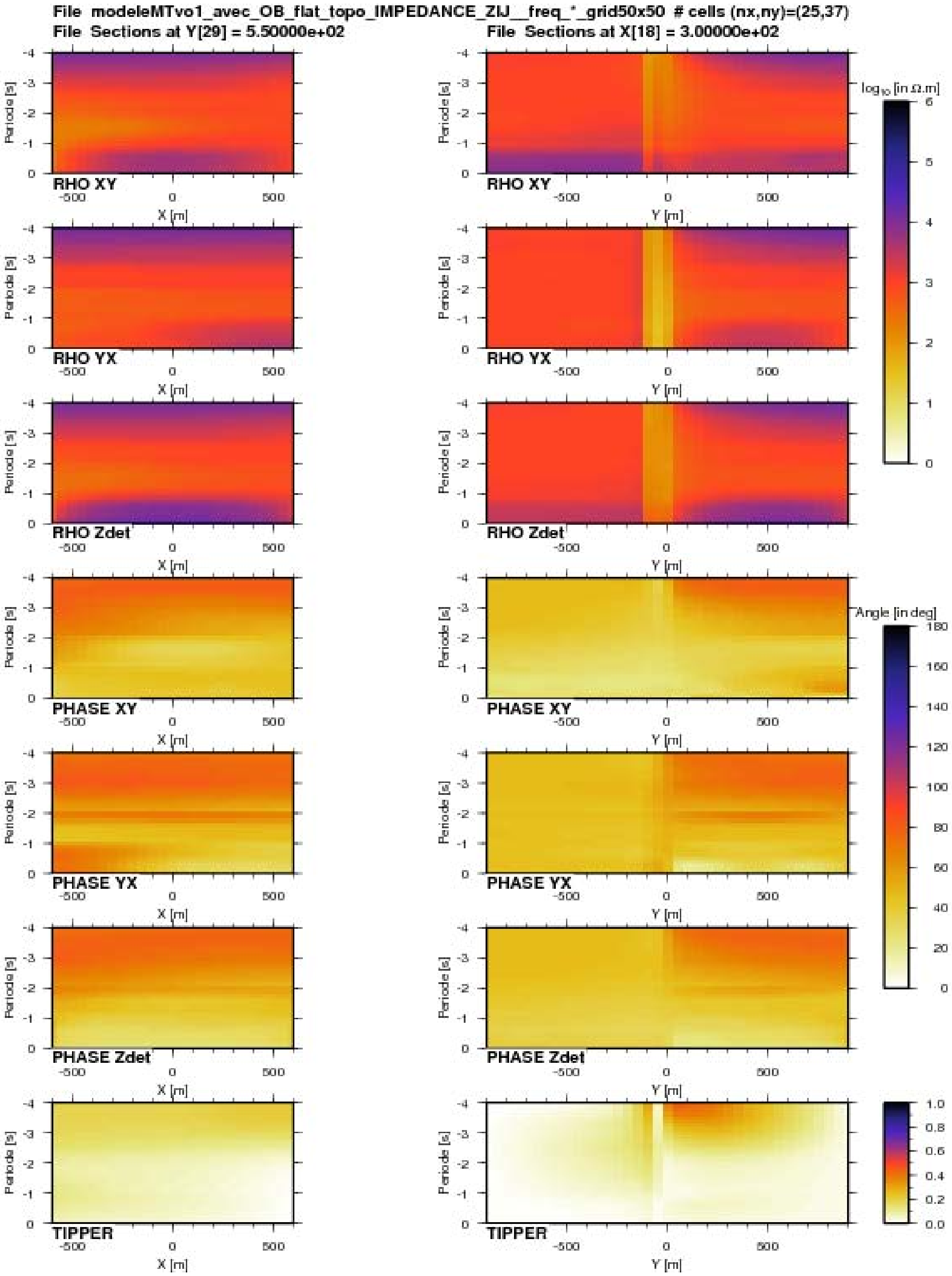

Figure RAG-5: apparent resistivities and phases (xy, yx and det) and tipper pseudo sections of the Raglan model for = [1 Hz - 10^4 Hz] along EW (X-axis at y = 550) profile on the left and NS (Y-axis at x = 300) profile on the right.

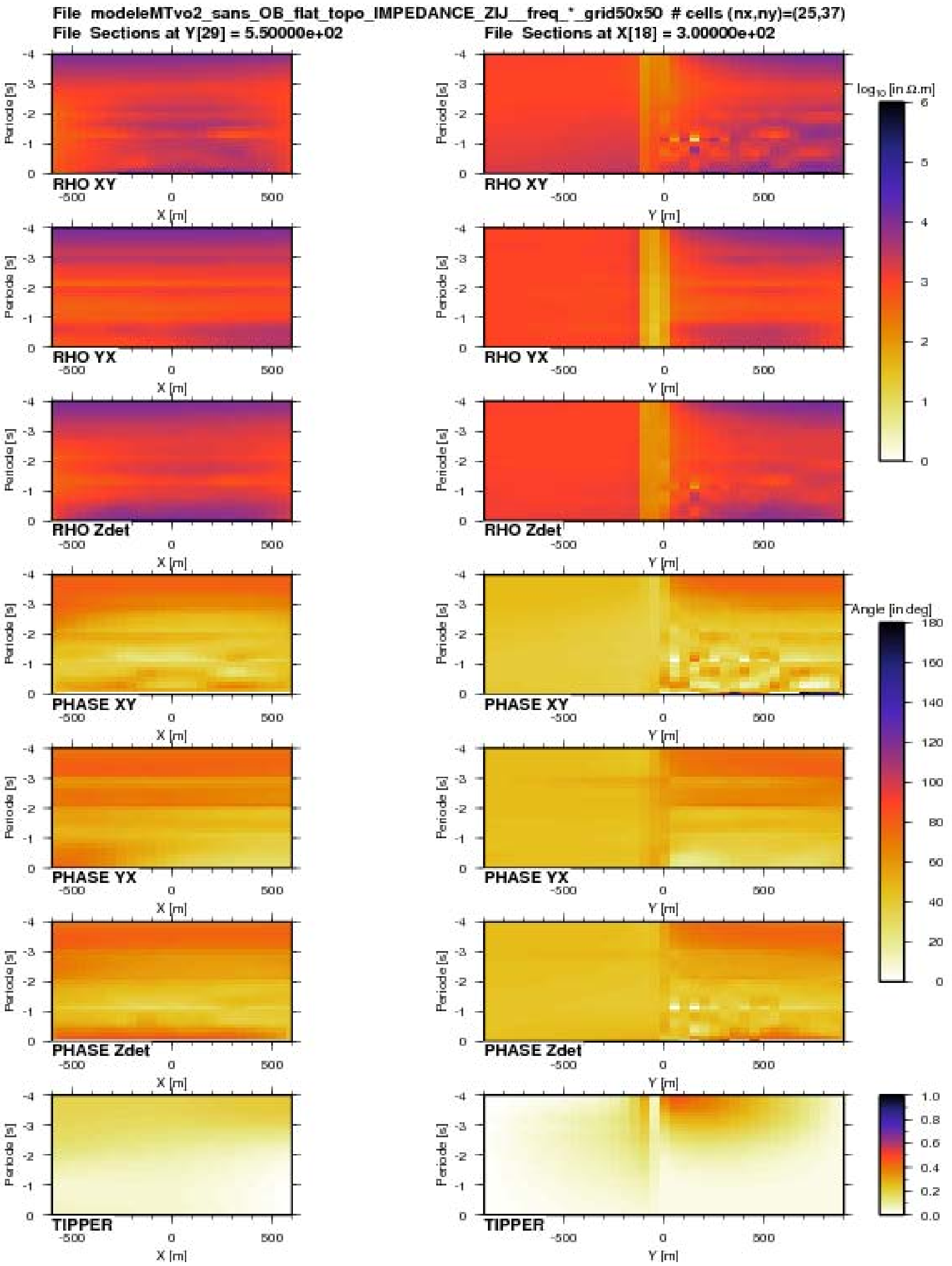

Figure RAG-6: apparent resistivities and phases (xy, yx and det) and tipper pseudo sections of the Raglan model without the conductive bodies for = [1 Hz - 10^4 Hz] along EW (X-axis at y = 550) profile on the left and NS (Y-axis at x = 300) profile on the right. The conductive bodies were replaced by bodies with the local background resistivies.

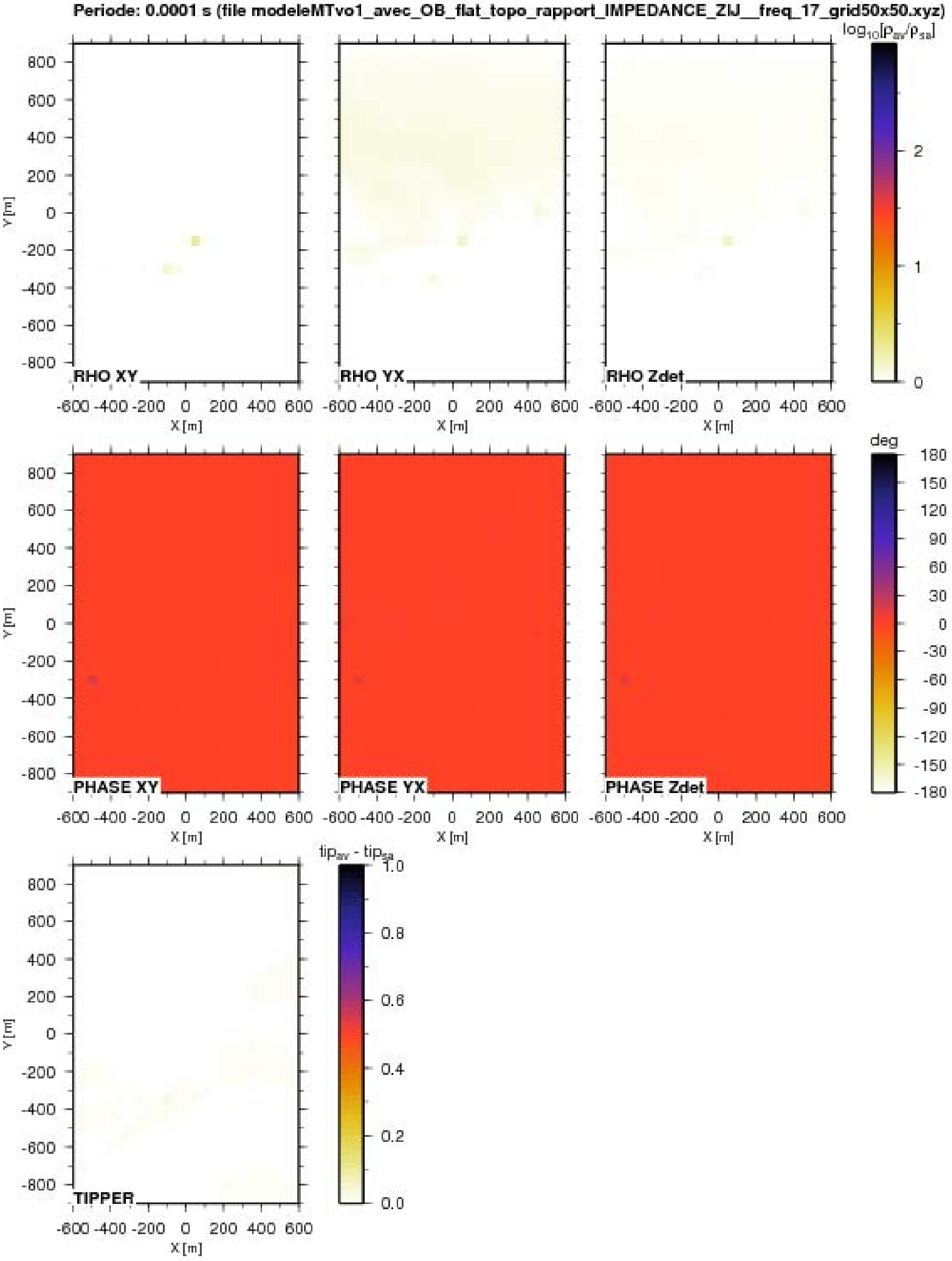

Figure RAG-7: maps showing the differences between apparent resistivities and phases (xy, yx and det) and tipper for F = 10^4 Hz between the model including the known conductive orebodies and the one excluding them. Within roundoff error the difference is virtually zero for resistivity, phase and tipper.

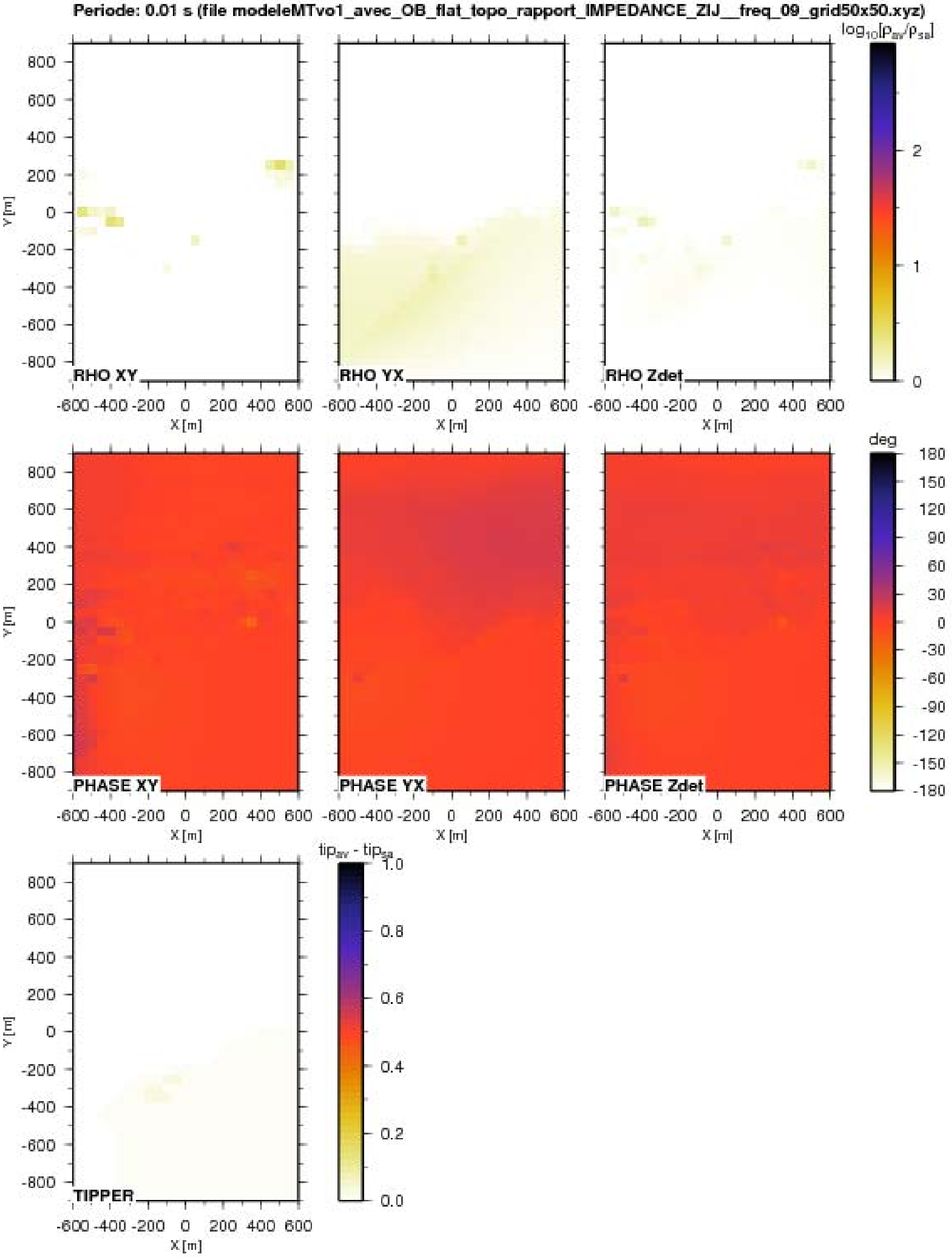

Figure RAG-8: maps showing the differences between apparent resistivities and phases (xy, yx and det) and tipper for $F = 10^2$ Hz between the model including the known conductive orebodies and the one excluding them. Most of the differences are zero for all parameters except for a few randomly distributed non-zero values caused by some inaccuracies in the calculation.

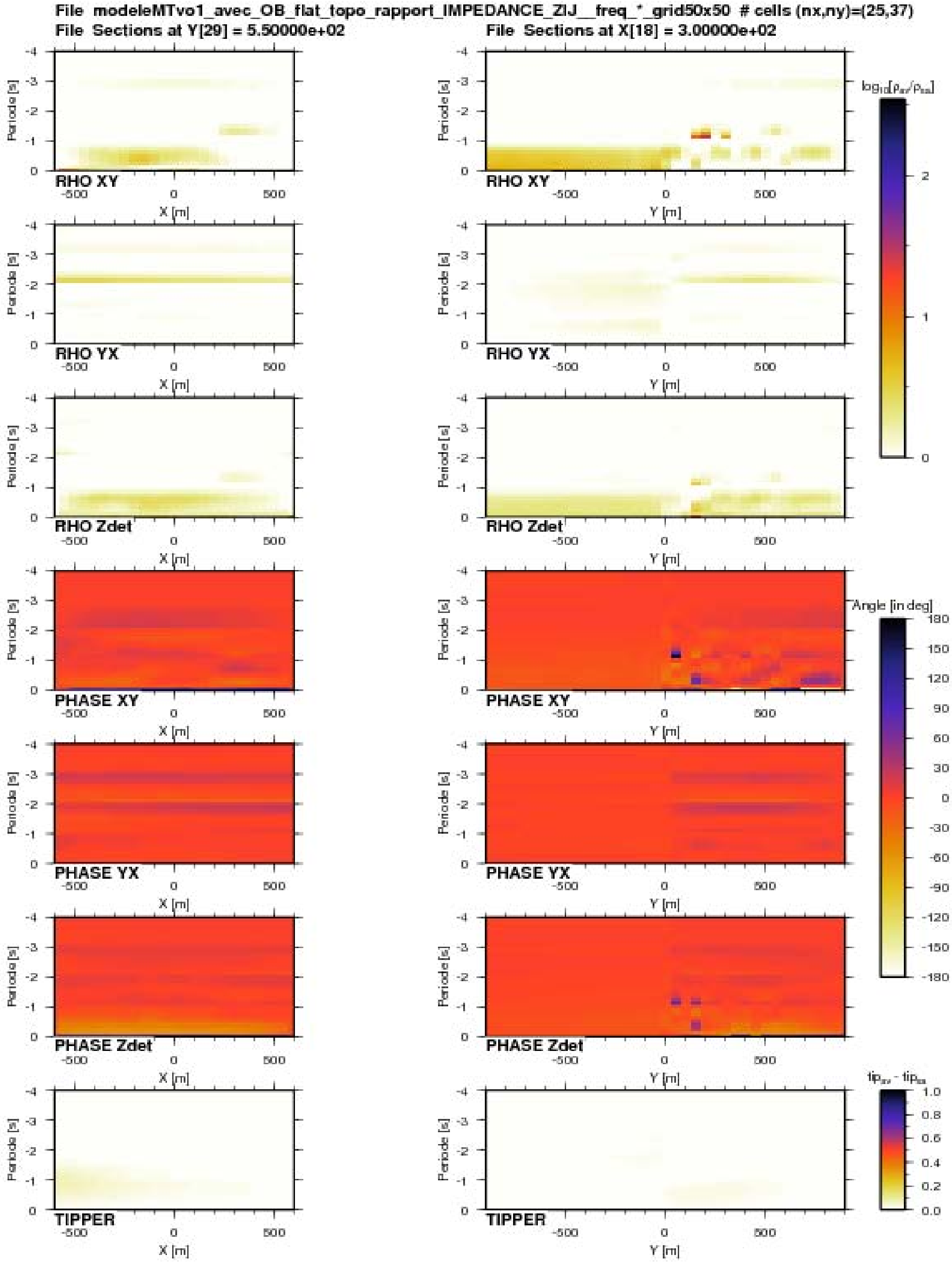

Figure RAG-9: pseudo sections displaying the differences between apparent resistivities and phases (xy, yx and det) and tipper of the Raglan model including and excluding the conductive bodies for = [1 Hz - 10^4 Hz] along EW (Xaxis at y = 550) profile on the left and NS (Y-axis at x = 300) profile on the right.

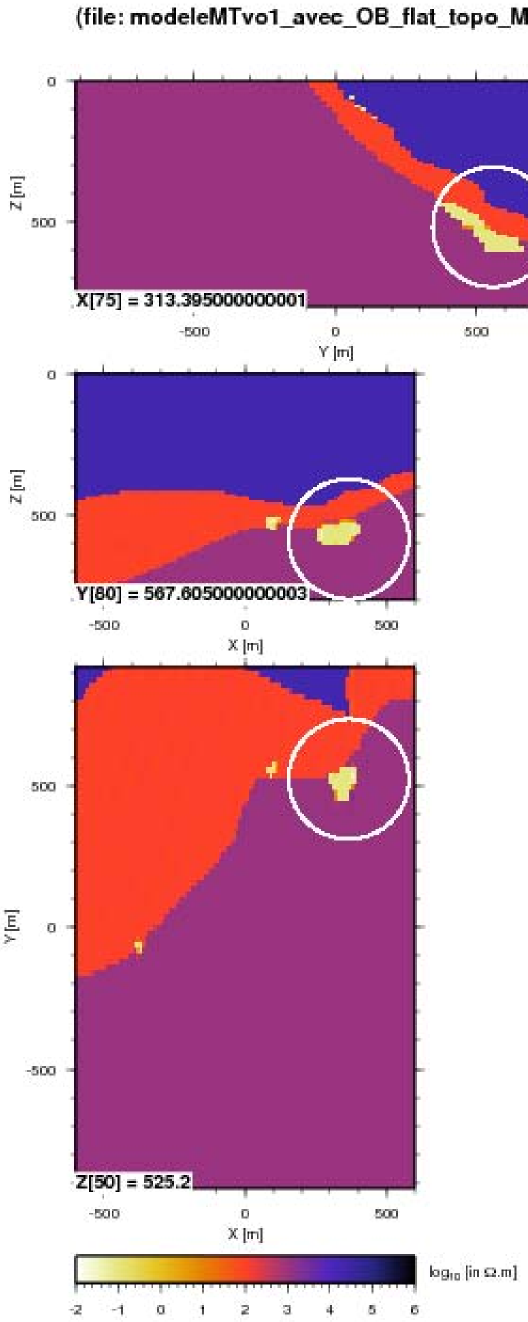

Figure RAG-10: Model 1 of Raglan with orebody 8H enlarged. Three slices of the Raglan mining camp resistivity model: (top) a NS cross-section running perpendicular to the main regional strike at X = 313.39; (middle) an EW cross-section at y = 567.6; (bottom) a horizontal slice at a depth of z = 525.2 m.

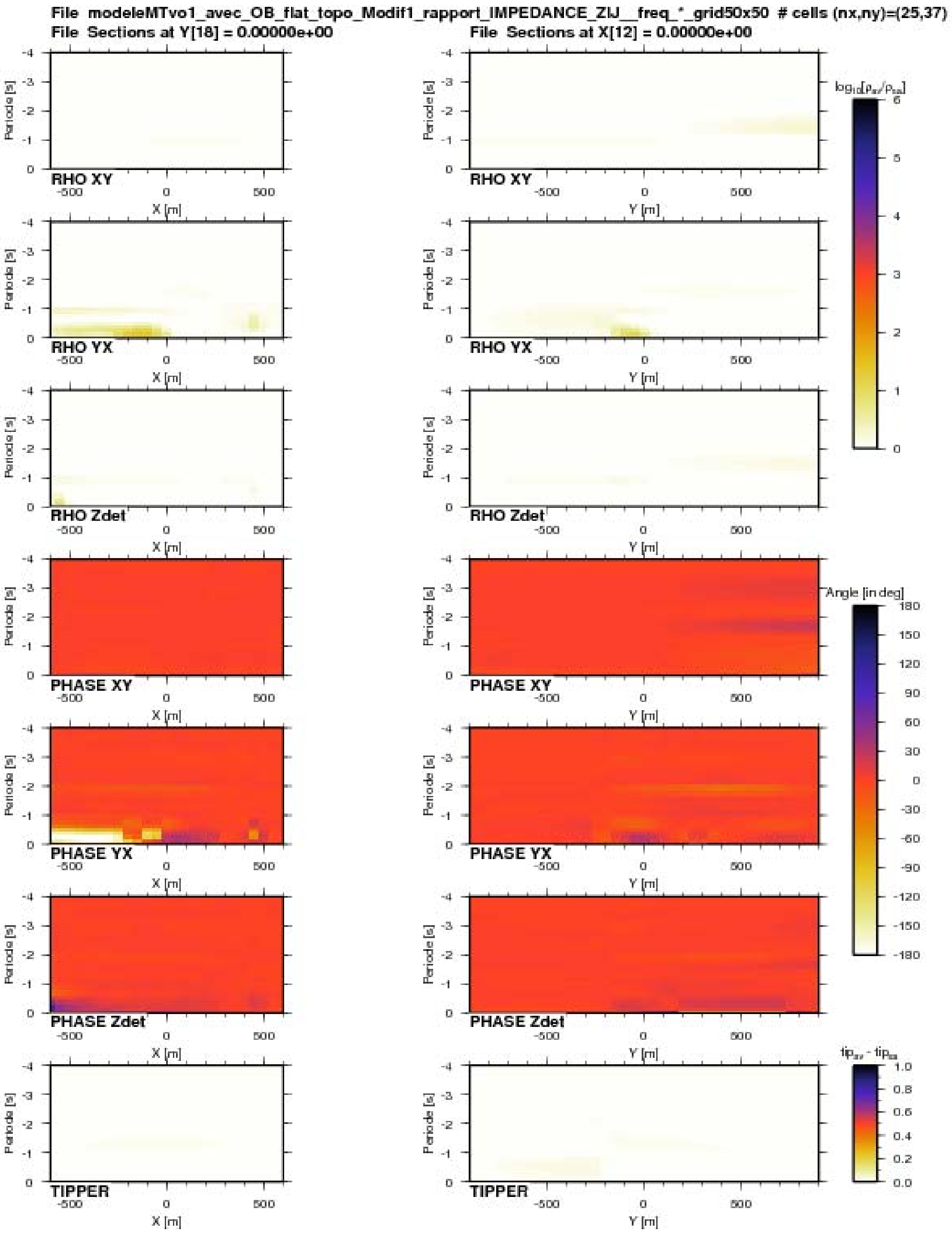

Figure RAG-11: pseudo sections displaying the differences between apparent resistivities and phases (xy, yx and det) and tipper of the Raglan model 1 compared to model 0 (original) for = [1 Hz - 10^4 Hz] along EW (X-axis at y = 0) profile on the left and NS (Y-axis at x = 0) profile on the right.

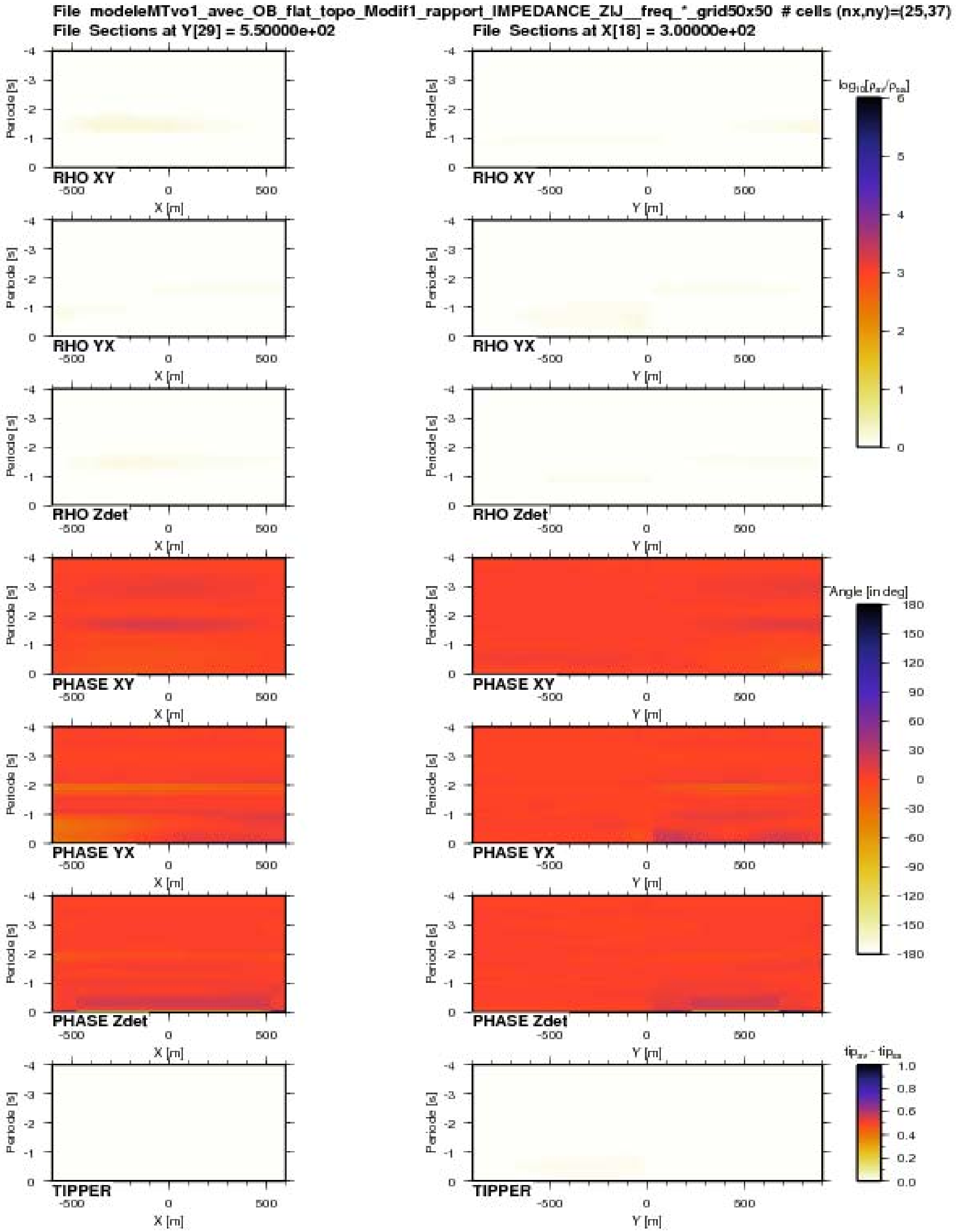

Figure RAG-12: pseudo sections displaying the differences between apparent resistivities and phases (xy, yx and det) and tipper of the Raglan model 1 compared to model 0 (original) for = [1 Hz - 10^4 Hz] along EW (X-axis at y = 550) profile on the left and NS (Y-axis at x = 300) profile on the right. Those both profiles directly run over the body 8H.

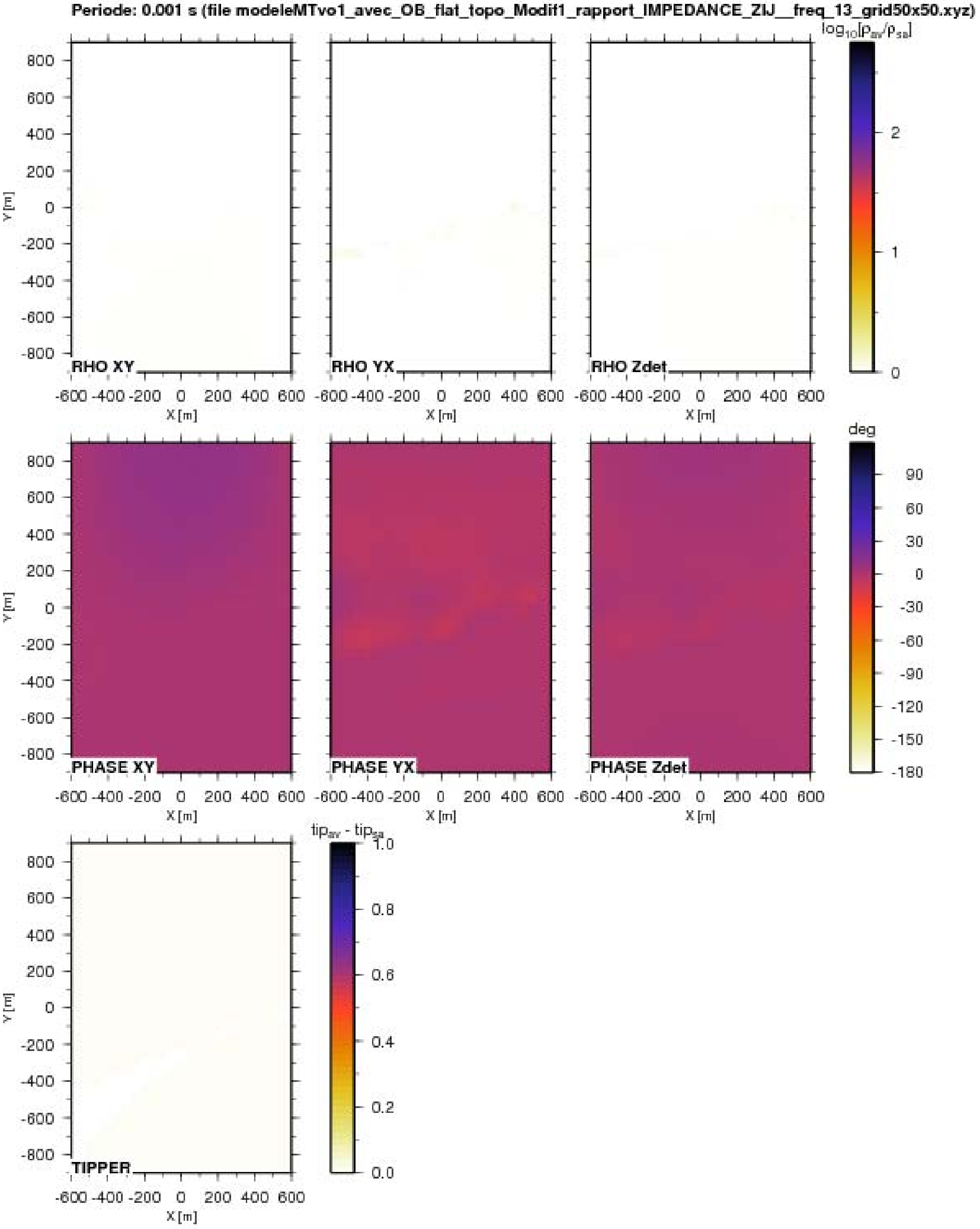

Figure RAG-13: maps showing the differences between apparent resistivities and phases (xy, yx and det) and tipper for F = 10^3 Hz between model 1 and model 0 (orebody 8H has been enlarged). Within roundoff error the difference is virtually zero for resistivity, phase and tipper.

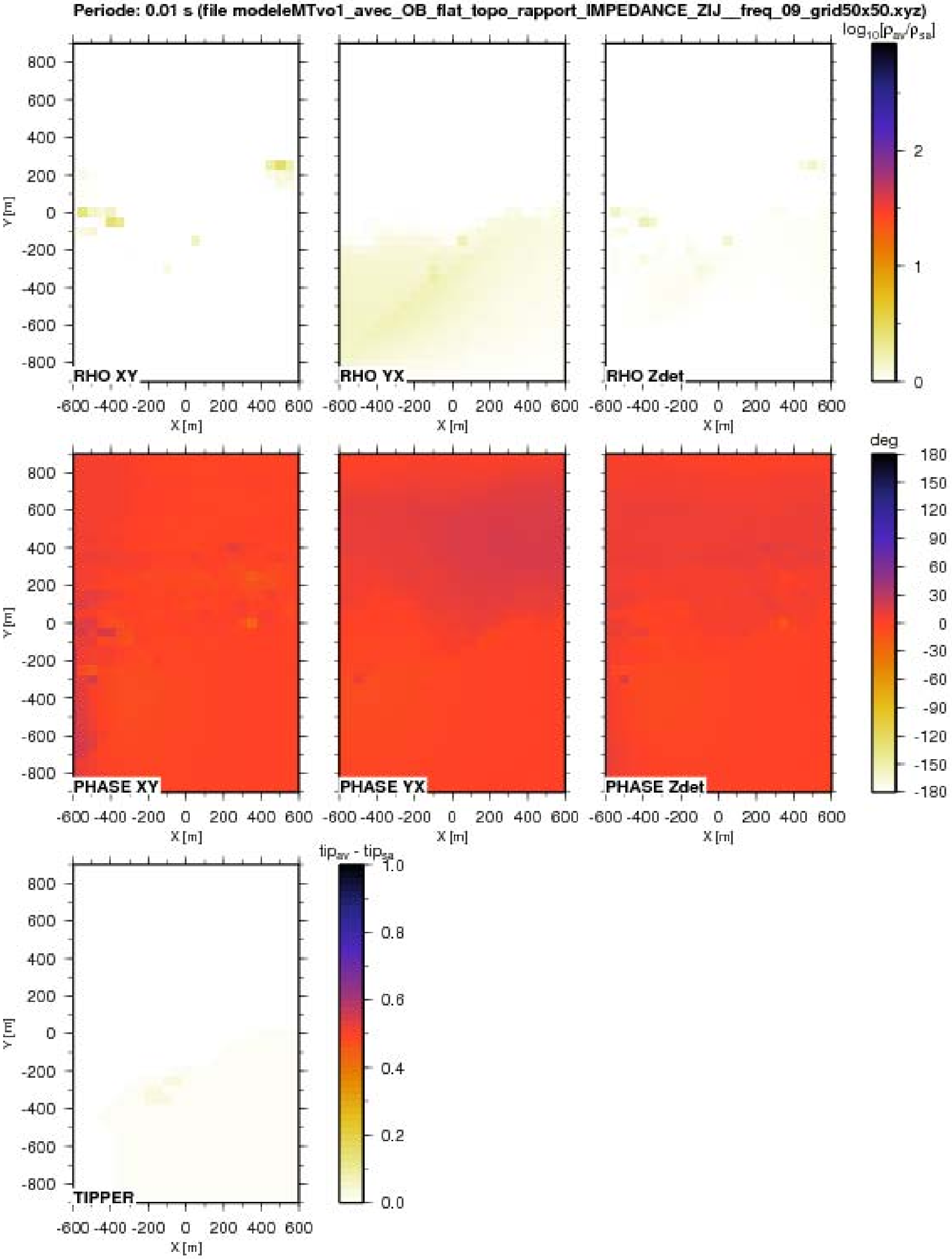

Figure RAG-14: maps showing the differences between apparent resistivities and phases (xy, yx and det) and tipper for F = 10^2 Hz between model 1 and model 0 (orebody 8H has been enlarged). Within roundoff error the difference is virtually zero for resistivity, phase and tipper.

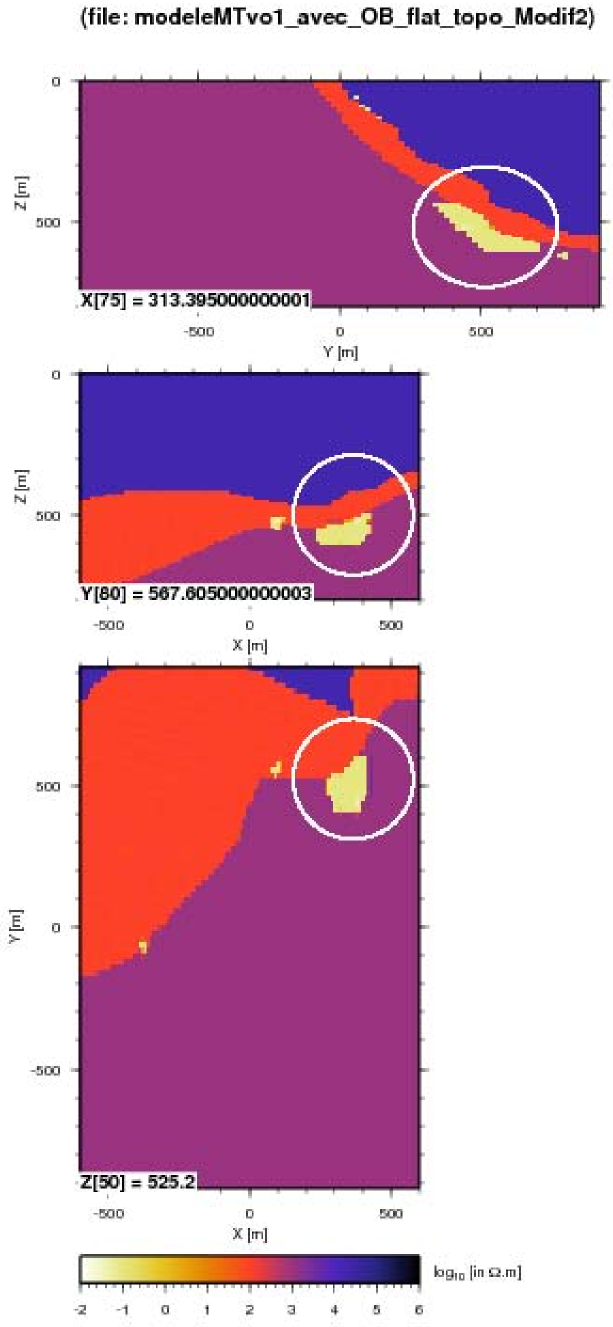

Figure RAG-15: Model 2 of Raglan with orebody 8H enlarged. Three slices of the Raglan mining camp resistivity model: (top) a NS cross-section running perpendicular to the main regional strike at X = 313.39; (middle) an EW cross-section at y = 567.6; (bottom) an horizontal slice at a depth of z = 525.2 m.

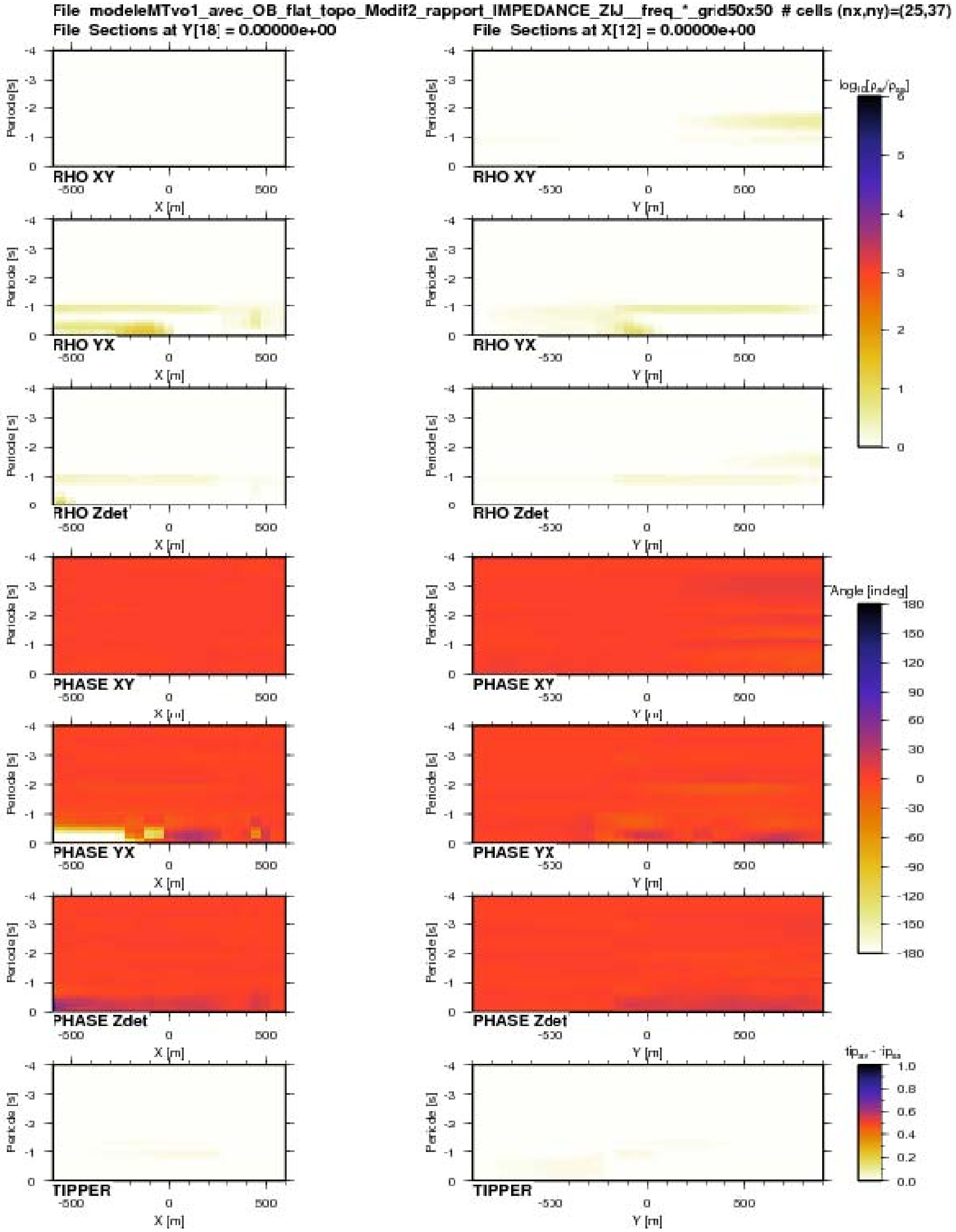

Figure RAG-16: pseudo sections displaying the differences between apparent resistivities and phases (xy, yx and det) and tipper of the Raglan model 2 compared to model 0 (original) for = [1 Hz - 10^4 Hz] along EW (X-axis at y = 0) profile on the left and NS (Y-axis at x = 0) profile on the right.

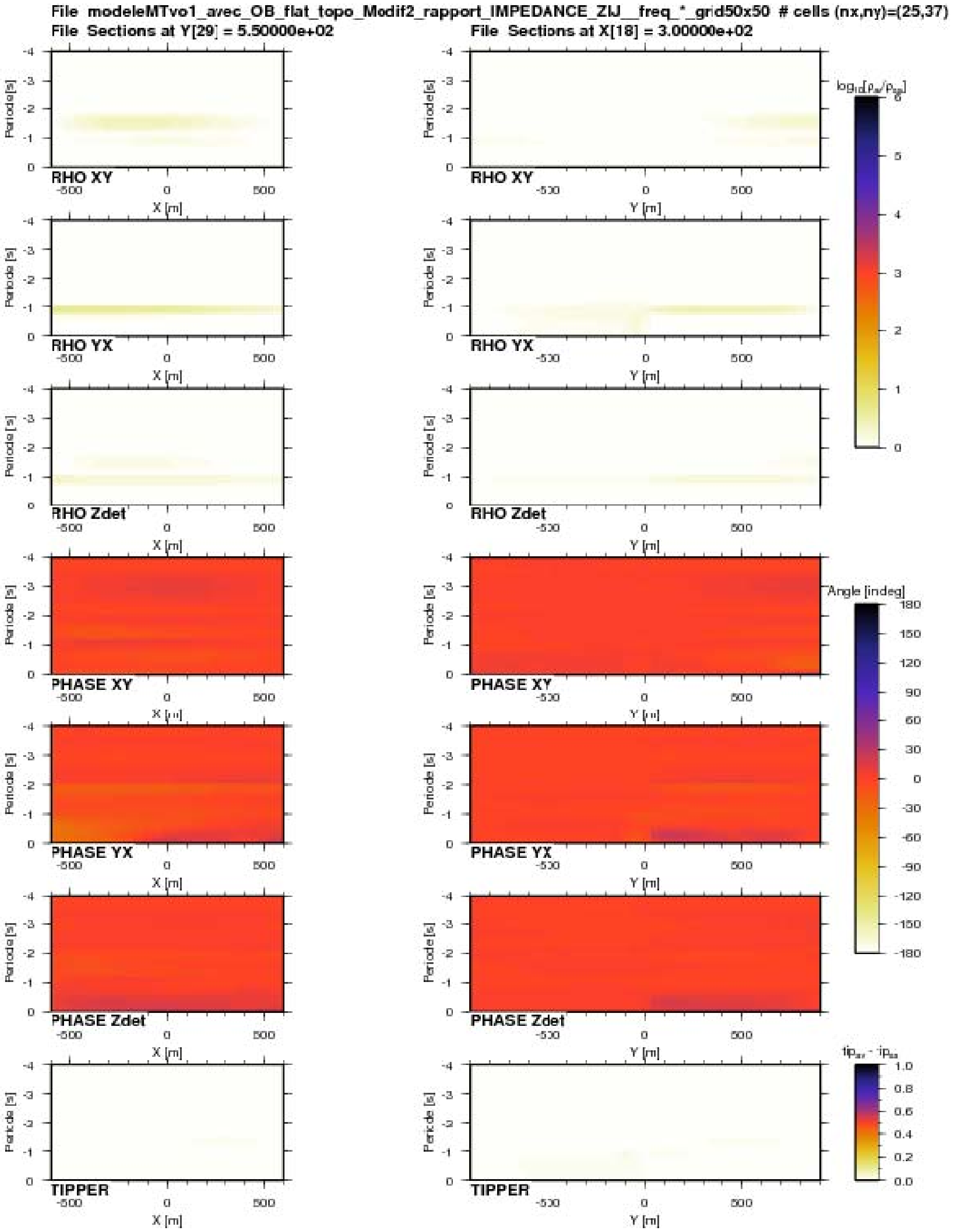

Figure RAG-17: pseudo sections displaying the differences between apparent resistivities and phases (xy, yx and det) and tipper of the Raglan model 2 compared to model 0 (original) for = [1 Hz - 10^4 Hz] along EW (X-axis at y = 550) profile on the left and NS (Y-axis at x = 300) profile on the right. Those both profiles directly run over the body 8H.

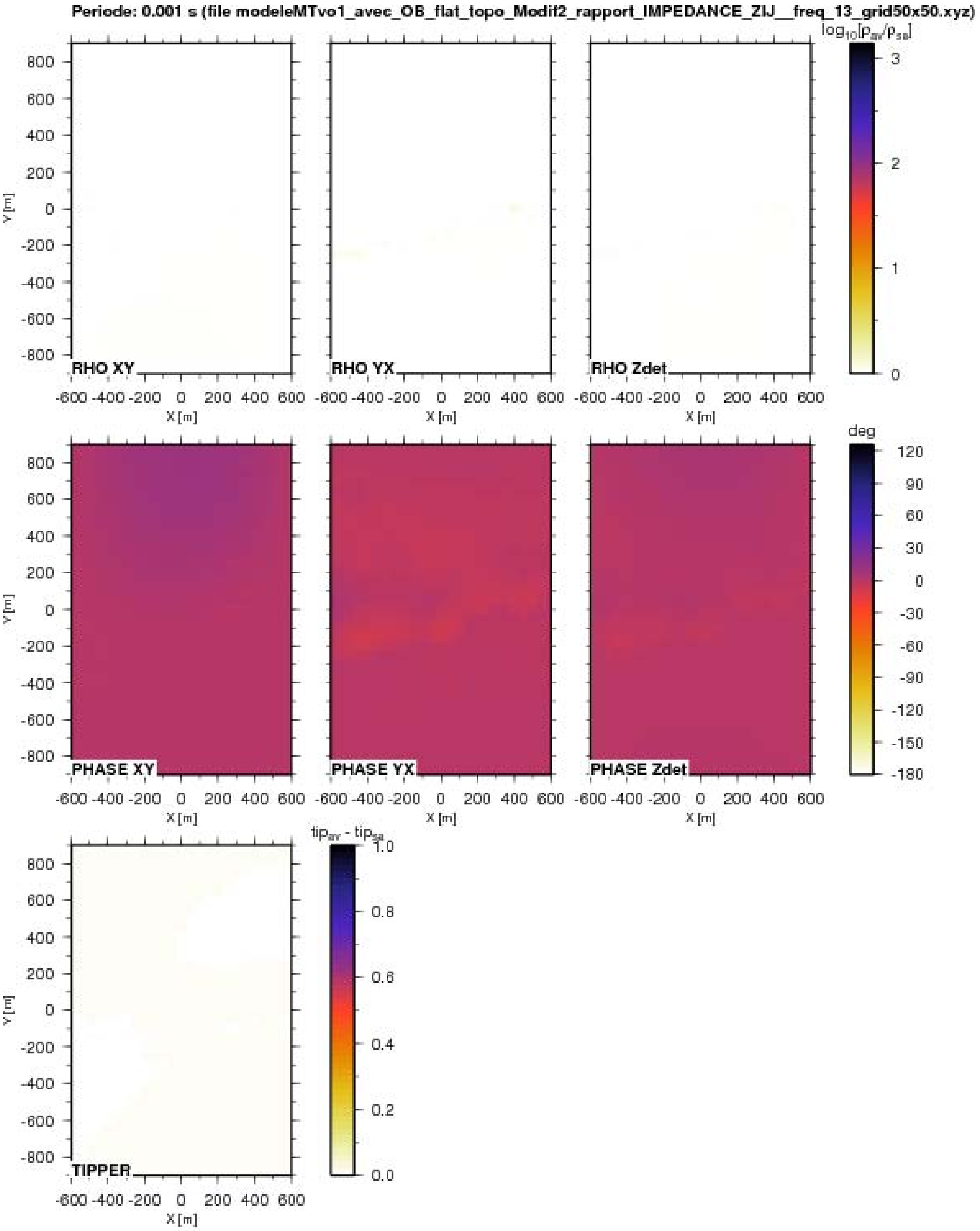
Periode: 0.001 s (file modeleMTvo1_avec_OB_flat_topo_Modif2_rapport_IMPEDANCE_ZIJ__freq_13_grid50x50.xyz)

Figure RAG-18: maps showing the differences between apparent resistivities and phases (xy, yx and det) and tipper for F = 10^3 Hz between model 2 and model 0 (orebody 8H has been enlarged). Within roundoff error the difference is virtually zero for resistivity, phase and tipper.

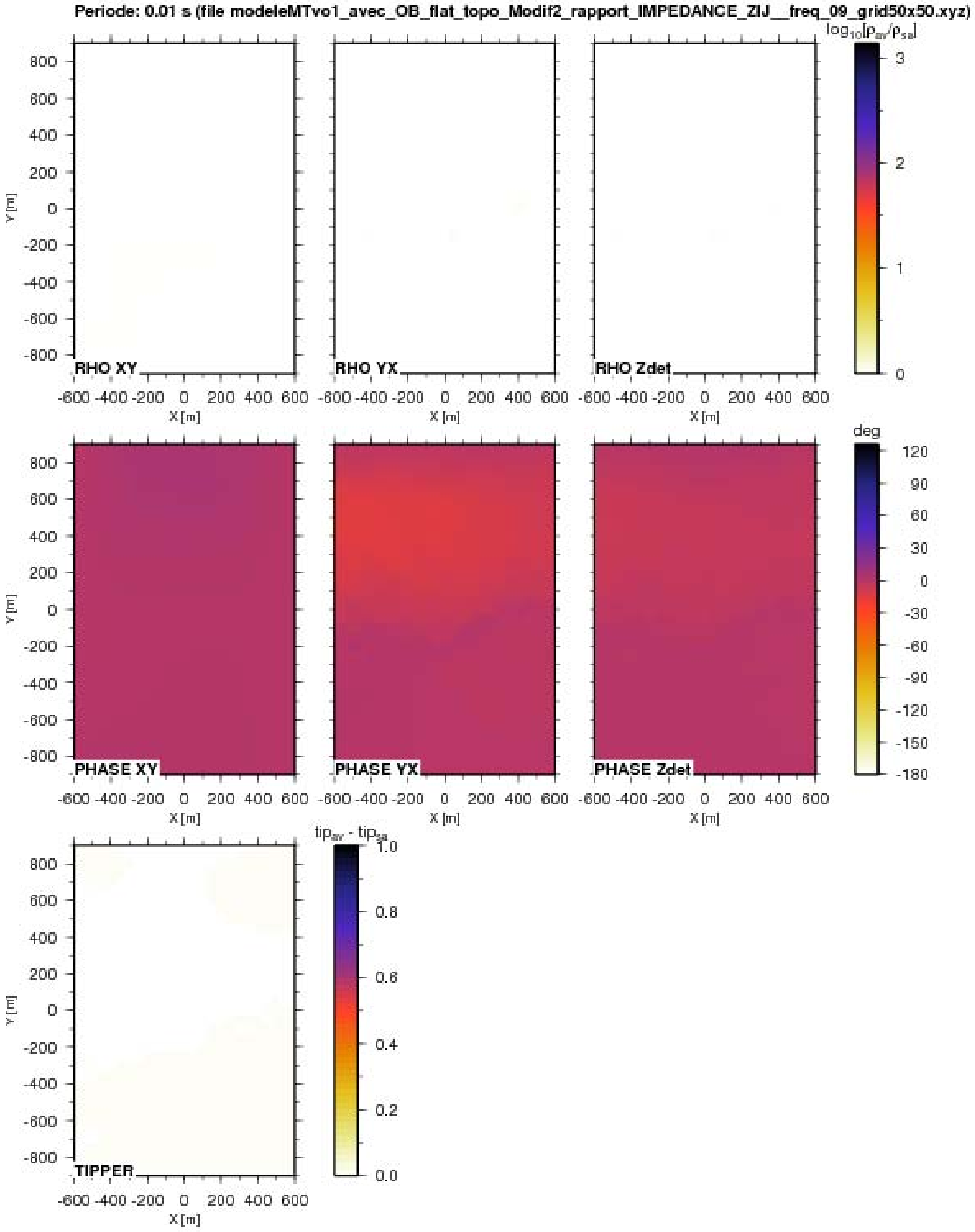

Figure RAG-19: maps showing the differences between apparent resistivities and phases (xy, yx and det) and tipper for F = 10^2 Hz between model 2 and model 0 (orebody 8H has been enlarged). Within roundoff error the difference is virtually zero for resistivity, phase and tipper.

BATHURST

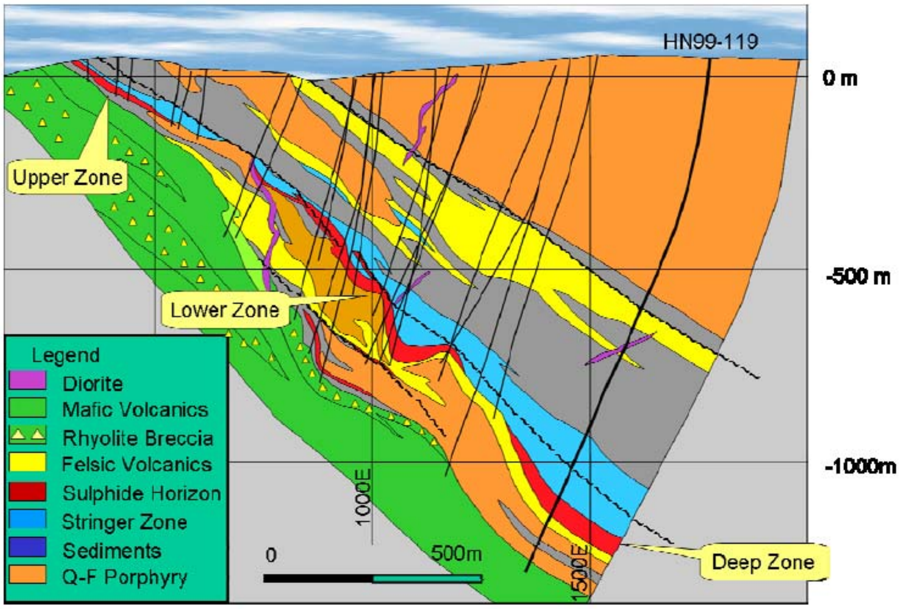

Figure Bat-1: Halfmile Lake Composite Section showing geology and drill holes.

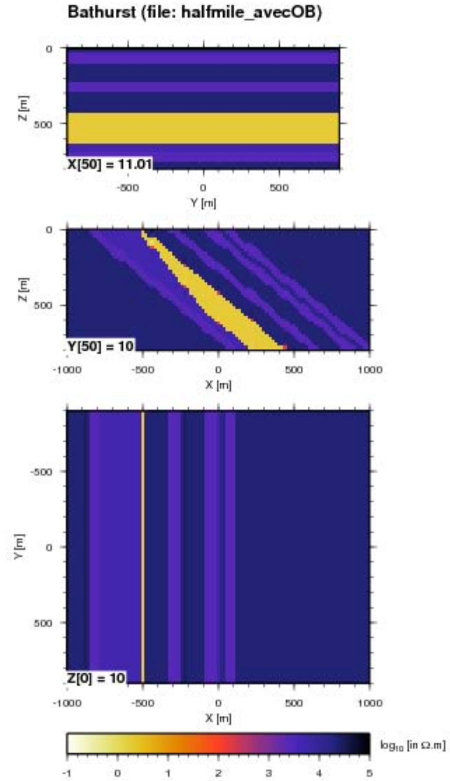

Figure Bat-2: resistivity model of the HalfMile orebody displayed as vertical slices along strike (Y-axis) at x = 11 m, perpendicular to strike (X-axis) at y = 10 m, and a horizontal slice at z = 10 m.

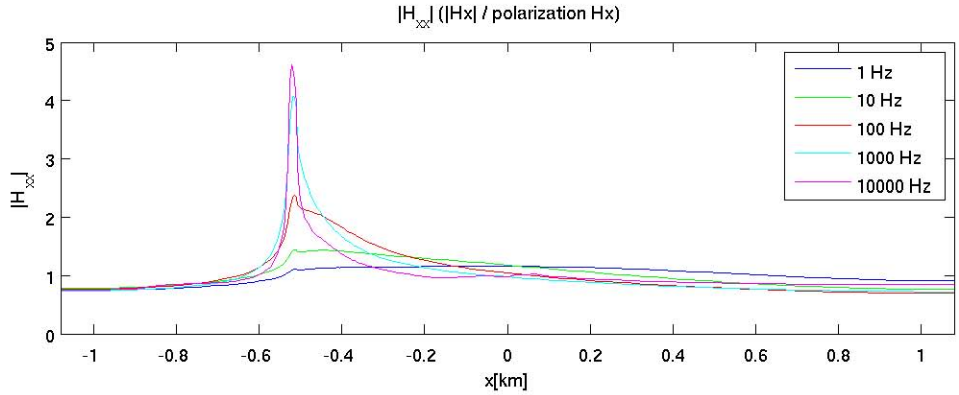

Figure Bat-3: horizontal magnetic field Hx (perpendicular to structural strike) for frequencies [1 Hz - 10^4 Hz]. At high frequencies induction causes large changes close to resistivity boundaries.

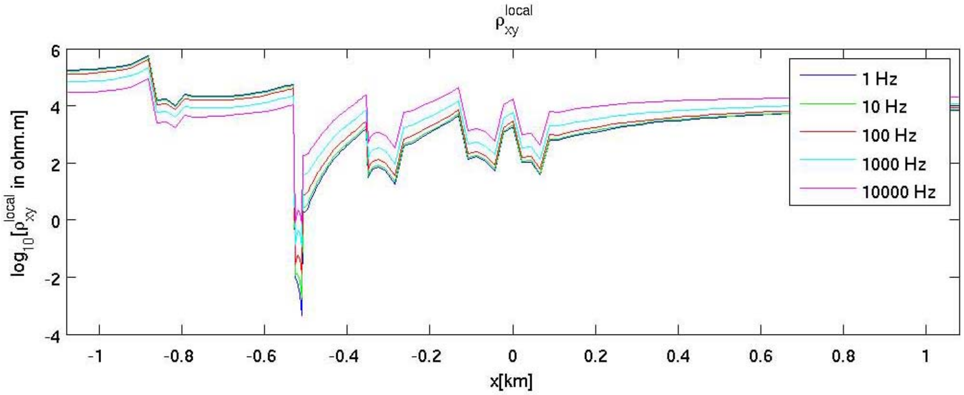

Figure Bat-4: apparent resistivity for F = [1 Hz - 10^4 Hz] with electric field measured along X (perpendicular to strike) for 5-components MT site.

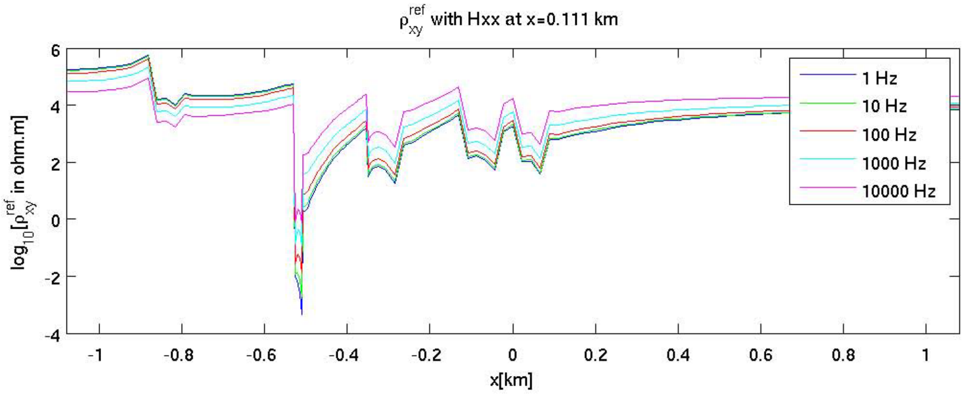

Figure Bat-5: apparent resistivity profiles for F = [1 Hz - 10^4 Hz] with electric field measured along X (perpendicular to strike) for Titan24-like MT site (magnetic field reference is at x = -0.111 km).

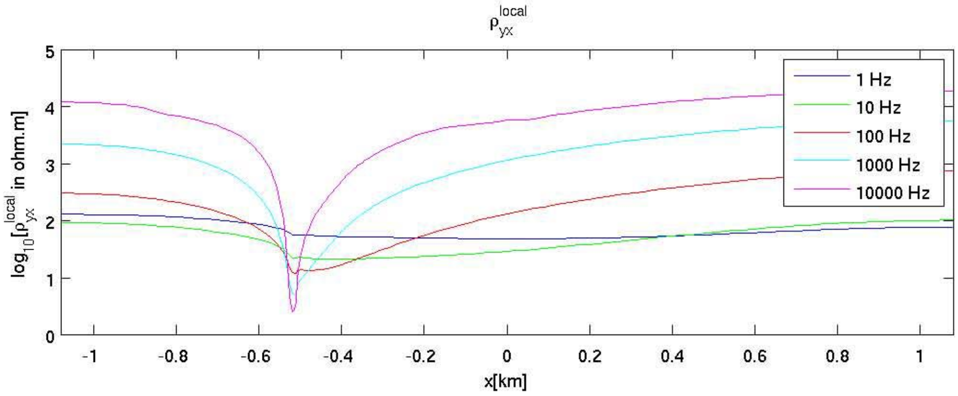

Figure Bat-6: apparent resistivity profiles for F = [1 Hz - 10^4 Hz] with electric field measured along Y (parallel to strike) for 5-components MT site.

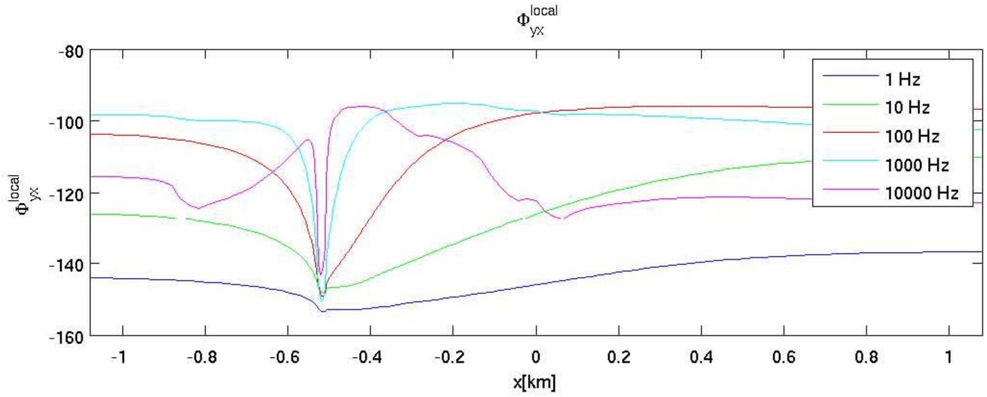

Figure Bat-7: apparent phase profiles for F = [1 Hz - 10^4 Hz] with electric field measured along Y (parallel to strike) for 5-components MT site.

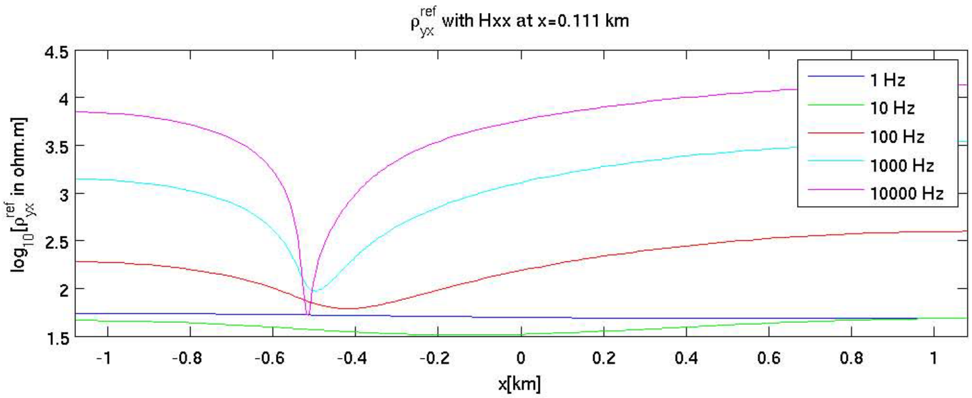

Figure Bat-8: apparent resistivity profiles for F = [1 Hz - 10^4 Hz] with electric field measured along Y (parallel to strike) for Titan24-like MT site (magnetic field reference is at x = -0.111 km).

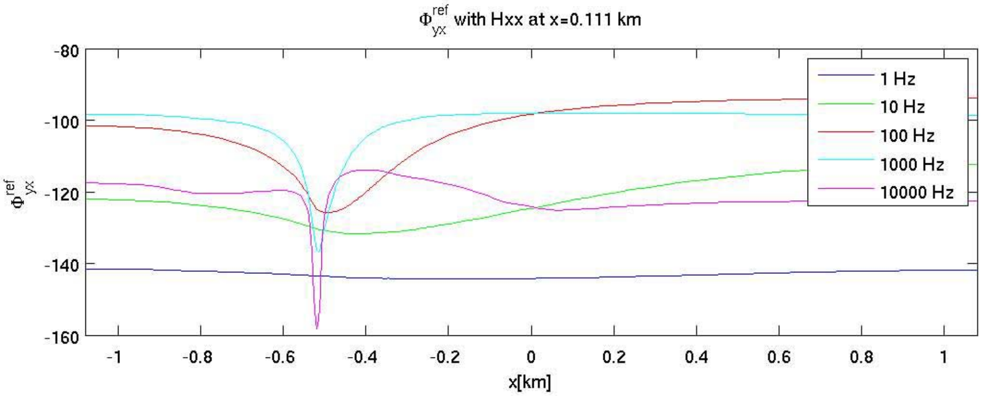

Figure Bat-9: apparent phase profiles for F = [1 Hz - 10^4 Hz] with electric field measured along Y (parallel to strike) for Titan24-like MT site (magnetic field reference is at x = -0.111 km).

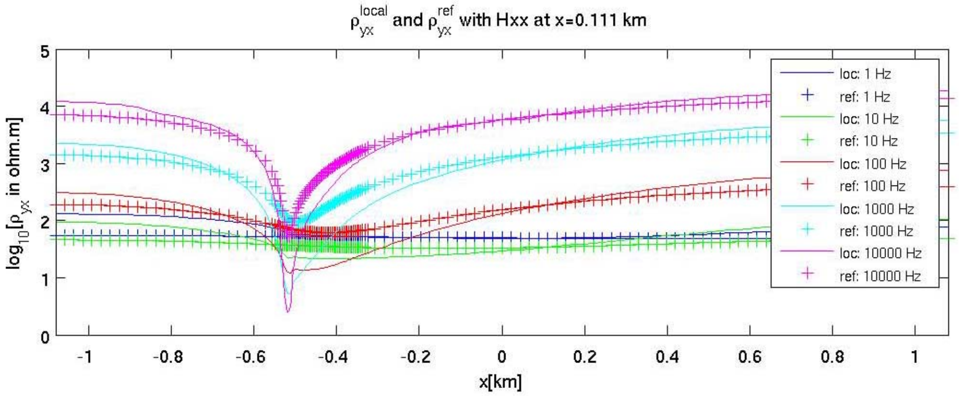

Figure Bat-10: comparison between apparent resistivity profiles for F = [1 Hz - 10^4 Hz] with electric field measured along Y (parallel to strike) for 5component and Titan24-like MT sites (magnetic field reference is at x = -0.111

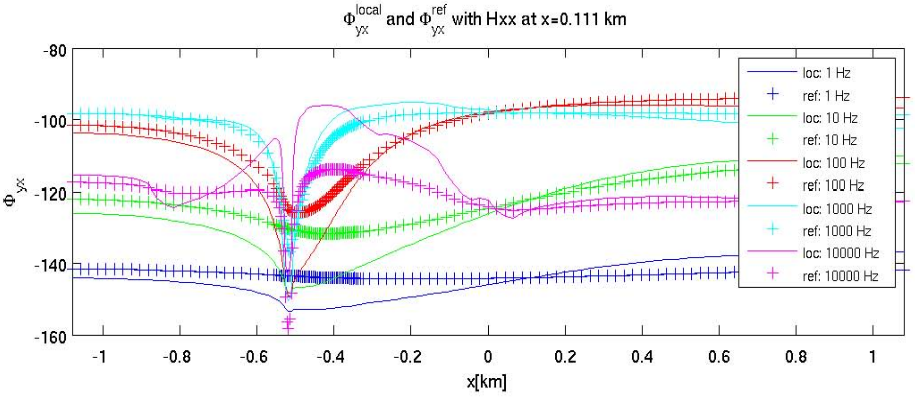

Figure Bat-11: comparison between apparent phase profiles for F = [1 Hz - 10^4 Hz] with electric field measured along Y (parallel to strike) for 5-component and Titan24-like MT sites (magnetic field reference is at x = -0.111 km for the Titan24).

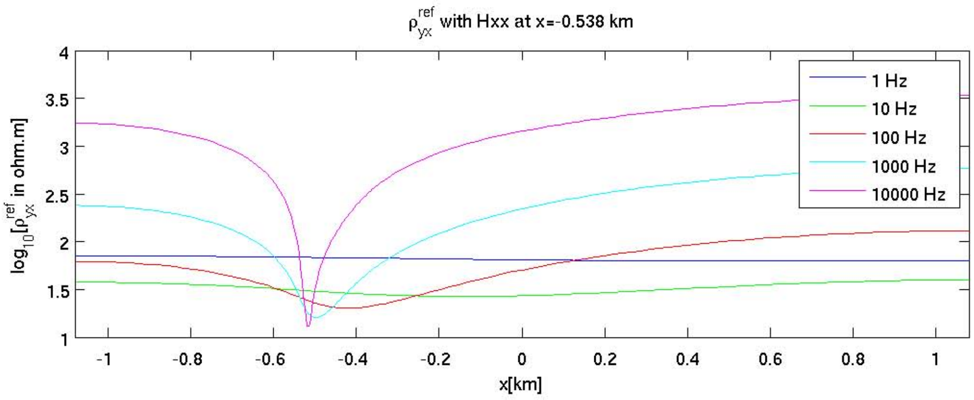

Figure Bat-12: apparent resistivity profiles for F = [1 Hz - 10^4 Hz] with electric field measured along Y (parallel to strike) for Titan24-like MT site (magnetic field reference is at x = -0.538 km).

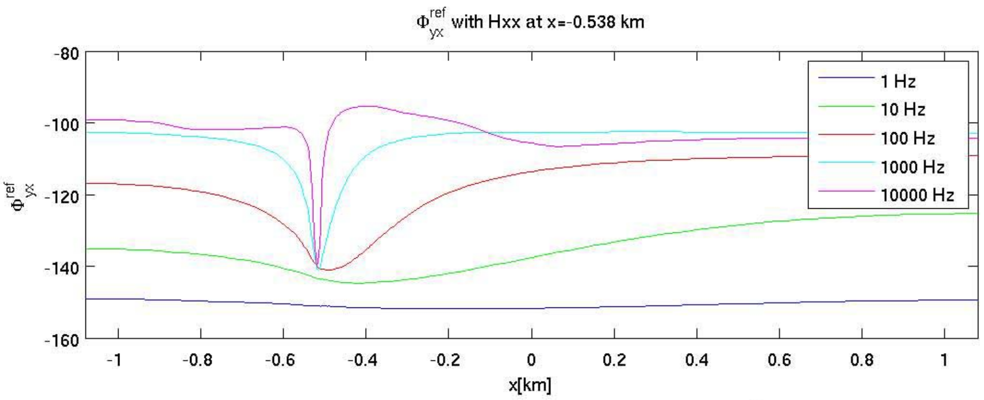

Figure Bat-13: apparent phase profiles for F = [1 Hz - 10^4 Hz] with electric field measured along Y (parallel to strike) for Titan24-like MT site (magnetic field reference is at x = -0.538 km).

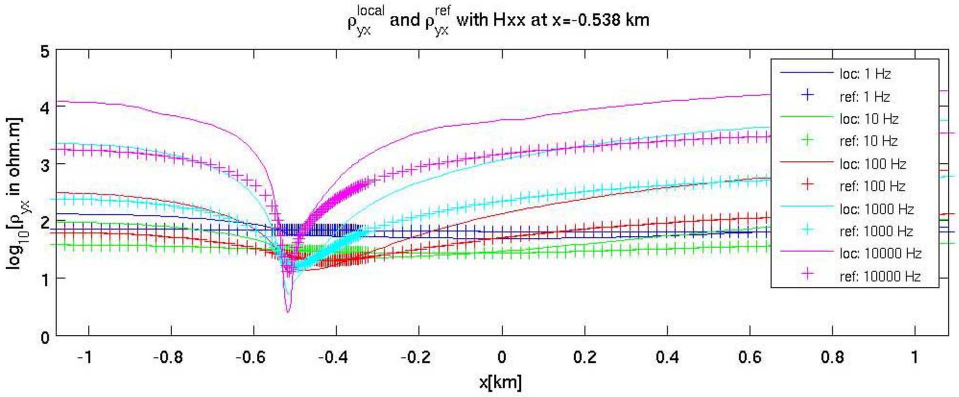

Figure Bat-14: comparison between apparent resistivity profiles for F = [1 Hz - 10^4 Hz] with electric field measured along Y (parallel to strike) for 5component and Titan24-like MT sites (magnetic field reference is at x = -0. 538 km for the Titan24).

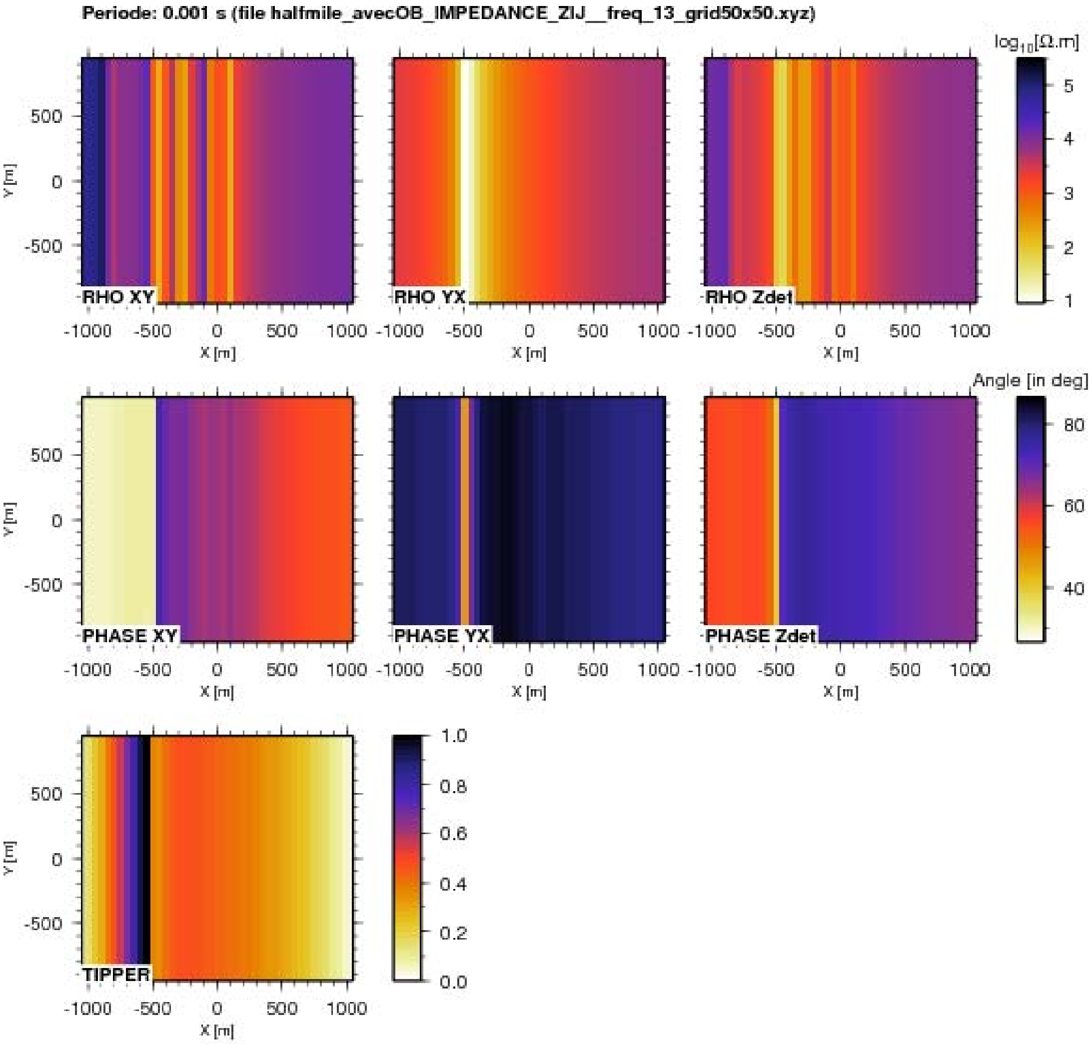

Figure Bat-15: maps showing apparent resistivities and phases and tipper for F = 10^3 Hz.

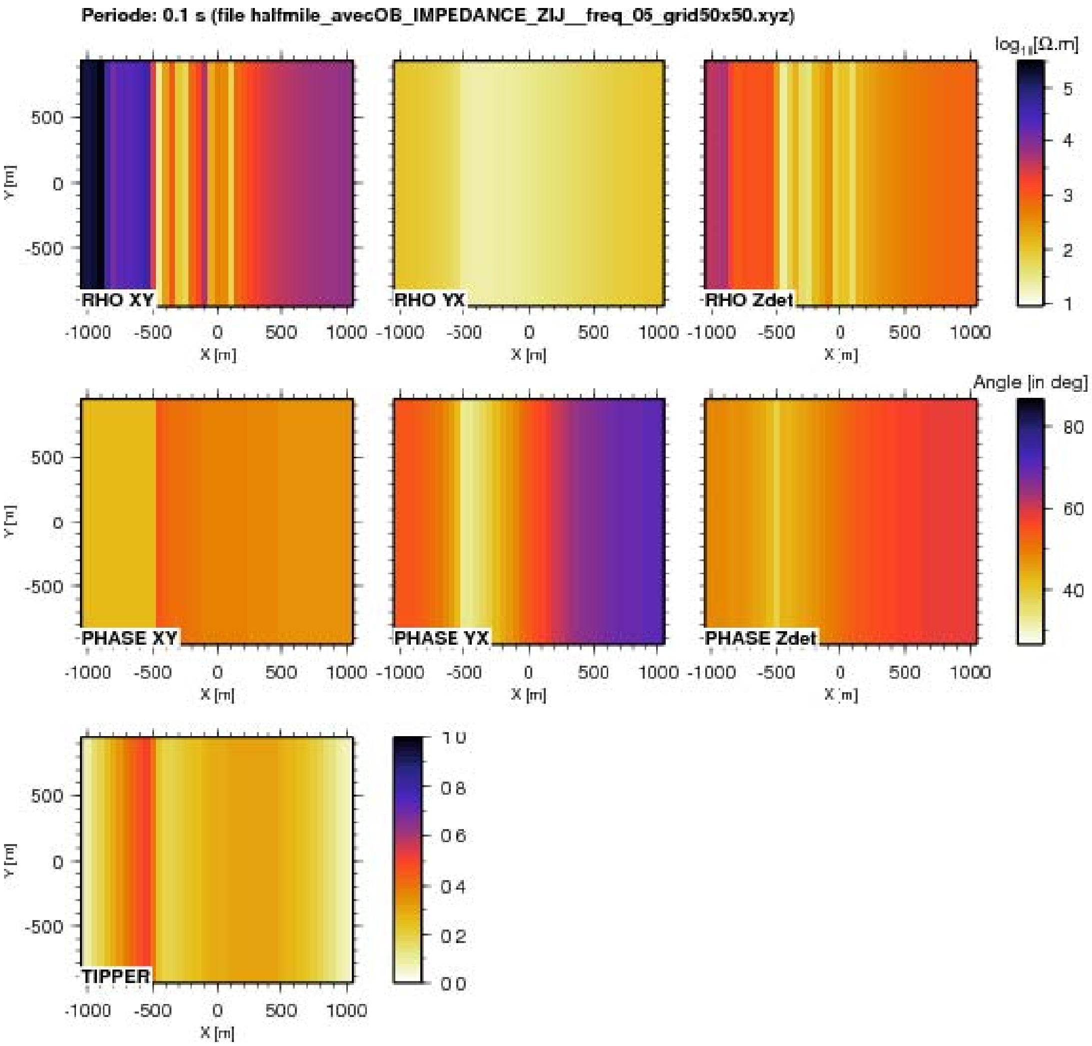

Figure Bat-16: maps showing apparent resistivities and phases and tipper for F = 10 Hz.

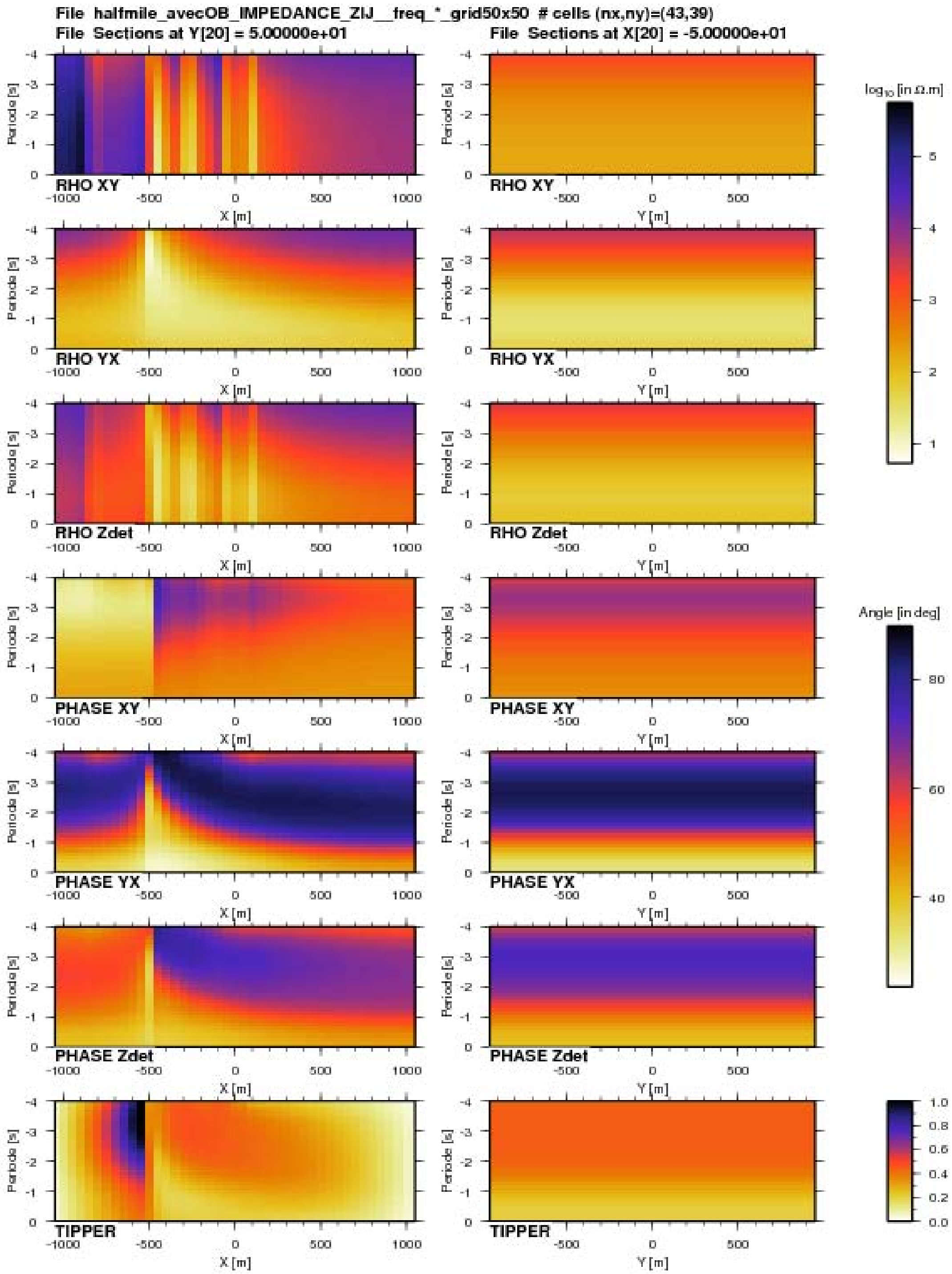

Figure Bat-17: apparent resistivities and phases (xy, yx and det) and tipper pseudo sections of the HalfMile orebody for = [1 Hz – 10^4 Hz] along profiles perpendicular to strike (X-axis) on the left and parallel to strike (Y-axis) on the right. Note the rapid MT parameter changes along X. The conductive body outcrops at about x = -0.5 km.